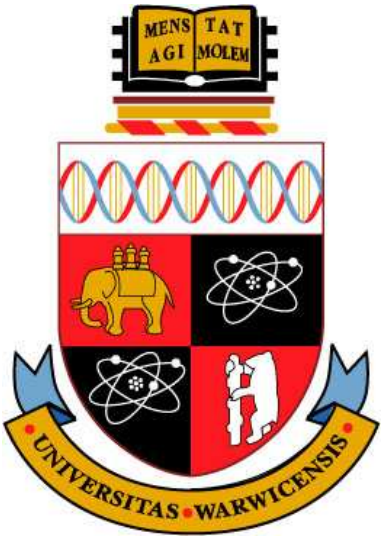

Effects of Partial Ionisation in the Solar Atmosphere

by

James Edward Leake

Thesis

Submitted to the University of Warwick

for the degree of

Doctor of Philosophy

Department of Physics

September 2006

THE UNIVERSITY OF WARWICK

Contents

List of Figures vi

Acknowledgments xiii

Declarations xiv

Abstract xv

Abbreviations xvi

Chapter 1 Introduction 1

1.1 The Sun . . . 1

1.2 The Solar Interior . . . 2

1.2.1 Internal Structure . . . 4

1.2.2 Internal Rotation . . . 7

1.3 The Solar Atmosphere . . . 8

1.4 Plasma Physics . . . 11

1.4.1 Plasma Properties . . . 12

1.4.2 The MHD Approximation . . . 14

1.5 Solar Activity and Magnetism . . . 19

1.5.1 Sunspots . . . 19

1.5.2 Granulation . . . 20

1.5.3 Coronal Structures . . . 22

1.5.4 Prominences . . . 23

1.5.5 Flares . . . 24
1.5.6 CME's . . . 25
1.5.7 The Solar Cycle . . . 26
1.5.8 The Solar Dynamo . . . 27
1.6 Magnetic Flux Emergence . . . 30
1.7 Overview of the Thesis . . . 37

Chapter 2 Partially Ionised Plasmas 38

2.1 Introduction . . . 38
2.2 Single Fluid Equations Describing Partially Ionised Plasmas . . . 40
2.2.1 The Continuity Equation . . . 40
2.2.2 Equation of Motion . . . 41
2.2.3 The Energy Equation . . . 46
2.3 EM fields for a Partially Ionised Plasma . . . 46
2.3.1 Ohm's Law . . . 46
2.3.2 Maxwell's Equations . . . 49
2.4 Equation of State . . . 49
2.5 Summary . . . 51

Chapter 3 The Partially Ionised Plasma of the Solar Atmosphere 52

3.1 Introduction . . . 52
3.2 Approximations to Ohm's Law for the Solar Atmosphere . . . 53
3.3 Governing Equations for the Solar Atmosphere . . . 57
3.4 Estimating the Ionisation of the Solar Atmosphere . . . 58
3.4.1 The Saha Equation . . . 59
3.4.2 Non-LTE . . . 60
3.4.3 Ionisation Levels in the Quiet Sun . . . 61
3.5 Estimating Cowling and Coulomb Resistivities in the Solar Atmosphere . . . 61
3.5.1 Collisional Frequencies . . . 63
3.5.2 Resistivities . . . 63
3.6 Heating Mechanisms in the Solar Atmosphere . . . 66

Chapter 4 The Lagrangian-Remap code **68**

4.1 Introduction . . . 68

4.2 The Lagrangian Remap code . . . 69

4.2.1 Equations . . . 69

4.2.2 The Grid . . . 70

4.2.3 The Lagrangian Step . . . 70

4.2.4 The Remap Step . . . 73

4.2.5 Viscous Effects . . . 73

4.2.6 Resistive Effects . . . 74

4.3 Adapting the Lare Code . . . 75

4.3.1 The Resistive Step . . . 75

4.3.2 The Equation of State . . . 77

4.4 Modeling Heating in the Lower Atmosphere . . . 78

Chapter 5 Collisional Damping of Alfvén Waves **81**

5.1 Introduction . . . 81

5.1.1 Theory of MHD Waves . . . 82

5.1.2 Waves in the solar atmosphere . . . 84

5.1.3 Damping of Alfvén Waves . . . 86

5.2 The Efficiency of Collisional Frictional Damping of Alfvén Waves . . . 88

5.2.1 Analytic Approach . . . 88

5.2.2 Numerical Simulations . . . 91

5.3 Conclusions . . . 101

Chapter 6 2D Simulations of Emerging Magnetic Flux **104**

6.1 Introduction . . . 104

6.2 Numerical Simulations . . . 105

6.2.1 Model atmosphere . . . 106

6.2.2 Initial Magnetic Field Profile . . . 108

6.2.3 Equations . . . 110

6.2.4 Numerical Method . . . 111

6.3 Evolution of the Magnetic Field in the Convection Zone and Photosphere 112
6.4 The Effect of Heating in the Lower Atmosphere 117
6.5 The Effect of Partial Ionisation 121
6.5.1 Emergence of Magnetic Flux 123
6.5.2 Cross-Field and Field-Aligned Currents 125
6.6 Conclusions 132

Chapter 7 3D Simulations of Emerging Magnetic Flux 135
7.1 Introduction 135
7.2 3D Model 136
7.3 Emergence of Magnetic Field into the Atmosphere 139
7.4 The Effect of Partial Ionisation 141
7.5 Conclusions 148

Chapter 8 Conclusions and Future Work 150
8.1 Thesis Summary 150
8.2 Suggestions for Future Work 152

Appendix A Numerical Integration of the Hydrostatic Equation 154

List of Figures

1.1 The temperature, pressure, density and mean mass calculated from the standard model as a functions of radius for the interior of the Sun. . . 3

1.2 A parcel of gas is adiabatically lifted to a region of different density. . . 5

1.3 Left panel: The rotation rate in nHz at five different latitudes as functions of depth. Right Panel: The rotation rate as a function of radius and latitude. Courtesy National Solar Observatory. 7

1.4 The temperature and density in the solar atmosphere. Courtesy Eugene Avrett, Smithsonian Astrophysical Observatory. 10

1.5 Density (left panel) and temperature (right panel) profiles in the low solar atmosphere showing the photosphere, chromosphere and transition region (TR). Values were obtained from the VALC model of the quiet Sun. 10

1.6 Sunspot structure showing the dark umbra in the centre of the filamentary penumbra and the background granulation pattern. Courtesy Vacuum Tower Telescope, National Solar Observatory and National Optical Astronomy Observatory. 21

1.7 SOHO-EIT image from 14 September 1997 showing a huge eruptive prominence in the resonance line of singly ionised helium (He II) at 304 Angstroms in the extreme ultraviolet. The material in the eruptive prominence is at temperatures of 60,000 - 80,000 K, much cooler than the surrounding corona, which is typically at temperatures above 1 million K. Courtesy European Space Agency and NASA. 22

1.8 A coronal arcade taken by TRACE on November 15th 2000. Courtesy TRACE consortium and NASA. 23

1.9 The 'Butterfly' diagram. Top panel shows latitude of emerging sunspots as a function of time. Bottom panel shows total averaged number of sunspots. Courtesy NASA. 26

1.10 Schematic diagram showing the idea of flux emergence and its relation to the solar dynamo. (0) and (1) show the generation and destruction of small scale magnetic field in the convection zone. (2) and (3) show the transport of magnetic field from the tachocline into the convection zone and flux pumping in the reverse direction. (4) shows the formation of flux tubes from the toroidal field. (5) and (6) show the generation of poloidal field by helical turbulence. (7) shows the emergence of the flux tube into the atmosphere and the formation of an active region. Courtesy N H Brummel. 32

3.1 The density (left) and temperature (right) stratification taken from the VALC model of the quiet Sun (Vernazza et al., 1981). 53

3.2 $\frac{n_i^2}{n_n}$ (left) and $\frac{n_n}{n_i}$ calculated using the density and temperature from the VALC model. The solid line is from the Saha equation, and the dashed line is from the modified Saha equation. 62

3.3 The neutral fraction $\xi_n = \frac{n_n}{n_n+n_i}$ calculated using the density and temperature from the VALC model. The solid line is from the Saha equation, and the dashed line is from the modified Saha equation. 62

3.4 A list of the magnetic field strength profiles used to calculate the resistivities. Profiles A-C are constant values. Profiles D-F have a power law dependence on density to maintain magnetic flux with height. $B_{ph} = 1200G$ and $\rho_{ph} = 2.7 \times 10^{-4} kg/m^3$ 64

3.5 The Cowling (solid lines) and Coulomb (dashed lines) resistivities as functions of height for the different magnetic field profiles in figure 3.4. The top left panel is profile A, top right B, middle left C, middle right D, bottom left E, bottom right F. 65

4.1 The computational domain in the x direction, showing cell boundaries (xb) and cell centres (xc). 70

4.2 The staggered grid showing magnetic field and velocity components. . 71

5.1 A cartoon diagram of how Alfvénic disturbances can be generated by horizontal motions at the surface and propagate upwards along open field structures which build up in inter-granular lanes. 85

5.2 The variation of the model background magnetic field with height. The four curves relate to the value of the exponent $\alpha = 0.2$ (small dash line), 0.35 (large dash line), 0.4 (thick solid line) and 0.6 (thin solid line). . . 89

5.3 Cowling (solid line) and Coulomb (dashed line) resistivities as a function of height calculated using ionisation levels from the modified Saha equation using varying $|\mathbf{B}|$ with height, with $\alpha = 0.2$. 90

5.4 Analytical estimates for the damping efficiency of Alfvén waves in the partially ionised region of the solar chromosphere, as a function of frequency. The four lines represent the four magnetic field profile given by $\alpha = 0.2$ (thin solid line). 0.35 (dashed line), 0.4 (dot-dashed line) and 0.6 (thick solid line). 92

5.5 Model atmosphere showing density (thin solid line), temperature (dashed line), gas pressure (dot-dashed line) and neutral fraction (thick solid line). The height is in units of photospheric scale height. 94

5.6 Velocity (top panels) and magnetic field (bottom panels) perturbations as a function of height for a typical run with $f = 0.07$Hz, The left hand panels are for the case of $\eta_c = 0$ and the right hand panels are for the η_c calculated at each step. The velocity and magnetic field are given in dimensionless units. 97

5.7 Estimates of the efficiency of damping due to ion-neutral collisions for the magnetic field profile with power law $\alpha = 0.2$. The solid line is the estimate due to analytic approaches and the triangles represent the estimates obtained from numerical data. 99

5.8 Estimates of the efficiency of damping due to ion-neutral collisions for the magnetic field profile with power law $\alpha = 0.35$. The solid line is the estimate due to analytic approaches and the triangles represent the estimates obtained from numerical data. 100

5.9 Estimates of the efficiency of damping due to ion-neutral collisions for the magnetic field profile with power law $\alpha = 0.4$. The solid line is the estimate due to analytic approaches and the triangles represent the estimates obtained from numerical data. 100

5.10 Estimates of the efficiency of damping due to ion-neutral collisions for the magnetic field profile with power law $\alpha = 0.6$. The solid line is the estimate due to analytic approaches and the triangles represent the estimates obtained from numerical data. 101

6.1 The initial temperature profile of the model background atmosphere (solid line), along with values taken from the VALC model of the quiet Sun (diamonds). 107

6.2 The initial stratification of the background atmosphere. The dashed line is the temperature, the solid line is the density and the dot-dash line is the gas pressure. All values are normalised to values at the surface, y=0. The height is normalised to the scale height at the surface. 108

6.3 The rise speed at the centre of the flux tube (triangles) along with the theoretical linear evolution (solid line). Velocity is normalised to the Alfvén speed at the surface, and the time is normalised to $t_0 = H_p/v_A$. 113

6.4 The axial field component though the centre of the tube as a function of position at five different times at t=0,10,20,30,40,50, shown by the solid lines in order from left to right. The dashed line shows the ratio of the density to the density at the tube's initial height. 114

6.5 The magnetic pressure at 4 different times in the simulations. Top left:t=28, top right:t=32, bottom left:t=36, bottom right:t=40. 115

6.6 The magnetic pressure (dashed line), gas pressure (thin solid line) and density (thick solid line) as functions of height in the centre of the horizontal domain at time t=30. The density is depleted at the top of the layer, and consequently the magnetic field is holding up denser gas. . . 116

6.7 Left panel: The initial (dashed line) and final (solid line) density as a function of height in the centre of the horizontal domain, for the adiabatic case where no heating/cooling terms are included. Right panel: The initial (dashed line) and final (solid line) temperature as functions of height for the same simulation. All values are normalised to values at the photosphere. 119

6.8 The temperature in the centre of the domain as a function of height for t=0 (thick solid line). Also shown are the final temperature profiles for the case when $\alpha = \infty$ (dashed line), for $\alpha = 1.67$ (dot-dashed line) and $\alpha = 1$ (thin solid line). 120

6.9 The density in the centre of the domain as a function of height for t=0 (lower solid line). Also shown are the final density profiles for the case when $\alpha = \infty$ (upper solid line), for $\alpha = 1.67$ (dot-dashed line) and $\alpha = 1$ (dashed line). 120

6.10 Plasma velocity at a height of 1500 km above the surface as a function of time showing the onset of the magnetic buoyancy instability. The solid line is the adiabatic case and the dashed line is the case non-adiabatic case. 122

6.11 The value of η_c in Ωm as a function of height in the centre of the horizontal domain at times t=40 (lower solid line), t=44 (dot-dash line), t=48 (dash line) and t=52 (upper solid line). The height is normalised to the scale height at the surface. 123

6.12 Total unsigned flux at two different heights as a function of time in the simulation. The two left plots are at heights 1500km, and the two right plots are at 4500 km above the surface. The solid lines are for the FIP model and the crosses are for the PIP model. 124

6.13 Magnetic field strength at t=75 for the fully ionised model (left panel) and partially ionised model (right panel). 126

6.14 Magnetic field strength in the centre of the domain at t=75 for the fully ionised model (solid line) and partially ionised model (dashed line). . . . 126

6.15 Field-lines in x and y given by contours in A_z where $\mathbf{B} = \nabla \wedge \mathbf{A}$. The left panel is the FIP model, the right is the PIP model. Both plots use the same contour levels. 127

6.16 Total perpendicular (dashed line) and parallel current (solid line) integrated across the horizontal domain as a function of height for the initial flux tube configuration All values are normalised. 129

6.17 Total perpendicular current across the domain as a function of height for the FIP model (dashed line) and the PIP model (solid line). All values are given in normalised units. 129

6.18 Total parallel current across the domain as a function of height for the FIP model (dashed line) and the PIP model (solid line). All values are given in normalised units. 130

6.19 Vertical profile of estimates of the terms in Ohm's law in the centre of the horizontal domain at t=75. The solid line is the advection term, the dashed line is the Hall term, and the dash-dot line is the diffusive term due to ion-neutral collisions. 131

7.1 Isovolume of magnetic field strength showing the initial tube configuration. Also shown is a vertical slice of the initial temperature profile. All values are normalised to values at the surface. 137

7.2 Isovolume of magnetic field strength at t=30 showing the Ω-shape formed due to the centre of the tube being more buoyant than the feet. Also shown is a 1D slice of the temperature. 139

7.3 Simulated magnetograms of flux emergence, showing vertical magnetic field in the z=0 plane. The left panel is at t=40 and the right panel is at t=49. All values are normalised to non-dimensional units. 140

7.4 Isosurface of magnetic field strength at t=50, shown from two different angles. All values are normalised to values at the photosphere. 140

7.5 Isosurface of the magnetic field strength in the y=0 plane showing the expansion of the top of the flux tube into the model corona. Top left panel is for t=50, top right t=55, bottom left t=60 and bottom right t=65. All values are normalised to non-dimensional units. 142

7.6 Horizontal velocity along the tube axis. The left panel shows a surface plot of v_x in the x,y plane at the height of the tube axis at t=55. The right panel shows a plot of v_x along the tube axis (y=0) at three different times. Dot-dashed line is for t=45, dashed line is for t=50, solid line is for t=55. 143

7.7 The Cowling resistivity in Ωm as a function of height in the centre of the horizontal domain. The solid line is for t=45, the dashed line is for t=48 and the dash-dotted line is for t=53. The height is given in dimensionless units. 144

7.8 Total unsigned vertical flux (in dimensionless units) as a function of time at two different heights. The upper panel is for $z = 10$ and the lower panel is for z= 30. Solid lines are for PIP and asterisks are for FIP. . . 145

7.9 The total parallel (solid line) and total perpendicular currents at t=0 as a function of height. 146

7.10 The two components of current as functions of height for the fully ionised model (top panel) and partially ionised model (bottom panel). Solid lines are total perpendicular current and dashed lines are total parallel current. 147

A.1 Numerical grid showing the positions of the variables needed to solve the HS equation 155

Acknowledgments

I would like to thank my supervisor Dr. Tony Arber for guidance throughout the last 3 years. I would also like to thank staff and PhD students at the Centre for Fusion, Space and Astrophysics for useful discussions, both scientific and technical. My thanks also to Dr. Maxim Khodachenko at the Space Research Institute (Institut fr Weltraumforschung, IWF) of the Austrian Academy of Sciences for collaboration which contributed to one of the papers published from this work. This work was funded by a PPARC grant.

This thesis was typeset with LaTeX 2_ε[1] by the author.

[1] LaTeX 2_ε is an extension of LaTeX. LaTeX is a collection of macros for TeX. TeX is a trademark of the American Mathematical Society. The style package *utthesis* was used.

Declarations

I hereby declare that the material presented here is all my own work, except where explicitly stated. Some of the work has been published in the following publications.

- Collisional Dissipation of Alfvén Waves in a Partially Ionised Solar Chromosphere. Leake et al.,2005. Astronomy and Astrophysics, 442:1091-1098.

- The Emergence of Magnetic Flux through a Partially Ionised Solar Atmosphere. Leake and Arber, 2006. Astronomy and Astrophysics, 450:805-818.

- Numerical Modeling of Flux Emergence in the Solar Atmosphere: Effects of Partial Ionisation, Leake, 2005. Proceedings of the 11th European Solar Physics Meeting "The Dynamic Sun: Challenges for Theory and Observations" (ESA SP-600). 11-16 September 2005, Leuven, Belgium. Editors: D. Danesy, S. Poedts, A. De Groof and J. Andries. Published on CDROM., p.13.

Abstract

In this thesis techniques are developed for the simulation of partially ionised plasmas in the fluid approximation. These techniques are used to model the evolution of magnetic fields in the partially ionised regions of the solar atmosphere. Single fluid equations for a partially ionised plasma are derived based on the individual equations for each species. A Lagrangian Remap MHD code is then adapted to simulate a plasma of arbitrary degree of ionisation.

The effects of the presence of neutrals on the propagation and damping of Alfvén waves in the solar atmosphere are investigated. Ion-neutral collisions are shown to be an efficient damping mechanism for outwardly propagating Alfvén waves of frequencies greater than 0.1 Hz, showing that high frequency waves in the outer solar atmosphere cannot originate at the surface of the Sun.

Next simulations to show the effects of neutrals on the emergence of magnetic flux from beneath the solar surface into the outer atmosphere are performed. Results from 2D and 3D numerical experiments show that the presence of neutrals increases the amount of magnetic flux that can emerge into the corona. Furthermore, ion-neutral collisions are strong enough to dissipate currents perpendicular to the magnetic field as it emerges. This shows that ion-neutral collisions are a viable mechanism for the formation of force-free ($\mathbf{j} \wedge \mathbf{B} = 0$) coronal magnetic field from sub-surface field, which is not the case when the plasma is assumed to be fully ionised.

Abbreviations

1D: One Dimensional

2D: Two Dimensional

CFL: Courant-Freidrichs-Lewy (condition)

EIT: Extreme Ultraviolet Imaging Telescope

LTE: Local Thermodynamic Equilibrium

FIP: Full Ionised Plasma

Lare: Lagrangian Remap

MBI: Magnetic Buoyancy Instability

MDI: Michelson Doppler Imager

MHD: Magnetohydrodynamics

MPI: Message Passing Interface

PIP: Partially Ionised Plasma

SOHO: Solar and Heliospheric Observatory

TRACE: Transition Region and Coronal Explorer

Chapter 1

Introduction

1.1 The Sun

The Sun is a dwarf star lying on the main sequence of the Hertzprung-Russel diagram, roughly halfway through its lifetime as a main sequence star, which is about 10^{10} years. It has a mass of 2×10^{30} kg, and a radius of 7×10^{8}m. 74% of the mass is made up of Hydrogen, 25% Helium and the rest heavier elements. The main source of energy generation is the fusion of Hydrogen into Helium.

The Sun has played a major role in the advancement of physics and mathematics for the past several centuries. These advancements include Keplers laws, Newtonian theory and gravitation, as well as general relativity. Due to its closeness to the Earth, more is known about the Sun than any other star, which has lead to it being referred to as the *Rosetta stone* of astronomy. The Sun is a ready made laboratory for the study of a wide range of processes and phenomena. These studies have allowed better understanding of the structure and evolution of other stars. Although direct measurements of the interior of the Sun are not possible, a combination of self-consistent models and surface observations have enabled a very detailed understanding of the solar structure to be built up.

The outer layers of the Sun exhibit many interesting and dynamic phenomena which influence our own climate on earth. These phenomena are closely related to the magnetic field of the Sun, which exists on many spatial and temporal scales. The

regeneration of large scale field in the Sun appears to be driven by a combination of differential rotation and turbulent convection. This is commonly referred to as the solar dynamo. The dynamics of the outer layers of the Sun are a direct consequence of the manifestation of these dynamo fields on smaller scales.

The Sun is thus a perfect astrophysical laboratory for the testing of not only atomic and nuclear physics, but high temperature plasma physics and magnetohydrodynamics.

1.2 The Solar Interior

Apart from neutrinos there are no direct observational tools for gleaning information regarding the Sun's internal structure. Therefore models must be constructed to estimate this structure which can be then refined to coincide with known parameters gained from observations, such as mass, radius and luminosity at the surface. This process is called the standard solar model (SSM). It consists of solving the equations of mechanical and thermal equilibrium (e.g., Christensen-Dalsgaard et al. (1996); Bahcall et al. (2001)), and modifying the free parameters to match results with observations. Figure 1.1 shows results from a typical solution, taken from Stix (2002), of temperature, density, pressure and the mean mass of each particle in terms of proton mass, all as functions of radius.

The surface of the Sun undergoes a series of mechanical vibrations with periods around 5 minutes. They can be observed in Doppler shifts on the surface (Leighton et al., 1962). They have been identified as acoustic modes of global pulsations (p-modes), being a superposition of millions of standing waves, each mode having an amplitude of a few cm/s (Ulrich, 1996; Leibacher and Stein, 1971).

Using these observations, information regarding the internal structure of the Sun can be obtained, such as density and sound speed. This process has become known as *helioseismology*. Although helioseismology is a relatively old technique (25 years), there is still some gaps in the knowledge regarding the excitations of these global modes. Excitation and damping of p-modes is though to be due to the convective transfer of energy that occurs in the solar interior from about 0.7 to 1 solar radii from the centre

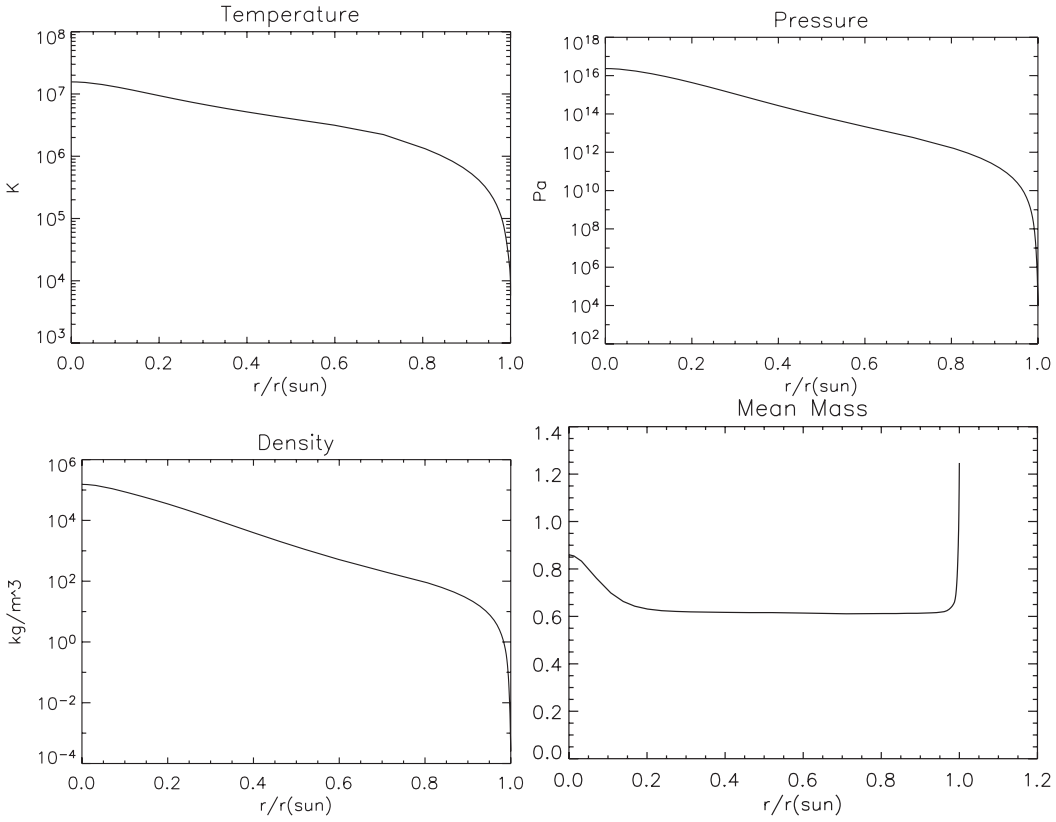

Figure 1.1: The temperature, pressure, density and mean mass calculated from the standard model as a functions of radius for the interior of the Sun.

of the Sun.

Observations of these global oscillation frequencies can provide very stringent constraints on the allowable solar models. There are generally two ways to analyse the data. The first is forward method and uses an equilibrium SSM, which is then perturbed in a linearised theory to obtain eigenfrequencies of solar oscillations, which are then compared to accurate measured frequencies (Elsworth et al., 1990). The fit is rarely accurate, but this kind of method has been used to obtain estimates on the depth of the convection zone, and Helium abundance.

Inversion techniques allow the use of measurements of solar oscillation frequencies to infer the internal structure of the Sun (Gough et al., 1996; Kosovichev et al., 1997). Typical inferred variables are the sound speed and density. These are very accurate, with typical errors for the sound speed being 0.1%. In order to infer the internal temperature, the thermodynamic equilibrium equation must also be included in the SSM. In this way the inverted internal sound speed, density, temperature and composition profiles can match the SSM to high levels of accuracy.

1.2.1 Internal Structure

The core of the Sun extends from the centre to about one quarter of the solar radius. The temperature is 1.5×10^7 K and the density is $1.6 \times 10^5 \mathrm{kg/m^3}$, conditions conducive for the nuclear fusion of Hydrogen into Helium. The majority of the energy release is in the form of gamma rays. At such high densities, these short wavelength photons are quickly absorbed. As a result it takes a particular packet of photons of the order of 10^7 years to reach the surface via absorption and emission in the radiative zone.

Travelling outwards the next region is the radiative zone. The energy generated in the core is transported as photons which suffer consecutive absorption/emission. Photons are heavily absorbed at a radius of about 0.7 solar, and the subsequent heating drives convection above.

The convection zone extends from 0.7 solar radii to the surface. Convection is where internal energy is transported along with the motion of matter. At a depth of about 200 000 km below the surface, convection becomes the dominant mechanism of

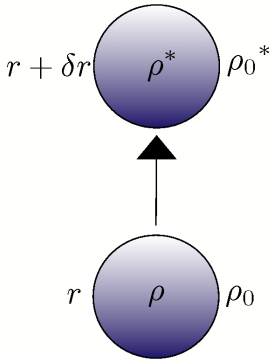

Figure 1.2: A parcel of gas is adiabatically lifted to a region of different density.

transport of energy.

One way of describing convection is known as *mixing length theory*, where parcels of gas travel a certain distance and then deposit their excess heat. This simple way of thinking about convection gives a way of describing the convective flux of energy. In this approach, convective motion is overturning. Parcels of gas are heated, rise and deposit their energy and then fall back down.

When a parcel of gas is lifted from it's position, it is either heavier or lighter than its surroundings. In the latter case it continues to rise (this is called *convectively unstable*), in the former case it falls back down (*convectively stable*). The criteria for convective instability was first derived by Schwarzschild in 1906.

Consider a parcel of gas at height r which has risen to a distance $r + \delta r$ (see figure 1.2). The density of the parcel is now $\rho^* = \rho + \delta\rho$, and must be compared to the density of the surrounding gas ${\rho_0}^* = \rho + \triangle\rho$. The condition for convective instability is simply

$$\delta\rho < \triangle\rho. \tag{1.1}$$

It is assumed that the motion is sufficiently fast that the parcel behaves adiabatically, but still sufficiently slow so that at each point the internal pressure is matched to the local ambient pressure. This is reasonable whenever the time scale of energy exchange is longer than the sound transit time across the parcel. The adiabatic condition implies

that

$$\frac{\delta\rho}{\rho} = \frac{1}{\gamma}\frac{\delta P}{P} \tag{1.2}$$

where γ is the ratio of specific heats. The atmosphere is assumed to be an ideal gas $P = \rho kT/\mu_m$, where μ_m is the mean mass so that

$$\frac{\triangle\rho}{\rho} = \frac{\triangle P}{P} - \frac{\triangle T}{T} \tag{1.3}$$

where changes in the mean mass have been neglected. The effects of changes in μ_m are stabilising, but the interior of the Sun can still be stable against convection even when these effects are ignored. The condition for instability can now be written as

$$\frac{1}{\gamma}\frac{\delta P}{P} < \frac{\triangle P}{P} - \frac{\triangle T}{T}. \tag{1.4}$$

As the pressure in the gas parcel responds quickly to match the surroundings, $\delta P = \triangle P$ and the criteria becomes

$$\frac{\triangle T}{T} < \frac{\gamma - 1}{\gamma}\frac{\triangle P}{P} \tag{1.5}$$

and the critical temperature gradient for convection is

$$\frac{dT}{dr} < \frac{\gamma - 1}{\gamma}\frac{T}{P}\frac{dP}{dr} = \left(\frac{dT}{dr}\right)_a \tag{1.6}$$

where the RHS is called the adiabatic temperature gradient.

In the Sun the temperature gradient and adiabatic gradient are both negative. Hence for instability to occur, the temperature gradient must be steeper than the adiabatic gradient.

If the temperature gradient is not steeper than the adiabatic gradient, then the original equilibrium is stable and the parcel effectively oscillates about the equilibrium position with a frequency N, called the *Brunt-Wäisälä* frequency which is given by

$$N^2 = -g\left[\frac{(\gamma - 1)}{\gamma}\frac{1}{P}\frac{dP}{dr} - \frac{1}{T}\frac{dT}{dr}\right] \tag{1.7}$$

so that the condition for instability is equivalent to $N^2 < 0$. A gas that is convectively unstable is also called *super-adiabatic*, and one that is stable *sub-adiabatic*.

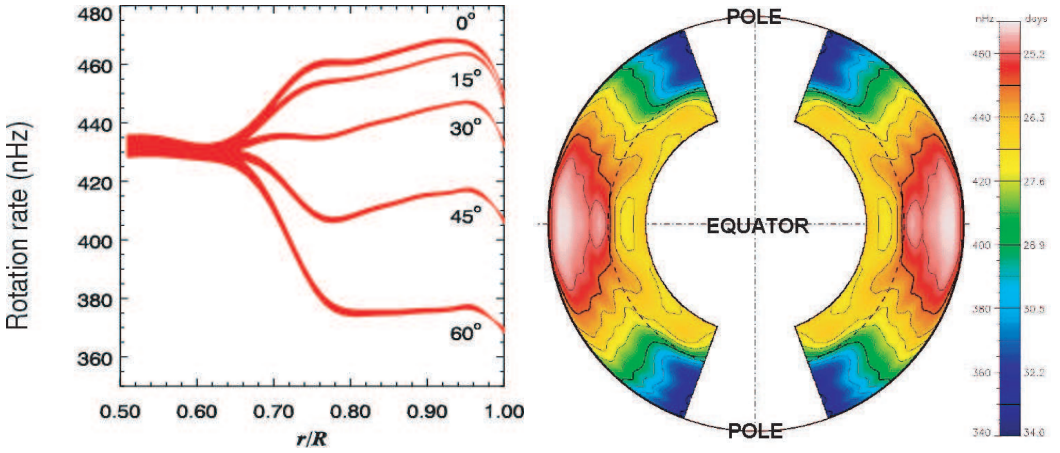

Figure 1.3: Left panel: The rotation rate in nHz at five different latitudes as functions of depth. Right Panel: The rotation rate as a function of radius and latitude. Courtesy National Solar Observatory.

1.2.2 Internal Rotation

Helioseismology has also made it possible to determine the rotation rate in the interior of the Sun from the rotational splittings of oscillation frequencies (for a comprehensive review see Antia (2003)). The splitting coefficients can be used to obtain the rotation rate as a function of height and latitude.

The differential rotation seen on the surface of the Sun continues through the convection zone, while in the interior the rotation rate appears to be relatively uniform (Thompson et al., 1996; Schou et al., 1998). As can be seen in figure 1.3, there is a transition region near the base of the convection zone, at radius $R = 0.705R_\odot$, where there is strong shear flows due to the change from differential rotation to solid body rotation. This region is called the *tachocline*, and is important for the Sun's dynamo, the regeneration of magnetic field in the interior of the Sun. There is also a shear layer at $r = 0.94R_\odot$, where the rotation rate increases with depth, and this could also play a role in the solar dynamo.

1.3 The Solar Atmosphere

The Solar atmosphere is a rarefied, hot (up to MK) plasma which shows a large amount of interesting phenomena. The radiation from the solar atmosphere can be observed in the visible range, UV and X-rays. This means its structure can be inferred from direct imaging using various observational instruments, both ground based and space based. The atmosphere of the Sun is generally split into three distinct regions: the photosphere, chromosphere and corona (see figure 1.4).

The photosphere (from the Greek for light) is a thin region, some 500 km thick, through which the temperature falls from the surface value of 6500 K to the minimum value in the atmosphere of 4300 K. A typical photospheric density is about $10^{-4}\mathrm{kg/m^3}$. The radiation goes from optically thick to optically thin in the visible spectrum in this region, which is why it can be seen with the naked eye.

The chromosphere (Greek for colour) is the coloured sphere that can be seen just before and after an eclipse. It is between two and three thousand km thick and got its name from the prominent red emission of the H_α line of neutral Hydrogen at 6563 Å. The temperature here rises from the minimum to about 2×10^4 K.

Further up, the temperature rises sharply to about 2 MK, in a very thin region known as the transition region. This is the start of the corona. The corona is so hot it is now observable in soft X-rays. It is also very sparse, being some 8 orders of magnitude less dense than the photospheric plasma.

This inversion in the temperature gradient in the chromosphere and subsequent large increase in temperature in the solar corona raises some important questions. One would expect the temperature to fall off with radius from the surface, as energy is radiated away. However, there is a rise in temperature from a few thousand K to MK. There must be some mechanism which heats the plasma at these radii.

The heating of the chromosphere is thought to be related to acoustic modes generated in the solar interior. The convection zone beneath the surface is a turbulent flow and therefore capable of generating acoustic waves which propagate in all directions. Because of the strong density decrease with radius, outwardly propagating waves will increase in amplitude due to energy conservation. These waves will eventually form

shocks, and these shocks dissipate their energy into the chromosphere and heat the plasma there. The upper chromosphere requires more heating and other types are waves are thought to provide this heating. It has long been known that strong magnetic fields exist in the solar atmosphere (Hale, 1908). Indeed as will be shown in later sections, the strong activity seen in the solar atmosphere is due to the magnetic fields present. In the presence of magnetic field, there is a new class of waves called magnetohydrodynamic (MHD) waves, which can carry energy from the surface into the upper chromosphere and dissipate their energy by various mechanisms.

The heating of the corona is far from understood and is a topic of much interest today. Both wave related and non-wave heating mechanisms have been suggested as possible mechanisms for the coronal heating problem (Erdélyi, 2005). One of the main candidates is magnetic reconnection. The magnetic fields present in the solar atmosphere are displaced by motions of the plasma and this can cause field lines of nearby fields to approach one another and reconnect. At the point of reconnection energy is dissipated into the plasma, and this heats it up.

There is still some debate as to which is the most likely candidate for coronal heating. As well as reconnection the damping of MHD waves by various mechanisms such as resonant absorption and mode-coupling, as well as turbulent and viscous heating have all been suggested. It is most likely that all the proposed mechanisms contribute to the heating in some way which gives the corona the temperatures observed. For a review of the coronal heating problem as it stands today see Ulmschneider and Musielak (2003); Erdélyi (2005); Klimchuk (2006).

The temperatures in the solar atmosphere can be inferred directly from observations. Vernazza et al. (1981) used extreme ultra violet (EUV) observations to determine models for the photosphere, chromosphere, and transition region. This was done by solving the statistical equilibrium, hydrostatic equilibrium and radiation equations to obtain the temperature and density stratification, as a function of height, which gave spectrum closest to the observed ones. Figure 1.5 shows calculated temperature and density profiles based on observations of EUV wavelength emission of the quiet Sun (referred to in Vernazza et al. (1981) as the VALC model).

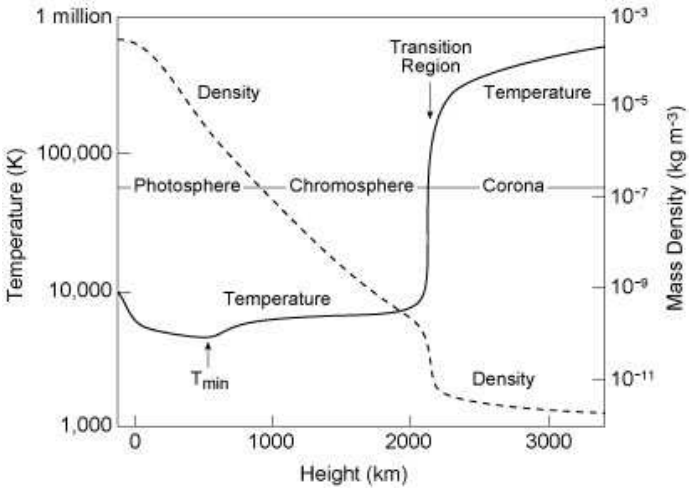

Figure 1.4: The temperature and density in the solar atmosphere. Courtesy Eugene Avrett, Smithsonian Astrophysical Observatory.

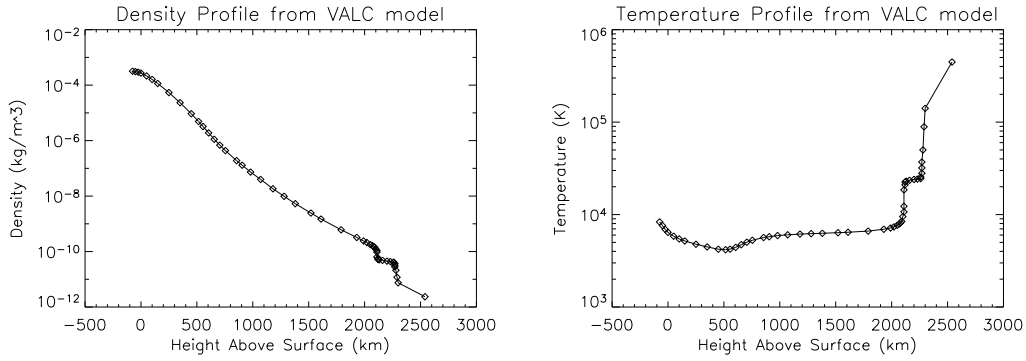

Figure 1.5: Density (left panel) and temperature (right panel) profiles in the low solar atmosphere showing the photosphere, chromosphere and transition region (TR). Values were obtained from the VALC model of the quiet Sun.

1.4 Plasma Physics

If the temperature of a gas is increased beyond a certain limit, it does not remain a gas: it enters a regime where the thermal energy of its constituent particles is so great that the electrostatic forces which ordinarily bind electrons to atomic nuclei are overcome. Instead of a hot gas composed of electrically neutral atoms, there are two populations composed of electrons and ionised nuclei. This is a plasma, and its most notable feature is its high electrical conductivity.

The Sun is made of plasma, as are most stars. In addition, the Earth is surrounded by the plasma of the magnetosphere. On earth, plasmas occur naturally in lightning and the aurora. Indeed the plasma state can be said to dominate the visible universe. The practical terrestrial applications of plasmas are also extensive ranging from small scale production of electrical components to thermonuclear fusion power generated in magnetically confined plasmas. The study of plasmas is therefore a worthwhile field in modern physics.

There has been much development in theoretical techniques to describe plasmas. These techniques can be broadly split into two regimes. The first is based on treating a plasma in a similar way as a gas is treated. A plasma is a collection of charged particles, each moving under the influence of the magnetic fields created by all the other particles. This leads to plasma kinetic theory, which has been extremely useful in applications where particle interactions are important. The second regime is provided by fluid dynamics. Looking at the macroscopic properties of a plasma, it resembles a fluid with a high electrical conductivity, eg. a liquid metal. This fluid interacts with the electromagnetic fields permeating it, and can be described by the equations of Magneto-Hydro-Dynamics (MHD). This approach is useful for studying large scale phenomena in plasmas. The MHD description can be obtained from the kinetic theory, and requires a number of assumptions and consequently drops certain physics as macroscopic properties are obtained from averaged microscopic properties of the plasma.

Before describing the MHD approach to plasmas it is pertinent at this point to introduce some basic plasma properties which will be useful in later sections.

1.4.1 Plasma Properties

Single particle motion

The charged particles that constitute a plasma are influenced by the electro-magnetic (EM) fields present in the plasma. One way of looking at plasmas is as a collection of particles, each subject to its own governing EM fields which are created by the summation of EM fields due to the motion of other particles, as well as by external drivers. The equation of motion for each particle of charge q, having velocity $\mathbf{v}$, in external electric field $\mathbf{E}$ and magnetic field $\mathbf{B}$ is

$$m\dot{\mathbf{v}} = q(\mathbf{E} + \mathbf{v} \wedge \mathbf{B}) \tag{1.8}$$

$$\dot{\mathbf{x}} = \mathbf{v}. \tag{1.9}$$

Consider the motion of a single charged particle in a uniform magnetic field, with $\mathbf{E} = 0$. Splitting the equation of motion into components parallel ($\|$) and perpendicular ($\perp$) to the magnetic field gives

$$\ddot{\mathbf{v}}_\perp = -{\omega_c}^2 \mathbf{v}_\perp \tag{1.10}$$

$$\ddot{\mathbf{v}}_\| = 0 \tag{1.11}$$

with

$$\omega_c = \frac{eB}{m} \tag{1.12}$$

known as the *gyrofrequency*. This motion consists of circular motion about a fixed point known as the *guiding centre*, and the constant motion of this guiding centre along the field line. In other words the particle traces a helix about the magnetic field-line. The *gyro-radius* is the radius of this helix and is

$$r_L = \frac{v_\perp}{\omega_c} \tag{1.13}$$

When other forces are present such as the electrostatic force, or when the magnetic field is not constant, the guiding centre undergoes more complex motions.

Collective behaviour

Plasmas exhibit collective behaviour. To exhibit what is meant by collective behaviour, it is necessary to introduce the concept of *Debye screening*. If a positive test charge Ze is placed in a plasma, it will attract electrons and repel ions in such a way that its Coulomb potential $\phi_c = Ze/4\pi\epsilon_0 r$ is attenuated at distance beyond a certain distance which is called the *Debye length*. To calculate the Debye length the potential $\phi(r)$ generated by this test charge needs to be found. Assuming the plasma is in thermal equilibrium, the ion and electron distribution distributions are of the Maxwell-Boltzmann form

$$f_j(\mathbf{x}, \mathbf{v}) = n_0 exp\left(-\frac{mv^2}{2k_BT} + \frac{e_j\phi}{k_BT}\right) \tag{1.14}$$

where $j = i, e$ and the densities are $n_j(r) = n_0 exp(e_j\phi(r)/k_BT)$, with k_B Boltzmann's constant. The potential must satisfy Possion's equation

$$\nabla^2\phi = \frac{1}{\epsilon_0}\rho_r \tag{1.15}$$

where $\rho_r = \sum_j e_j n_j(r)$. Assuming spherical symmetry and that $e\phi/k_BT << 1$ this has solutions

$$\phi = \frac{A}{r} exp\left(-\frac{r}{\lambda_d}\right) \tag{1.16}$$

where A is a constant and

$$\lambda_d = \left(\frac{\epsilon_0 k_B T}{2n_0 e^2}\right)^{\frac{1}{2}} \tag{1.17}$$

is the Debye length. To find the constant A the solution must be matched to the bare potential of the test charge at a distance r which is small compared to the interparticle distance $n_0^{-\frac{1}{3}}$. This gives $A = Ze/4\pi\epsilon_0$ provided the condition

$$n_0^{-\frac{1}{3}} << \lambda_d \tag{1.18}$$

holds. This condition stipulates that the number of particles in a debye sphere (sphere of radius λ_d) is much greater than one. This condition needs to be satisfied if an ionised gas is to be called a plasma. Another condition is that the typical length scale of the plasma L must be greater than the Debye length

$$L >> \lambda_d. \tag{1.19}$$

Another example of collective behaviour in plasmas is plasma oscillations. Consider a collection of ions and electrons, where $m_e << m_i$, such as a Hydrogen plasma. Now imagine that an electron distribution in a quasi-neutral collection of ions and electrons is displaced by a small amount x. The electrons will experience a restoring force $\mathbf{F} = -e\mathbf{E}$ where the electric field $\mathbf{E}$ is created by a higher concentration of positive charge, Q, left by the electrons. The electron will oscillate about their equilibrium position. Using Gauss' law

$$\int_S \mathbf{E}.\mathbf{dS} = \frac{Q}{\epsilon_0} \tag{1.20}$$

where S is a Gaussian surface enclosing the displaced electron distribution, $\mathbf{dS}$ its normal, and ϵ_0 the permittivity of free space, the restoring electric field can be found.

$$E = \frac{enx}{\epsilon_0} \tag{1.21}$$

The equation of motion of the electron distribution is then

$$m_e\ddot{x} = -eE \tag{1.22}$$

or

$$\ddot{x} + \frac{e^2 n}{\epsilon_0 m_e}x = 0 \tag{1.23}$$

which represents simple harmonic motion about the equilibrium position with frequency

$$\omega_{pe} = \left(\frac{e^2 n}{\epsilon_0 m_e}\right)^{\frac{1}{2}} \tag{1.24}$$

which is known as the *electron plasma frequency* and is the fundamental frequency of plasmas. If

$$\tau >> \frac{1}{\omega_{pe}} \tag{1.25}$$

where τ is a characteristic timescale, then these oscillations can be ignored and the plasma is said to be *quasi-neutral* $n_i = n_e$.

1.4.2 The MHD Approximation

The evolution of particles in a plasma is formally described by the Boltzmann equation, which details the evolution of a distribution function in phase space and time.

$$\frac{\partial f_\alpha}{\partial t} + \mathbf{v}.\nabla_r f_\alpha(\mathbf{r},\mathbf{v},t) + \frac{\mathbf{F}_\alpha}{m_\alpha}.\nabla_v f_\alpha(\mathbf{r},\mathbf{v},t) = \left(\frac{\partial f_\alpha}{\partial t}\right)_{coll} = C_\alpha \tag{1.26}$$

$f_\alpha(\mathbf{r}, \mathbf{v}, t)$ is the density of particles having velocity $\mathbf{v}$ at position $\mathbf{r}$ at time t. The forces acting on the particles can be separated into the EM forces due to electric and magnetic fields $\mathbf{F}_\alpha = q_\alpha(\mathbf{E} + \mathbf{v}_\alpha \wedge \mathbf{B})$ and forces due to collisions C_α. ∇_r and ∇_v are the gradient vectors in space and velocity respectively.

A complete study of a plasma involves solving the Boltzmann equation for the particles and the Maxwell equations for the EM fields. Once these are solved the macroscopic quantities of interest can be found by integration of f_α over velocity space.

The full set of Boltzmann-Maxwell equations are virtually impossible to solve except for trivial cases. The situation is very complicated when collisions are important, as the Boltzmann equation is actually an integro-differential equation. Thus simpler models, albeit with a smaller scope of applicability, have been adopted. The MHD approximation is such an approach. Magneto-Hydro-Dynamics on a basic level treats a plasma as a conducting fluid permeated by magnetic field. This magnetic field may be externally applied, produced by currents flowing in the fluid, or a combination of both. The governing equations of MHD resemble the equations describing a fluid, such as the Euler equation, but with the action of the magnetic field on the plasma flows included (the *Lorentz force*).

The MHD equations are arrived at by taking moments of the Boltzmann equation and integrating over velocity space. This gives fluid equations for each species of the plasma. These fluid equations can be combined into single fluid equations for the whole plasma by averaging over parameters such as velocity and momentum. For a fully ionised plasma this is relatively simple as the heavy ions carry almost all the momentum, and the average velocity is determined by their velocity. The MHD equations are given here in eulerian form.

$$\frac{\partial \rho}{\partial t} = -\nabla.(\rho \mathbf{v}) \tag{1.27}$$

$$\frac{\partial \rho \mathbf{v}}{\partial t} = -\nabla.(\rho \mathbf{v}) + \mathbf{j} \wedge \mathbf{B} - \nabla P + \nabla.\mathbf{\Pi} \tag{1.28}$$

$$\frac{\partial \mathbf{B}}{\partial t} = \nabla \wedge (\mathbf{v} \wedge \mathbf{B}) - \nabla \wedge (\eta \mathbf{j}) \tag{1.29}$$

$$\frac{\partial \rho \epsilon}{\partial t} = -\nabla.(\rho \epsilon \mathbf{v}) - P \nabla.\mathbf{v} + \eta j^2 + \Pi_{ij} S_{ij} \tag{1.30}$$

ρ is the mass density of the plasma as a whole, $\mathbf{v}$ is the centre of mass velocity, P is

the gas pressure, $\mathbf{B}$ is the magnetic field, and $\mathbf{j} = \frac{\nabla \wedge \mathbf{B}}{\mu_0}$ the current density, where μ_0 is the permeability of free space. ϵ is the total specific internal energy density, given by $\epsilon = \frac{P}{(\gamma-1)\rho}$. $\mathbf{\Pi}$ is the stress tensor which, in the absence of magnetic field, has components

$$\Pi_{ij} = \nu(s_{ij} - \frac{1}{3}\delta_{ij}\nabla.\mathbf{v}) \tag{1.31}$$

and

$$s_{ij} = \frac{1}{2}(\frac{\partial v_i}{\partial x_j} + \frac{\partial v_j}{\partial x_i}). \tag{1.32}$$

When magnetic field is present, the stress tensor is slightly more complicated (Braginskii, 1965).

Equation (1.27) is the conservation of mass, equation (1.28) is the conservation of momentum which looks similar to the Navier Stoke's equation for a fluid but with the Lorentz force added. Equation (1.30) is the conservation of internal energy density.

The Lorentz force can be split into two terms via

$$\mathbf{j} \wedge \mathbf{B} = \frac{1}{\mu_0}\left[(\nabla \wedge \mathbf{B}) \wedge \mathbf{B}\right] = \frac{(\mathbf{B}.\nabla)\mathbf{B}}{\mu_0} - \nabla\left(\frac{B^2}{2\mu_0}\right). \tag{1.33}$$

The first is *magnetic tension*, which resists bending of magnetic field lines and the second is *magnetic pressure* which represents the magnetic fields pressure on the plasma.

An important parameter in MHD is the so-called *plasma* β. Consider the the Lorentz force and the pressure gradient in the momentum equation. The plasma β is defined as

$$\beta = \left|\frac{\nabla P}{\mathbf{j} \wedge \mathbf{B}}\right| \sim \frac{P}{\frac{B^2}{\mu_0}}. \tag{1.34}$$

If the magnetic pressure is greater than the gas pressure, then β is much less than unity. So for a low beta plasma in equilibrium, the momentum equation, neglecting gravitational and viscous terms reduces to

$$\mathbf{j} \wedge \mathbf{B} \approx 0. \tag{1.35}$$

Equation (1.29) is known as the induction equation. It is a result of combining Faraday's law of induction

$$\frac{\partial \mathbf{B}}{\partial t} = -\nabla \wedge \mathbf{E} \tag{1.36}$$

and a closing equation called Ohm's law. Ohm's law describes how the currents in the plasma are driven by EM fields and retarded by collisions between particles. It can be thought of as simply relating the current density to the electric field. As will be shown in future chapters, this can be extremely complicated. In resistive MHD the only terms retained are the electric field in the rest frame of the fluid, the current density and the resistivity, which is related to the momentum transfer between particles during collisions.

$$\mathbf{E} + \mathbf{v} \wedge \mathbf{B} = \eta \mathbf{j} \tag{1.37}$$

Combining Ohm's law and Faraday's equation gives the resistive induction equation. This can be recast using the definition of current density $\mathbf{j} = \frac{\nabla \wedge \mathbf{B}}{\mu_0}$.

$$\frac{\partial \mathbf{B}}{\partial t} = \nabla \wedge (\mathbf{v} \wedge \mathbf{B}) + \frac{\eta}{\mu_0} \nabla^2 \mathbf{B} \tag{1.38}$$

An important parameter of resistive MHD is the *magnetic Reynolds number*, given by the ratio of the two terms in the induction equation. The first is the advection term $\mathbf{v} \wedge \mathbf{B}$ and the second is the diffusion term $\eta \frac{\nabla^2 \mathbf{B}}{\mu_0}$.

$$R_m \approx \frac{\mu_0 L v}{\eta} \tag{1.39}$$

where L and v are characteristic lengths and velocities. If R_m is high then the diffusion term is negligible and the evolution of the magnetic field is determined by advection by the fluid velocity. In this regime, called *ideal MHD*, the magnetic field lines are essentially *frozen in* to the field. If R_m is low then the advection term is negligible and equation (1.38) becomes a diffusion equation for the magnetic field.

In addition to these equation, an equation of state is needed, which relates the pressure, specific internal energy density and mass density. A simple example would be the ideal gas equation, which, within the context of MHD can be written as

$$P = \rho \epsilon (\gamma - 1). \tag{1.40}$$

The MHD equations (1.27)-(1.30) can also be written in Lagrangian form

$$\frac{D\rho}{Dt} = -\rho\nabla.\mathbf{v} \tag{1.41}$$

$$\rho\frac{D\mathbf{v}}{Dt} = \mathbf{j}\wedge\mathbf{B} - \nabla P + \nabla.\mathbf{\Pi} \tag{1.42}$$

$$\frac{D\mathbf{B}}{Dt} = (\mathbf{B}.\nabla)\mathbf{v} - \mathbf{B}(\nabla.\mathbf{v}) - \nabla\wedge(\eta\mathbf{j}) \tag{1.43}$$

$$\rho\frac{D\epsilon}{Dt} = -P\nabla.\mathbf{v} + \eta j^2 + \Pi_{ij}S_{ij} \tag{1.44}$$

where

$$\frac{D}{Dt} = \frac{\partial}{\partial t} + \mathbf{v}.\nabla \tag{1.45}$$

is the Lagrangian derivative.

Conditions of applicability of MHD

The MHD equations treat a fully ionised plasma as a single fluid *threaded* by magnetic field lines. Hence the general condition for a fluid approach should be satisfied in that the plasma be collision dominated. This means that the smallest scale δx considered must be much larger than the mean free path of collisions λ_f.

$$\lambda_f << \delta x \tag{1.46}$$

This smallest scale would typically be the scale over which the fluid variables change. If condition (1.46) is satisfied then the MHD timescale δt is long enough for there to be sufficient collisions between particles. This also means that δt is longer than the time required for light to cross the system, and justifies the neglect of the displacement current in the equation for the current density

$$\mathbf{j} = \frac{\nabla\wedge\mathbf{B}}{\mu_0}. \tag{1.47}$$

The MHD approach also assumes the plasma is *quasi-neutral* in that there is no local build up of charge. This is satisfied if the Debye length λ_D is much smaller than the MHD length scale.

$$\lambda_D << \delta x \tag{1.48}$$

In addition MHD also assumes that the current is carried by mobile electrons, while the fluid momentum is carried by the heavier ions. This is true if the length scale is much larger than the ion gyro-period.

$$r_{Li} << \delta x \tag{1.49}$$

In order to justify modeling the Sun in the MHD limit these criteria must be satisfied for the solar plasma. The requirement that relativistic effects are negligible is generally true in the solar plasma as thermal velocities are at most two orders of magnitude smaller than the speed of light. The ion-gyrofrequency in the solar atmosphere is about 50 kHz for protons, and as the processes and phenomena investigated in this thesis occur on time scales greater than a second, typical time scales are longer than the gyro-period, and therefore typical length scales are longer than the gyro-radius so that (1.49) is satisfied. In addition condition (1.48) is satisfied due to the large length scales of the solar plasma. In the solar corona, the low densities mean that the mean free path can be very large, so that condition (1.46) is not strictly applicable. However, as the plasma is of low density, collisions are generally not a significant contributor to the behaviour of the plasma, and MHD is still a good working model for the solar atmospheric plasma.

1.5 Solar Activity and Magnetism

For 2000 years astronomers have been attracted by solar activity: At first by observations of sunspots, including the variation in number and appearance. Later by actual sunspot structure, and later still by observations in ultraviolet of structures in the atmosphere above sunspots. It is well accepted that the activity seen on the surface and in the atmosphere (the chromosphere, corona and solar wind) is almost entirely caused by the magnetic field of the Sun.

1.5.1 Sunspots

Perhaps the simplest and most easily observable activity one can observe on the solar surface are *sunspots*. When viewing the Sun with the naked eye, the observer sees the

photosphere. This is where the majority of white light radiation from the Sun originates from. The plasma here goes from optically thick to optically thin in the visible spectrum over a thin region (500 km). Rather than being homogeneous the surface of the Sun has several dark spots, known as *sunspots*. They are observed by Zeeman splitting of spectral lines. It was suggested by Hale (1908) that these spots appear dark because of the presence of magnetic fields. Magnetic fields of intensities of the order of KG can produce such a splitting of the observed lines. In more recent times, the Zeeman effect has been used to detect weaker magnetic fields (Babcock, 1953), as well as all 3 components of the field (Severny, 1964).

Sunspots are typically $2 - 6 \times 10^7$m in size. They appear dark because they are actually cooler than their surroundings. Typical sunspots temperatures are 3700K with the photospheric temperature being 6000K. Sunspots are cooler because the presence of magnetic field can inhibit the flow of energy by convection in the underlying convection zone.

The sunspot can be divided into two regions: the umbra, where the magnetic field is mostly vertical, and the penumbra, where the field is almost horizontal. These regions can be seen in figure 1.6. The cool dark umbra is at the centre, and a distinct radial structure can be seen in the penumbra. Sunspots can be explained by foot points of vertical flux tubes which extend into the atmosphere above. The plasma pressure drops off with height in the solar atmosphere, and since total horizontal pressure balance must be maintained, the magnetic pressure must also decrease. In order that the total magnetic flux in the tube be constant, then the radius of the tube must increase with height. Thus the sunspot must expand outwards rapidly with height, which explains the existence of the penumbra.

1.5.2 Granulation

Looking at the surface of the Sun, with a telescope of around 20cm or greater in diameter, a cellular pattern is seen on the surface of the Sun. This pattern, called *granulation*, was first observed back in the 19th century by Sir William Herschel. A typical granular pattern is shown in figure 1.6. Bright granules are seen on top of a

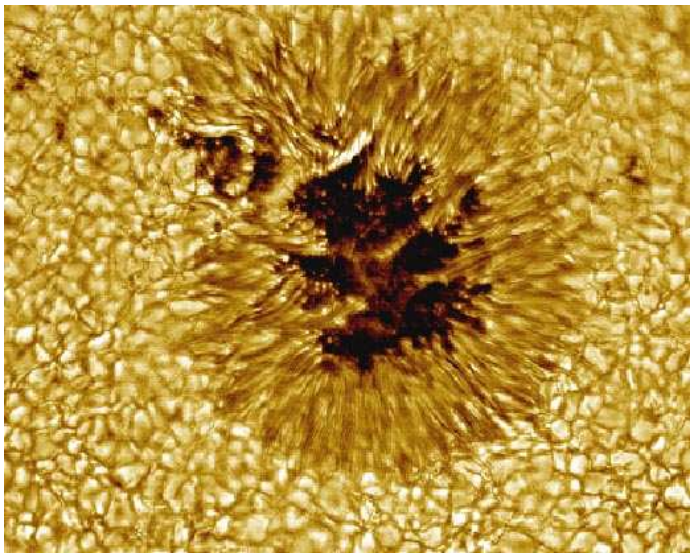

Figure 1.6: Sunspot structure showing the dark umbra in the centre of the filamentary penumbra and the background granulation pattern. Courtesy Vacuum Tower Telescope, National Solar Observatory and National Optical Astronomy Observatory.

background of dark inter-granular lanes. Granules are hot upward moving parcels of gas, while the inter-granular lanes are cooler, downward flowing plasma. Granulation is merely a consequence of the convection going on in the convection zone beneath the surface. Typical granule sizes go up to 1000 km. Granulation is a continuously ongoing process. Granules merge, die out and new ones reform, with a typical lifetime of a granule being up to 20 minutes.

Looking over larger and larger scales, other scales of granulation can be seen. By tracking 'active' granules, i.e regions which have continuous reproduction of granules, a bigger scale of granulation known as *meso-granulation* can be detected. The reason for this larger scale is not exactly known, but it is merely thought of as a larger version of granulation.

Leighton et al. (1962), using Doppler shift measurements of radiation from the surface, found a cellular pattern distributed uniformally over the Sun with a typical spacing of 30000km between cell centres. This *super-granulation* is generally interpreted as large scale convection currents that originate deep in the convection zone (Simon and

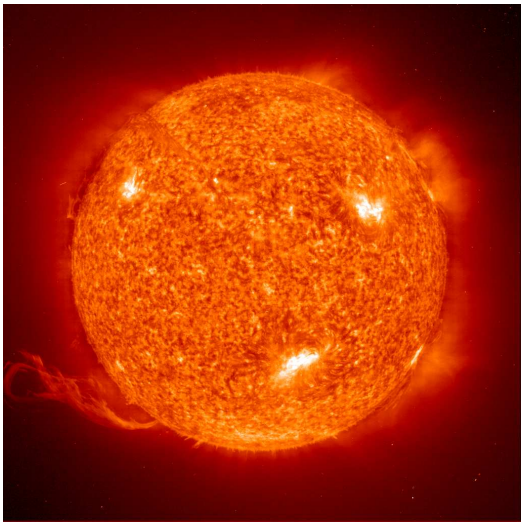

Figure 1.7: SOHO-EIT image from 14 September 1997 showing a huge eruptive prominence in the resonance line of singly ionised helium (He II) at 304 Angstroms in the extreme ultraviolet. The material in the eruptive prominence is at temperatures of 60,000 - 80,000 K, much cooler than the surrounding corona, which is typically at temperatures above 1 million K. Courtesy European Space Agency and NASA.

Leighton, 1964).

1.5.3 Coronal Structures

As the temperature of the solar atmosphere increases with height, the plasma undergoes the transition to optically thin in the ultra-violet wavelength range, and so UV observations are required to observe the plasma at these heights. Figure 1.7 shows an image from the Extreme ultraviolet Imaging Telescope (EIT) on the Solar Heliospheric Observatory spacecraft (SOHO). The regions directly above sunspots appear as bright regions, showing that the plasma is either denser or hotter and hence visible in the EIT bandpass.

These active regions are directly related to the magnetic fields associated with the sunspots below. Looking more closely at these active regions in the corona a large amount of structure can be seen. Figure 1.8 shows a UV image taken from the Transition Region and Coronal Explorer (TRACE). Hot plasma is being held in loop-like structures

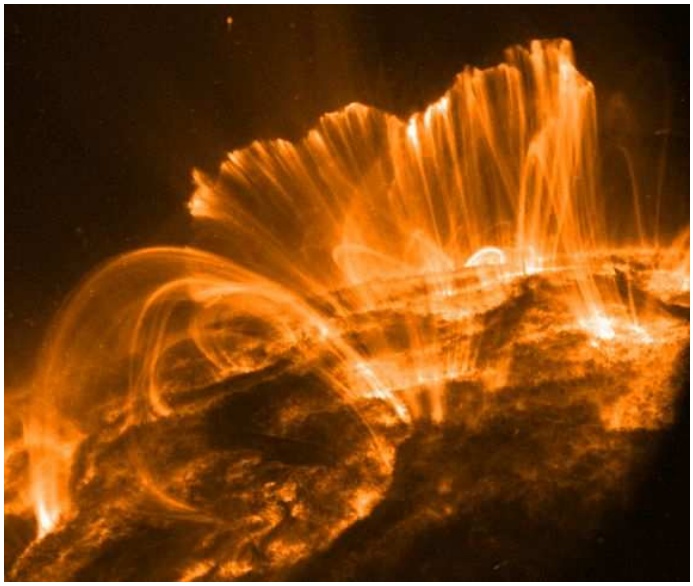

Figure 1.8: A coronal arcade taken by TRACE on November 15th 2000. Courtesy TRACE consortium and NASA.

called *coronal loops*. These loops are caused by the magnetic field lines of the magnetic field in active regions. Typical loop lengths are 10^7 m. As can be seen in figure 1.8 these loops can form arcade structures. The motions of the plasma at the solar surface cause the footpoints of these loops to move around which can cause field lines to entangle and reconnect. This reconnection is a possible source of heating of the solar corona.

1.5.4 Prominences

Prominences (also called filaments) are regions of cool dense plasma supported high in the corona by magnetic field. They appear as dark-ribbon like structures on the disk of the Sun, but when observed on the limb they are brighter than the surroundings as the corona is of such low density, and the intensity of radiation is proportional to the square of the density. Prominences can be split into two broad types. Quiescent prominences are located away from active regions, and have lifetimes of about 200 days. They have temperatures between 5000 and 10000 K, and typical number densities of $10^{16} - 10^{17}\mathrm{m}^{-3}$. Typical dimensions of quiescent prominences are lengths of 2×10^8m,

widths of 6×10^6m and heights of 5×10^7m. Active region prominences have a much smaller lifetime, and are denser ($> 10^{17}\mathrm{m}^{-3}$) and smaller by factors of about 3-5. Typical measurements of the lines of sight magnetic field for prominences are around 10G. A limb prominence can be seen in figure 1.7.

For prominences that exist for many Alfvén time scales, they can be regarded as globally stable equilibria. When critical conditions are met, they can become unstable and erupt. Oscillations have also been observed in prominences (Oliver and Ballester, 2002).

One problem associated with prominences is to explain how a cool plasma can be formed in the surrounding hot plasma. A possible mechanism is a thermal instability, originally suggested by Parker (1953). This is based on that fact that, for certain temperatures, a small amount of cooling can actually increase the radiative loss of energy, thus causing a run-away instability. The instability stops when the radiative loss function no longer increases with decreasing temperature.

1.5.5 Flares

Solar flares are rapid brightenings in H_α in the chromosphere due to the release of a large amount of magnetic energy. The largest of flares are amongst the most violent events in the solar system. A typical large flare releases $10^{25}J$ of energy in the period of about an hour. The only possible source of this energy in the corona is the magnetic field (Hood, 1996). Flares come in two categories, *two-ribbon flares* and *simple-flare loops*.

Two-ribbon flares are large events associated with the eruption of active-region filaments where there is significant restructuring of the magnetic field. Two bright bands of emission in H_α are seen, which give the two-ribbon flare its name. This phase of the flare involves the most energy release. Afterwards, post-flare loops are seen connecting the two regions of emission.

Simple-loop flares are much smaller, releasing only $10^{23}J$. They consist of single loops or groups of loops that brighten without any major change in their overall shape.

The modeling of flares is an active areas of solar physics, as there exist no detailed

models that can predict all the features present in a typical flare. One common feature of flare models is that the energy is stored in coronal magnetic field. Motions on the surface can inject stress into the magnetic field associated with coronal loops. Current models suggest that an MHD instability can trigger magnetic reconnection, which will accelerate particles and release energy into the plasma.

1.5.6 CME's

Coronal mass ejections, or CME's, were first observed by OSO-7 (Orbiting Solar Observatory) in 1973, and later by Skylab in 1974, and are now seen by SOHO (Solar Heliospheric Observatory). CME's are essentially large scale magnetic structures being expelled from the Sun. They are caused by MHD processes in closed magnetic field regions, such as active regions, prominences and coronal arcades. It has been suggested that the emergence of new flux near closed magnetic field regions is directly linked to the onset of CME's (Feynman and Martin, 1995; Wang and Sheeley, 1999). CME's have been detected along the entire Sun-Earth distance (Manoharan et al., 1995), and can influence the interplanetary medium.

The initiation of CME's is still a strong topic of debate. Some CME's are associated with flares, and some have no associated chromospheric activity. A large number of flares are associated with eruptive prominences, and the eruption of prominences is a strong candidate for the onset of CME's (Wu et al., 2000). Another view is that CME's result from an untwisting of magnetic field lines, such as the kink instability.

Typical ejection speeds are > 1000 km/s for energetic CME's, but as low as 10 km/s for CME's with no associated chromospheric activity, such as those seen near solar minimum. Typical mass ejected in a CME is 10^{13}kg, giving a kinetic energy of 10^{32} ergs, combining this with the magnetic energy gives a total energy comparable to or larger than the energy released in flares.

For flare-related CME's, it is not the flare that causes the onset of ejection, as CME's sometimes precede flares. However, flares, erupting prominences and CME's may all be caused by a loss of MHD equilibrium.

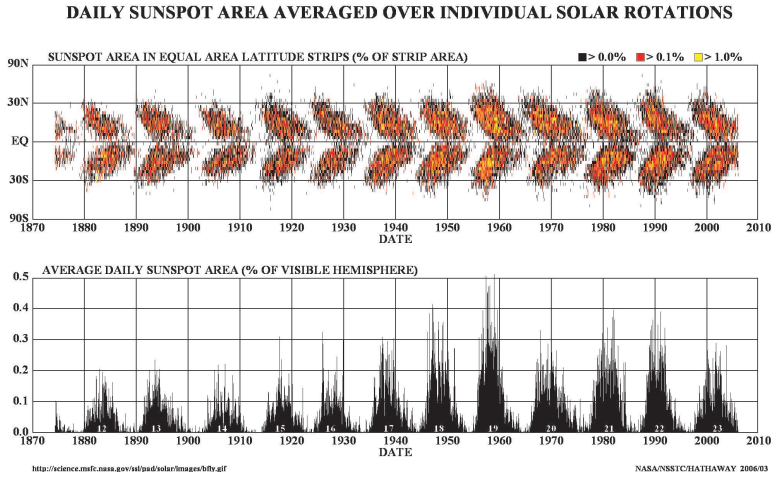

Figure 1.9: The 'Butterfly' diagram. Top panel shows latitude of emerging sunspots as a function of time. Bottom panel shows total averaged number of sunspots. Courtesy NASA.

1.5.7 The Solar Cycle

The activity on the solar surface and in the atmosphere above undergoes temporal variations on time scales much longer than the individual phenomena previously mentioned. This was first noticed in the number of sunspots appearing on the solar surface. The number of sunspots appears to wax and wane on an 11 year cycle, first discovered by Schwabel in 1844, and can be seen in figure 1.9.

Sunspots appear at latitudes below $\pm 35^o$. Another interesting feature of the sunspot cycle is that at the start of the cycle, new sunspot groups appear at $30^o - 35^o$ latitude, and towards the end of the cycle new groups appear at lower latitudes. This latitude migration can be seen in figure 1.9.

Sunspots usually occur as two bipoles of opposite polarity. The imaginary line connecting the two bipoles is always angled at to the equator, with the leading sunspot closest to the equator. This is known as *Joy's law*. The polarity of the leading sunspot is opposite for the northern and southern hemisphere. However, every 11 years, the polarity of a leading sunspot in a given hemisphere reverses (*Hale's law*). This 11 year switch coincides with the reversal of the Sun's general poloidal field, which can be measured

by summing up the small scale poloidal field on the surface.

It is not only sunspots that exhibit cyclic behaviour, EUV observations of the solar corona show that the number of active regions is larger at times of solar maximum than at solar minimum. At times of maximum more flares and CME's are observed. Furthermore the Sun's global field resembles a simple dipole structure at solar minimum, but is extremely complicated at solar maximum.

1.5.8 The Solar Dynamo

The fact that the magnetic field of the Sun, on both small and large scales, exhibits cyclic behaviour, with minima and maxima occurring regularly suggests that there is some kind of regeneration of magnetic field going on. Any 'fossil' field left over from the formation of the Sun must by now have dissipated away, as the time scale for magnetic diffusion for the whole Sun is much less than its age. This leads to the idea of a solar dynamo which regenerates magnetic field.

The idea of a dynamo in the context of MHD is based on the concept that motion of an electrically conducting fluid across magnetic field induces currents which generate more magnetic field. This regeneration acts against the continuous drain of energy due to the resistance of the fluid. Looking at the resistive induction equation (1.38), if the inductive process (represented by the advection term) outweighs the resistance to the currents (represented by the diffusive term), then magnetic field can be amplified by the velocity flows of the electrically conducting fluid.

An ideal investigation into the dynamo of the Sun would consist of large scale numerical simulations treating the entire Sun in the MHD approximation, However, this is difficult due to the vast range of scales and parameter regimes. It is more instructive to consider basic dynamo properties and then try to apply them to the Sun to see where they can operate.

The dynamo problem is often simplified by neglecting the feedback of the magnetic field on the flow (Lorentz force). By then specifying a velocity field, a small 'seed' field can be amplified if certain conditions are met. This is the well-known 'kinematic dynamo'. Problems lie even in this idealised set-up, however. Cowling, in 1934 derived

the 'anti-dynamo' theorem, which shows that a steady axi-symmetric magnetic field cannot be maintained by a dynamo. Other anti-dynamo theories followed shortly after, showing that other simple cases can be ruled out.

The solution for the kinematic dynamo came about by considering dynamo action in a different way by splitting the magnetic field into two components, poloidal (N-S) and toroidal (E-W). The kinematic dynamo can be made to work provided that a velocity field can be found which regenerates both the toroidal field and the poloidal field.

Thinking about the Sun, an obvious velocity flow to consider is the differential rotation observed at the surface and in the convection zone below. Differential rotation, if the plasma is highly conducting (High R_m), is able to 'stretch out' poloidal field into toroidal field. This is known as the ω-effect. Now all that is required is to find a reverse process, a way of converting toroidal field into poloidal field, and the cycle is complete.

This reverse process is much more complicated, and still under considerable debate today. In 1955, Eugene Parker suggested that small scale helical motions, which are present in convection in a rotating body such as the Sun, can twist toroidal field into loops of field in the meridional plane. The sum of these loops gives rise to a large-scale poloidal field, therefore completing the cycle. This process is known as the α-effect.

Having described the basic process of how a dynamo can operate, these now need to be related to the Sun, to determine where the solar dynamo can operate. As these processes involve convection and differential rotation, the convection zone appears to be an ideal choice. Models which distribute the solar dynamo over the whole convection zone have been successful in reproducing qualitative features of large scale field in the Sun (Stix, 1976). However, a dynamo which operates solely in the convection zone is incapable of producing the strong magnetic fields which are found within active regions. Parker (1979) showed that regions of concentrated magnetic field will buoyantly rise to the surface on time scales much shorter than the solar cycle period, and that it is doubtful that magnetic field can be held in the convection zone until it is concentrated to the observed field strengths.

Turbulent motions also inhibit dynamo actions, as they tend to expel magnetic field from regions of high concentration. However, because of this expelling these helical

motions are also capable of concentrating magnetic field beneath the convection zone in a convectively stable region (Spiegel and Weiss, 1980). This leads to a modified model for the dynamo, with the regeneration process occurring beneath the convection zone (Galloway and Weiss, 1981). Magnetic field will be less susceptible to buoyancy, and can be concentrated to stronger values. However, it will also be less amplified by the turbulent convection. This is called α-quenching.

It remains to see if large scale field can be generated at the base of the convection zone. The solution to this problem comes from helioseismology, which can infer the internal rotation of the Sun. The tachocline, a region of large radial shear, where the rotation of the Sun goes from differential to solid body rotation in a small shell, is of particular importance. It is the strongest site of velocity shear in the Sun, and thus an ideal candidate for the seat of the ω-effect. Parker (1993) came up with the *interface dynamo*. The two processes are spatially separated, with the α-effect occurring in the turbulent convective layer, and the ω-effect occurring in the shear layer below. This model circumnavigates the α quenching issue as it allows strong toroidal field to be generated away from the seat of the α-effect (Charbonneau and MacGregor, 1996).

The interface dynamo has since been developed further. Magnetic field can be driven up from the tachocline into the convection zone by an instability called the magnetic buoyancy instability (MBI). The MBI is a Rayleigh-Taylor like instability that occurs when magnetic field can hold up denser gas due to magnetic pressure. A mechanism is needed to return this flux to keep the interface dynamo efficient. The mechanism suggested is the downward expulsion of flux by turbulent convection (called *magnetic pumping*). Numerical simulations have tested this mechanism and shown it to be important for the interface model (Tobias et al., 2001).

This leads to the current solar dynamo model. Toroidal field is generated by shearing in the tachocline. This field is then susceptible to the magnetic buoyancy instability and rises into the convection zone, where poloidal field is generated by the α-effect. The convection zone acts as a filter. If the field is strong enough, it continues to rise though buoyancy to the surface, giving rise to the active regions observed. Weaker field is churned up by convection, and is returned to the tachocline by magnetic pumping.

The entire process is repeated, and gives rise to the observed solar cycle of magnetic phenomena on the surface.

It is important to know that this is far from the final answer. As yet full numerical simulations of a complete dynamo do not exist. Instead each process is being investigated separately (Ossendrijver, 2003). Also, many aspects of the α-effect are still under considerable debate. One of the main problems is that results from numerical simulations (Cattaneo and Hughes, 1996) show that α-quenching is more severe than once thought, this has lead to other mechanisms being suggested for the generation of poloidal field. Suggestions to date include the α effect operating at the surface, the Leighton-Babcock model (Babcock, 1961; Leighton, 1969), and even a tachocline based α-effect. For a full review see Bushby and Mason (2004). What is generally accepted is that the ω-effect is seated in the tachocline at the base of the convection zone, and that strong enough fields are unstable and rise to the surface to give the observed active regions and associated phenomena such as sunspots and coronal loops.

1.6 Magnetic Flux Emergence

It is now accepted that the active regions on the Sun are a result of the buoyant rise of magnetic flux from the convection zone. Parker (1955) was the first to suggest that sunspots could be formed from an underlying toroidal magnetic flux concentration, and as a result introduced the concept of magnetic buoyancy.

Imagine a magnetic flux tube in the convection zone. In equilibrium the total pressure must balance internally(i) and externally(e) so that

$$P_e = P_i + \frac{B^2}{2\mu_0} \tag{1.50}$$

which means that the tube has less gas pressure inside than outside $p_i < p_e$. Assuming that the flux tube is in thermal equilibrium with the surrounding plasma this means that $\rho_i < \rho_e$ and the tube is less dense than its surroundings and therefore buoyant.

The flux that rises to the surface and forms sunspots must also be the field that forms active regions. Dynamo actions can occur on the surface, but they are not strong enough to produce KG fields, so cannot produce the strong magnetic fields associated

with large scale active regions. Predictions from current dynamo models suggest that strong (10^5G) magnetic fields is capable of rising to the surface from the convection zone., and this is the magnetic field that forms these active regions.

This idea of flux rising to the surface and into the atmosphere is known as *flux emergence*, and is of considerable interest to both the study of the solar dynamo and the study of magnetic field in the solar atmosphere. It provides a way of coupling these two manifestations of the Sun's magnetic field, and can give insight into the structure and behaviour of various atmospheric phenomena.

Large scale field in the tachocline is unstable to the magnetic buoyancy instability, and can give rise to the formation of loops or flux tubes, which can rise up to the surface on time scales of months (Moreno-Insertis, 1986; D'Silva and Choudhuri, 1993; Caligari et al., 1995; Fan et al., 1994). As mentioned in the previous section (1.5.8), large fields can continue to rise, while small fields are 'pumped' back into the tachocline.

Magnetic flux tubes will tend to rise in the convection zone, because the initial magnetic buoyancy pushes plasma upwards, and due to the super-adiabatic nature of the convection zone (section 1.2.1), they continue to rise to the surface. During the rise, the roots of the flux tube remain close to the base of the convection zone, while the apex rises across the convection zone and eventually erupts at the photosphere (Zwann, 1978; van Ballegooijen, 1982; Moreno-Insertis, 1986).

Figure 1.10 shows a cartoon picture of flux emergence, along with its place in the current solar dynamo model. In this model a flux tube rises to the surface while its roots remain tied to the original layer at the base of the convection zone.

Since Parker (1955) suggested that sunspots could be formed from toroidal field at the base of the convection zone, there has been much interest in flux emergence. As in the majority of studies of fluid dynamics, numerical experiments must be performed, as the governing equations cannot be solved analytically. An ideal experiment would simulate the full evolution of a rising magnetic flux tube, which begins with unstable magnetic field at the base of the convection zone, and ends with the erupting flux forming new active regions at the surface. However, a simple look at the problem throws up some difficulties in this approach. The density stratification drops by 6 orders of magnitude

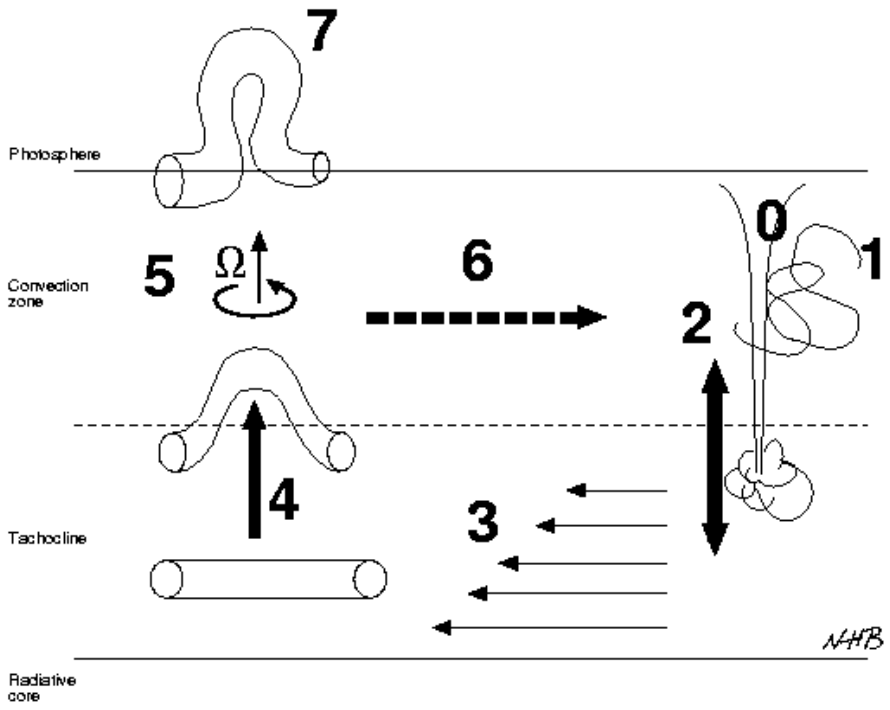

Figure 1.10: Schematic diagram showing the idea of flux emergence and its relation to the solar dynamo. (0) and (1) show the generation and destruction of small scale magnetic field in the convection zone. (2) and (3) show the transport of magnetic field from the tachocline into the convection zone and flux pumping in the reverse direction. (4) shows the formation of flux tubes from the toroidal field. (5) and (6) show the generation of poloidal field by helical turbulence. (7) shows the emergence of the flux tube into the atmosphere and the formation of an active region. Courtesy N H Brummel.

from the base of the convection zone to the surface, and the density drops off further in the atmosphere also. In addition the convection zone is turbulent in nature, and an ideal simulation must also be three dimensional. These factors make a full simulation almost impossible with today's computing power. In the past different approaches have been used to investigate flux emergence.

Some of the properties of rising flux tubes can be well expressed through one-dimensional models. For most of the evolution of a flux tube in the convection zone, its radius is much less than the local scale height. The *thin flux tube approximation* allows calculation of interesting properties of the rise of a flux tube in the convection zone. For more on properties that can be extracted from one-dimensional studies see Moreno-Insertis (1986); Choudhuri (1989); Moreno-Insertis (1992); D'Silva and Choudhuri (1993); Fan et al. (1993). One of the most useful results from these kinds of studies relates to the *tilt angle* of emerging active regions. The tilt angle is the angle between the equator and the line connecting the two poles of the bipolar structure. For rising flux tubes to give the correct tilt angle at the surface, the initial magnetic field concentration must be between 10^5 and 10^6 G (D'Silva and Choudhuri, 1993; Fan et al., 1994; Caligari et al., 1995; Fisher et al., 1995).

The thin flux tube approximation has been successful in explaining observed properties but fails near the top of the convection zone where the radius becomes comparable to the scale height. As a result two and three-dimensional studies become the best way to investigate flux emergence. This allows the inhomogeneity in the tube radius and along the tube axis to be included.

2D simulations by Schüβler (1979); Longcope and Fisher (1996) showed that a flux tube with only a longitudinal component of magnetic field will suffer significant deformation during its rise in the convection zone. The tube forms two vortex rolls and a following wake which engulfs a large fraction of the rising tube. This can be likened to a rising gas bubble that has no surface tension (Moreno-Insertis, 1997). A simple solution to this is to use an azimuthal component of magnetic field, and the stresses associated with this field can play the role of surface tension. The origin of this twist has been considered by Moreno-Insertis (1997), and is related to the formation of the

flux tube in the tachocline (Matthews et al., 1995). There are other effects which can prevent fragmentation, such as rotation, but twist is thought to be the most likely.

The effect of twist on the buoyant rise of flux tubes in the convection zone has been extensively studied (Moreno-Insertis and Emonet, 1996; Moreno-Insertis, 1997; Emonet and Moreno-Insertis, 1998; Wissink et al., 2000). Without sufficient twist, a flux tube will fragment and not survive the crossing of the convection zone. The twist of a flux tube can be defined in terms of the axial (B_A) and azimuthal (B_T) magnetic field.,

$$q = \frac{B_A}{rB_T} \tag{1.51}$$

where r is the radial distance from the centre of the tube.

A first order estimate of the minimum amount of twist q for a flux tube of radius a to have to survive the crossing of the convection zone is

$$|q_{min}| = \frac{1}{a}. \tag{1.52}$$

However, there is also an upper limit on the amount of twist a flux tube can have. Linton et al. (1996) investigated the kink instability of isolated twisted flux tubes. The tubes are stable provided that the twist is less than the critical value which depends inversely on square root of the tube radius. Tubes that are created in the lower convection zone with twist greater than this value will be destroyed by the kink instability during their rise. This gives a range of twist that flux tubes must have to be able to survive the crossing of the convection zone to the surface. However, a tube that is initially created with an amount of twist within this range can become unstable to the kink instability for two reasons. As the tube rises the drop in density in the convection zone cause significant expansion of the tube radius. Firstly this causes the critical value of twist for onset of the kink instability q_{cr} to decrease due to the increase in a (Linton et al., 1996). Secondly in order to conserve magnetic flux the average axial field decreases as the inverse of the radius squared while the azimuthal field decreases much less, typically with the inverse of the radius. This means that the amount of twist in the tube increases linearly with the radius. These two effects mean that as a flux tube rises to the surface it can become unstable to the kink instability. It is for this reason that the kink instability has been

suggested as a mechanism for the formation of δ sunspot groups (Linton et al., 1998; Matsumoto et al., 1998; Linton et al., 1999; Fan et al., 1999). These active regions are characterised by large tilt angles upon emergence, and subsequent rotation and development of large magnetic shear. If a stable tube can survive the convection zone and then become kink unstable it could be a mechanism for the formation of δ-spots.

Given that a sufficiently twisted flux tube will reach the surface by buoyancy, much work has been done to discover how the tube then expands into the atmosphere above. The photosphere is convectively stable, so that buoyancy cannot drive flux into the atmosphere. Magara (2001) showed that as the flux tube reaches the surface, its vertical motion stops and a significant amount of horizontal deformation occurs. It is this horizontal deformation which gives a possible emergence mechanism. A horizontal layer of magnetic field is capable of holding up denser gas (by total pressure balance) and therefore is unstable to a Rayleigh-Taylor like instability.

The emergence of magnetic field from the photosphere into the atmosphere above has been studied extensively in recent years (Matsumoto and Shibata, 1992; Matsumoto et al., 1993; Magara, 2001; Shibata et al., 1989; Shibata et al., 1989). These authors studied the emergence of magnetic field held at the photosphere by the convectively stable stratification. It was shown that these fields were unstable to mixed modes of the magnetic buoyancy instability. The resulting expansion of magnetic field was shown to match certain observational data of active regions. Nozawa et al. (1992); Matsumoto et al. (1993); Shibata et al. (1990) modified the analysis by looking at the effect of convection on the instability, showing how field held just beneath the photosphere could emerge into the atmosphere above.

More recent simulations have combined the buoyant and expansive phases of the emergence process, simulating rising magnetic flux tubes in the convection zone followed by the expansion through the photosphere into the corona via the magnetic buoyancy instability (Fan, 2001; Magara, 2001; Magara and Longcope, 2003; Manchester, 2001; Manchester et al., 2004). In these simulations an isolated twisted flux tube is inserted into the upper part of the convection zone which rises by magnetic buoyancy until it reaches the stable layers of the photosphere. The resulting, predominantly horizontal,

expansion leads to the formation of a magnetic layer which is unstable to the magnetic buoyancy instability and this drives magnetic field into the atmosphere above.

Archontis et al. (2004) and Galsgaard et al. (2005) showed how this emerging field would interact with a pre-existing coronal field, with the formation of current sheets and jets occurring as a by-product of reconnection. This reconnection with coronal field helps the flux tube to emerge through the lower atmosphere as field lines from beneath the surface are reconnected to coronal field lines.

All these numerical simulations use a standard model for the solar atmosphere. The model consists of an adiabatically stratified convection zone, isothermal photosphere/chromosphere, isothermal corona and a transition region between the two isothermal regions. Furthermore the simulations are performed under the MHD approximation. The MHD approach treats the plasma as fully ionised, so that the fluid momentum is carried with the ions. However, the first ionisation potential of Hydrogen corresponds to a temperature of 1.6×10^5K. Calculations of the temperature in the solar atmosphere (Vernazza et al., 1981) show that the temperature minimum in the lower chromosphere is well below this, about 4000 K. The plasma here is not fully ionised but weakly ionised. The fluid now contains neutral atoms as well as ions and electrons. This means that in these weakly ionised regions, the fully ionised approximation of MHD is not applicable.

The presence of neutrals in the plasma may have an important effect on the evolution of magnetic fields in the solar atmosphere. The collisions between ions and neutrals must now be considered in the governing equations. The evolution of magnetic field is affected by collisions, and the inclusion of neutrals may have an strong effect on this evolution.

All this means that the effect of partial ionisation on the evolution of magnetic field and therefore the plasma in the solar atmosphere could be very significant. Moreover the emergence of magnetic fields through the partially ionised regions of the solar atmosphere may well be very different to the fully ionised models used so far. This warrants a full investigation into the effects of partial ionisation on magnetic flux emergence.

This thesis aims to develop techniques to simulate the evolution of magnetic

fields in a partially ionised plasma using a single fluid approach akin to MHD. Simulations will be performed to see how partial ionisation effects flux emergence and what it means for the evolution of the magnetic field and the subsequent structures formed in the solar atmosphere.

1.7 Overview of the Thesis

This introduction has hopefully explained why the study of flux emergence is important in solar physics, and given a sufficient introduction to the approach of MHD simulations of flux emergence. The aim of this thesis is to develop numerical techniques and perform simulations which include the effect of partial ionisation in MHD studies of flux emergence, as to date all previous work assumes the solar atmosphere to be fully ionised. It is hoped that the results presented will show the importance of these effects, and show the consequences for the subject of flux emergence.

Chapter 2 contains a derivation of single fluid equations for a partially ionised plasma, analogous to the equations of MHD, for a plasma of arbitrary ionisation. Chapter 3 consists of calculations of the ionisation levels in the atmosphere of the Sun, and simplifications of the single fluid equations based on certain justified assumptions. Chapter 4 describes the numerical code used in these simulations, and how it has been adapted to include the effects of partial ionisation. Chapter 5 contains numerical investigations into the damping of Alfvén waves in the partially ionised plasma of the solar atmosphere. Chapter 6 and chapter 7 show results from 2D and 3D simulations of flux emergence in the partially ionised atmosphere of the Sun. This includes the simulation of buoyant flux tubes in the convection zone and the subsequent evolution in the atmosphere above. Chapter 8 summarises the main conclusions of this thesis. There follows an appendix which explains some numerical methods used in the solution of the governing equations.

Chapter 2

Partially Ionised Plasmas

2.1 Introduction

The equations of MHD describe the evolution of a completely ionised plasma in the fluid approximation. In this approximation the state variables such as velocity, density and energy density are averaged over the ions and the electrons. However, if the temperature is not high enough the kinetic energy of the constituent particles is small compared to the energy binding the outer electrons to the nucleus. In this situation collisions do not provide enough energy to strip an atom completely of its electron and as a result there will also be neutral atoms present as well as ions and electrons.

74% of the Sun's mass is accounted for by Hydrogen, and 25% by Helium. The remaining 1% is made up of heavier ions. The first ionisation potential of Hydrogen is 13.6 eV, which corresponds to a temperature of 1.6×10^5 K, and that for Helium is 24.6 eV or 2.9×10^5 K. The surface temperature of the Sun is about 5700 K, so that the temperature in this region is well below the ionisation temperature, and the plasma here is weakly ionised.

The ratio of neutral atoms to the total number of particles can be considered as a continuous function of temperature, varying from 1 when the temperature is at absolute zero, to close to 0 when the temperature is much larger than the temperature associated with ionisation of the atom. If the plasma is only partially ionised, the motion of the neutral atoms must be taken into account in the fluid description of the plasma.

Neutral atoms do not experience the Lorentz force, whereas ions and electrons moving in a magnetic field do. This causes a relative motion of charged and neutral species. This relative motion is sometimes called ion-neutral slip, or ion-neutral drift. This has implications for the momentum of the fluid as a whole. For a fully ionised plasma the heavy ions carry the momentum, as opposed to the electrons. In a partially ionised plasma the momentum is now shared between the ions and neutrals, which have similar masses.

In addition the added collisions of neutrals with electrons and ions must be considered. The evolution of currents in a plasma is determined by a competition between the driving electro-magnetic fields and the collisions between different components of the plasma. Collision rates between species affect the relationship between electric fields and currents. This relationship is called the generalised Ohm's law. Combining Ohm's law with Faraday's equation gives the evolution of the magnetic field (e.g the resistive induction equation (1.29)). The ion-neutral collisions may have a significant impact if the relative motion of ions and neutrals is large. This may be the case if the Lorentz force is large, because ions are affected by this force, whereas neutral atoms are not.

In this chapter, single fluid equations are derived for a partially ionised plasma, analogous to the MHD equations. The starting point is the multi fluid equations, i.e the fluid equations for each individual components of the plasma (ions, electrons and neutrals). These single fluid equations are obtained by taking different moments of the Boltzmann equation and integrating over velocity space.

These single fluid equations are used to derive governing equations for the plasma as a whole. These will be analogous to the MHD equations but with additional terms related to the conservation of mass, momentum and energy for the neutral components as well as the added collisions of electrons and ions with neutrals. The main difference to the MHD equations will be in the momentum equation and the generalised Ohm's law. These single fluid equations are combined with Maxwell's equation, the modified generalised Ohm's law and the equation of state to give the full set of equations needed to model a partially ionised plasma in the fluid approximation.

2.2 Single Fluid Equations Describing Partially Ionised Plasmas

2.2.1 The Continuity Equation

An incompletely ionised plasma is a three-component mixture containing ions (i), electrons (e) and neutral atoms (n). The motion of the three components of a partially ionised plasma can be specified by three velocities $\mathbf{v}_i$, $\mathbf{v}_e$ and $\mathbf{v}_n$. The plasma as a whole has a centre of mass velocity specified by

$$\mathbf{v} = \frac{1}{\rho}(m_i n_i \mathbf{v}_i + m_n n_n \mathbf{v}_n + m_e n_e \mathbf{v}_e) \tag{2.1}$$

where m_a and n_a are the mass and number density of each species ($a = i, e, n$). The density is defined by

$$\begin{aligned} \rho &= m_i n_i + m_n n_n + m_e n_e \qquad (2.2) \\ &= \rho_i + \rho_n + \rho_e. \end{aligned}$$

Treating each component as an individual fluid, the continuity equation for ions, electrons and neutrals can be used separately. However the three equations will couple via a source/drain term corresponding to ionisation and recombination.

$$\frac{\partial \rho_i}{\partial t} + \nabla.(\rho_i \mathbf{v}_i) = R_i \tag{2.3}$$

$$\frac{\partial \rho_n}{\partial t} + \nabla.(\rho_n \mathbf{v}_n) = R_n \tag{2.4}$$

$$\frac{\partial \rho_e}{\partial t} + \nabla.(\rho_e \mathbf{v}_e) = R_e \tag{2.5}$$

Where R_n is the rate of production (by recombination) of mass density of neutrals, R_i is the rate of production (by ionisation) of mass density of ions, and R_e is the source/drain term for electrons. Summing all three continuity equations gives

$$\frac{\partial(\rho_i + \rho_n + \rho_e)}{\partial t} + \nabla.(\rho_i \mathbf{v}_i + \rho_n \mathbf{v}_n + \rho_e \mathbf{v}_e) = 0 \tag{2.6}$$

$$\frac{\partial \rho}{\partial t} + \nabla.(\rho \mathbf{v}) = 0 \tag{2.7}$$

as the sum of the source/drain terms must cancel. This equation is the same as the continuity equation for a fully ionised plasma but the centre of mass velocity and total mass density are defined by equations (2.1) and (2.2).

As the electron mass is much smaller than the ion and neutral masses, the approximation

$$\rho = m_i n_i + m_n n_n \tag{2.8}$$

can be used and so the centre of mass velocity of the fluid can be approximated by

$$\mathbf{v} = \frac{1}{\rho}(m_i n_i \mathbf{v}_i + m_n n_n \mathbf{v}_n). \tag{2.9}$$

Defining the fractional density ξ_i of each species $a = i, e, n$ by

$$\xi_a = \frac{\rho_a}{\rho} = \frac{m_a n_a}{\sum_{j=i,e,n} m_j n_j} \tag{2.10}$$

the centre of mass velocity can be rewritten as

$$\mathbf{v} = \xi_i \mathbf{v}_i + \xi_n \mathbf{v}_n. \tag{2.11}$$

2.2.2 Equation of Motion

In order to derive the equation of motion for the entire plasma, each species (i,e,n) is treated as a single fluid, so the equation of motion for each is given by the single fluid equation.

$$\rho_a \frac{d_a}{dt}\mathbf{v}_a = -\nabla P_a + q_a n_a \left(\mathbf{E} + \mathbf{v}_a \wedge \mathbf{B}\right) + \sum_{b,b\neq a} \mathbf{R}_{ab} - \mathbf{S}_a. \tag{2.12}$$

The total derivative on the left hand side is the time derivative in a rest frame travelling with the species fluid velocity

$$\frac{d_a}{dt} = \frac{\partial}{\partial t} + \mathbf{v}_a.\nabla \tag{2.13}$$

The electric field and magnetic field are given by $\mathbf{E}$ and $\mathbf{B}$ respectively, and the second term on the right hand side is the Lorentz force, with the charge of species a being q_a. $\mathbf{R}_{ab}$ is the momentum change due to collisions of species a with species b. $\mathbf{S}_a$ is the source of momentum due to changes in ionisation.

This approach assumes isotropic pressure tensors and no viscosity. In general the pressure term in the absence of magnetic field is $\nabla.\mathbf{P}$ where $\mathbf{P}$ is the pressure tensor (Braginskii, 1965) and can be written as

$$\mathbf{P} = P\delta_{ij} - \Pi_{ij} \tag{2.14}$$

where P is the scalar pressure and Π_{ij} is the stress tensor, which has components

$$\Pi_{ij} = \nu(s_{ij} - \frac{1}{3}\delta_{ij}\nabla.\mathbf{v}) \tag{2.15}$$

and s_{ij} is the strain tensor and is given by

$$s_{ij} = \frac{1}{2}\left(\frac{\partial v_j}{\partial x_i} + \frac{\partial v_i}{\partial x_j}\right). \tag{2.16}$$

ν is the kinematic viscosity and δ_{ij} is the Kronicker-delta function. Including these terms in the momentum equation at this point is simple enough, but adds no more understanding to how partial ionisation affects the momentum equation. They are added to the single fluid momentum equation later in this chapter. $\mathbf{R}_{ab}$ is the average change in momentum of fluid a due to the collisions with fluid b. It derives from the first moment of the collision terms in the Boltzmann equation (1.26).

$$\mathbf{R}_{ab} = \int m\mathbf{v}C_{ab}. \tag{2.17}$$

Following the approach of Braginskii (1965), in the high collision frequency limit of MHD the species a and b can be assumed to have Maxwellian distributions. The collisional momentum change is therefore proportional to the relative velocity of the two species.

$$\mathbf{R}_{ab} = \alpha_{ab}(\mathbf{v}_b - \mathbf{v}_a) \tag{2.18}$$

where α_{ab} depends on the number density and mass of species a and b.

$$\alpha_{ab} = m_a n_a \nu'_{ab} \tag{2.19}$$

As in Cowling (1957), the factor α_{ab} is expressed in terms of the *effective collisional frequency* ν'_{ab}. This takes into account the reduce mass of the system and is related to the collisional frequency between species a and b, ν_{ab} by

$$\nu'_{ab} = \frac{m_b}{m_a + m_b}\nu_{ab}. \tag{2.20}$$

By momentum conservation,

$$\mathbf{R}_{ab} = -\mathbf{R}_{ba}. \tag{2.21}$$

Using the definition of the collisional forces R_{ab} they can be explicitly written for the three-component partially ionised plasma consisting of ions, neutrals and electrons (i,n,e).

$$\begin{aligned}
\mathbf{R}_{en} &= \alpha_{en}(\mathbf{v}_n - \mathbf{v}_e) = m_e n_e \nu'_{en}(\mathbf{v}_n - \mathbf{v}_e) \\
\mathbf{R}_{ne} &= \alpha_{ne}(\mathbf{v}_e - \mathbf{v}_n) = m_n n_n \nu'_{ne}(\mathbf{v}_e - \mathbf{v}_n) \\
\mathbf{R}_{in} &= \alpha_{in}(\mathbf{v}_n - \mathbf{v}_i) = m_i n_i \nu'_{in}(\mathbf{v}_n - \mathbf{v}_i) \\
\mathbf{R}_{ni} &= \alpha_{ni}(\mathbf{v}_i - \mathbf{v}_n) = m_n n_n \nu'_{ni}(\mathbf{v}_i - \mathbf{v}_n) \\
\mathbf{R}_{ei} &= \alpha_{ei}(\mathbf{v}_i - \mathbf{v}_e) = m_e n_e \nu'_{ei}(\mathbf{v}_i - \mathbf{v}_e) \\
\mathbf{R}_{ie} &= \alpha_{ie}(\mathbf{v}_e - \mathbf{v}_i) = m_i n_i \nu'_{ie}(\mathbf{v}_e - \mathbf{v}_i)
\end{aligned} \tag{2.22}$$

The following expressions are for a pure Hydrogen plasma, so that the ions are merely protons and the neutrals are hydrogen atoms. Thus $m_i \approx m_n$ and

$$\xi_n \approx \frac{n_n}{n_i + n_n}. \tag{2.23}$$

For electrons the equation of motion is

$$n_e m_e \frac{d_e}{dt}\mathbf{v}_e = -\nabla P_e - en\left(\mathbf{E} + \mathbf{v}_e \wedge \mathbf{B}\right) + \mathbf{R}_{ei} + \mathbf{R}_{en} - S_e \tag{2.24}$$

$$\begin{aligned}
&= -\nabla P_e - en\left(\mathbf{E} + \mathbf{v}_e \wedge \mathbf{B}\right) \\
&\quad + \alpha_{ei}(\mathbf{v}_i - \mathbf{v}_e) + \alpha_{en}(\mathbf{v}_n - \mathbf{v}_e) - S_e.
\end{aligned} \tag{2.25}$$

The relative velocity of electrons and neutrals $(\mathbf{v}_n - \mathbf{v}_e)$ can be expressed in terms of the current density $\mathbf{j} = en(\mathbf{v}_i - \mathbf{v}_e)$ and the drift velocity of ions and neutrals $\mathbf{w} = \mathbf{v}_i - \mathbf{v}_n$.

$$\begin{aligned}
\mathbf{v}_n - \mathbf{v}_e &= (\mathbf{v}_i - \mathbf{v}_e) - (\mathbf{v}_i - \mathbf{v}_n) \\
&= \frac{\mathbf{j}}{en_e} - \mathbf{w}
\end{aligned} \tag{2.26}$$

Here the quasi neutral nature of plasmas has been used, $n_i = n_e = n$. Using relation (2.26), the equation of motion of electrons can be written in terms of $\mathbf{j}$ and $\mathbf{w}$.

$$-n_e m_e \frac{d_e}{dt}\mathbf{v}_e - \nabla P_e - en\left(\mathbf{E} + \mathbf{v_e} \wedge \mathbf{B}\right) = -\alpha_e \frac{\mathbf{j}}{en} + \alpha_{en}\mathbf{w} + S_e \tag{2.27}$$

where

$$\alpha_e = \alpha_{ei} + \alpha_{en} = m_e n_e(\nu'_{ei} + \nu'_{en}). \tag{2.28}$$

The equation of motion for ions is given by

$$nm_i\frac{d_i}{dt}\mathbf{v}_i = -\nabla P_i + en\left(\mathbf{E}+\mathbf{v}_i\wedge\mathbf{B}\right)+\mathbf{R}_{ie}+\mathbf{R}_{in}-S_i \tag{2.29}$$

or

$$-nm_i\frac{d_i}{dt}\mathbf{v}_i-\nabla P_i+en\left(\mathbf{E}+\mathbf{v}_i\wedge\mathbf{B}\right)=\alpha_{ei}\frac{\mathbf{j}}{en}+\alpha_{in}\mathbf{w}+S_i. \tag{2.30}$$

In the same vein the neutral equation of motions is given by

$$n_nm_n\frac{d_n}{dt}\mathbf{v}_n = -\nabla P_n+\mathbf{R}_{ne}+\mathbf{R}_{ni}-S_n \tag{2.31}$$

$$\tag{2.32}$$

or

$$-n_nm_n\frac{d_n}{dt}\mathbf{v}_n-\nabla P_n = \alpha_{en}\frac{\mathbf{j}}{en}-\alpha_n\mathbf{w}+S_n \tag{2.33}$$

with

$$\alpha_n=\alpha_{en}+\alpha_{in}=m_en_e\nu'_{en}+m_in_i\nu'_{in}. \tag{2.34}$$

This approach means that the collisional terms in the equations of motion of the three components can all be expressed in terms of the current density $\mathbf{j}$ and ion-neutral drift $\mathbf{w}$.

$$-n_em_e\frac{d_e}{dt}\mathbf{v}_e-\nabla P_e-en\left(\mathbf{E}+\mathbf{v}_e\wedge\mathbf{B}\right) = -\alpha_e\frac{\mathbf{j}}{en}+\alpha_{en}\mathbf{w}+S_e \tag{2.35}$$

$$-n_im_i\frac{d_i}{dt}\mathbf{v}_i-\nabla P_i+en\left(\mathbf{E}+\mathbf{v}_i\wedge\mathbf{B}\right) = \alpha_{ei}\frac{\mathbf{j}}{en}+\alpha_{in}\mathbf{w}+S_i \tag{2.36}$$

$$-n_nm_n\frac{d_n}{dt}\mathbf{v}_n-\nabla P_n = \alpha_{en}\frac{\mathbf{j}}{en}-\alpha_n\mathbf{w}+S_n \tag{2.37}$$

By relating these to the EM fields permeating the plasma, the set of equations can be closed.

From these equations of motion it is now possible to construct an equation of motion for the bulk plasma in terms of the centre of mass velocity $\mathbf{v}$. Using the continuity equations (2.3)-(2.5) allows the inertial terms in the momentum equations

to be converted into conservative form.

$$
\begin{aligned}
m_i n_i \frac{d_i}{dt}\mathbf{v}_i &= \frac{\partial}{\partial t}(\rho_i \mathbf{v}_i) + \nabla.(\rho_i \mathbf{v}_i \mathbf{v}_i) - S_i && (2.38)\\
m_n n_n \frac{d_n}{dt}\mathbf{v}_n &= \frac{\partial}{\partial t}(\rho_n \mathbf{v}_n) + \nabla.(\rho_n \mathbf{v}_n \mathbf{v}_n) - S_n && (2.39)\\
m_e n_e \frac{d_e}{dt}\mathbf{v}_e &= \frac{\partial}{\partial t}(\rho_e \mathbf{v}_e) + \nabla.(\rho_e \mathbf{v}_e \mathbf{v}_e) - S_e && (2.40)\\
& && (2.41)
\end{aligned}
$$

Adding together all three equations of motion for the components of the plasma, and noting that collision terms cancel, and that the electron inertial term is negligible, gives the equation of motion for the plasma centre of mass velocity.

$$\frac{\partial}{\partial t}(\rho_i \mathbf{v}_i + \rho_n \mathbf{v}_n) + \nabla.(\rho_i \mathbf{v}_i \mathbf{v}_i + \rho_n \mathbf{v}_n \mathbf{v}_n) = -\nabla(P_i + P_e + P_n) + \mathbf{j} \wedge \mathbf{B} \qquad (2.42)$$

Using the definition of the centre of mass velocity and defining the gas pressure as $P = P_i + P_n + P_e$ this becomes

$$\frac{\partial}{\partial t}(\rho \mathbf{v}) + \nabla.(\rho_i \mathbf{v}_i \mathbf{v}_i + \rho_n \mathbf{v}_n \mathbf{v}_n) = -\nabla P + \mathbf{j} \wedge \mathbf{B}. \qquad (2.43)$$

Using the relations

$$
\begin{aligned}
\mathbf{v}_i &= \mathbf{v} + \xi_n \mathbf{w} && (2.44)\\
\mathbf{v}_n &= \mathbf{v} - (1 - \xi_n)\mathbf{w} && (2.45)
\end{aligned}
$$

where $\xi_n = \rho_n / \rho$ is the neutral fraction, and ξ_i is the ion fraction and $\xi_i + \xi_n = 1$, the divergence term in equation (2.43) can rewritten as

$$
\begin{aligned}
\rho_i \mathbf{v}_i \mathbf{v}_i + \rho_n \mathbf{v}_n \mathbf{v}_n &= (\rho_i \mathbf{v}_i + \rho_n \mathbf{v}_n)\mathbf{v} && (2.46)\\
&\quad + \xi_n \rho_i \mathbf{v}_i \mathbf{w} - (1 - \xi_n)\rho_n \mathbf{v}_n \mathbf{w} && (2.47)\\
&= \rho \mathbf{v}\mathbf{v} + \rho \xi_n \xi_i \mathbf{v}_i \mathbf{w} - \rho \xi_n (1 - \xi_n)\mathbf{v}_n \mathbf{w} && (2.48)\\
&= \rho \mathbf{v}\mathbf{v} + \rho \xi_n (1 - \xi_n)\mathbf{w}\mathbf{w}. && (2.49)
\end{aligned}
$$

Hence the equation of motion for the centre of mass for a partially ionised plasma is

$$\frac{\partial}{\partial t}(\rho \mathbf{v}) + \nabla.(\rho \mathbf{v}\mathbf{v}) = -\nabla P + \mathbf{j} \wedge \mathbf{B} - \nabla.(\rho \xi_n (1 - \xi_n)\mathbf{w}\mathbf{w}). \qquad (2.50)$$

If the last term in this equation is zero then the equation of motion is identical to that for a fully ionised plasma. Indeed, if ξ_n becomes zero, representing a neutral gas, or 1, representing a fully ionised plasma, the last term disappears. Then one is left with the familiar Euler's equation for a neutral gas, or the momentum equation for a fully ionised plasma (which contains the Lorentz force). If the ionisation level is neither zero or unity then this term can not necessarily be ignored.

2.2.3 The Energy Equation

Taking the second order moment of Boltzmann's equation for each species gives the equation for the temporal evolution of specific internal energy density. As in the derivation of the single fluid momentum equation, all viscous effects are left out for the sake of simplicity, but included in the final equations. Also, any effects due to thermal conduction have been ignored. Summing over the three species gives the single fluid energy equation.

$$\frac{\partial}{\partial t}(\rho\epsilon) + \nabla.(\rho\epsilon\mathbf{v}) \quad = \quad -P\nabla.\mathbf{v} + \mathbf{E}.(\mathbf{j} - nq\mathbf{v}) - (\mathbf{j} \wedge \mathbf{B}).\mathbf{v} \tag{2.51}$$

The last two terms of this equation can be written as

$$\mathbf{E}.(\mathbf{j} - nq\mathbf{v}) - (\mathbf{j} \wedge \mathbf{B}).\mathbf{v} = [\mathbf{E} + (\mathbf{v} \wedge \mathbf{B})].\mathbf{j} \tag{2.52}$$

Which is the scalar product of the electric field in the rest frame of the fluid ($\mathbf{E}' = \mathbf{E} + \mathbf{v} \wedge \mathbf{B}$) with the current density. This can be found using the generalised Ohm's law for a partially ionised plasma which will be derived in the next section. This term is called the Ohmic heating term. It represents the rate of energy dissipated from currents in the plasma due to collisions. The energy equation is thus

$$\frac{\partial}{\partial t}(\rho\epsilon) + \nabla.(\rho\epsilon\mathbf{v}) = -P\nabla.\mathbf{v} + [\mathbf{E} + (\mathbf{v} \wedge \mathbf{B})].\mathbf{j} \tag{2.53}$$

2.3 EM fields for a Partially Ionised Plasma

2.3.1 Ohm's Law

As mentioned in the previous section equations are needed to relate the current density and the ion-neutral drift velocity to the plasma variables. For a fully ionised plasma this

usually takes the form of relating the current density to the electric field by considering the motion of electrons. This will be the approach used here. The equation of motion for the electrons was given in equation (2.35).

$$-\nabla P_e - en\left(\mathbf{E} + \mathbf{v}_e \wedge \mathbf{B}\right) = -\alpha_e \frac{\mathbf{j}}{en} + \alpha_{en}\mathbf{w} \tag{2.54}$$

The first step is to rewrite the electron velocity in terms of the current density and ion-neutral drift velocity using the definition of the fractional densities.

$$\begin{aligned} \mathbf{v}_e &= \mathbf{v}_i - \frac{\mathbf{j}}{ne} \\ &= \mathbf{v} + \xi_n \mathbf{w} - \frac{\mathbf{j}}{ne} \end{aligned} \tag{2.55}$$

This gives

$$\begin{aligned} \mathbf{E} + \mathbf{v} \wedge \mathbf{B} &= -\frac{\nabla P_e}{en} + \frac{\alpha_e \mathbf{j}}{(en)^2} - \frac{\alpha_{en}\mathbf{w}}{en} \\ &\quad + \frac{\mathbf{j} \wedge \mathbf{B}}{en} - \xi_n \mathbf{w} \wedge \mathbf{B} \end{aligned} \tag{2.56}$$

This is similar to the Ohm's used in section 1.4.2 in that it relates the electric field as experienced by a particle in the rest frame of the fluid ($\mathbf{E} + \mathbf{v} \wedge \mathbf{B}$), to the current density. However, an equation for $\mathbf{w}$ is also needed. This equation can be found using the difference between the equations of motions for the charged components of the plasma and that for the neutrals (equations (2.36) + (2.35) and (2.37)). This difference is

$$\rho_i \rho_n \left[\frac{d_i}{dt}\mathbf{v}_i - \frac{d_n}{dt}\mathbf{v}_n\right] = -\rho_n \nabla(P_e + P_i) + \rho_i \nabla P_n + \rho_n \mathbf{j} \wedge \mathbf{B} \tag{2.57}$$

$$+\rho \frac{\alpha_{en}\mathbf{j}}{en} - \rho \alpha_n \mathbf{w} \tag{2.58}$$

which can be rearranged to give an equation for the ion-neutral drift velocity $\mathbf{w}$.

$$\mathbf{w} = -\frac{\mathbf{G}}{\alpha_n} + \xi_n \frac{\mathbf{j} \wedge \mathbf{B}}{\alpha_n} + \frac{\alpha_{en}}{\alpha_n}\frac{\mathbf{j}}{en} - \frac{\rho(1-\xi_n)\xi_n}{\alpha_n}\left[\frac{d_i}{dt}\mathbf{v}_i - \frac{d_n}{dt}\mathbf{v}_n\right] \tag{2.59}$$

where

$$\mathbf{G} = \xi_n \nabla(P_e + P_i) - \xi_i \nabla P_n. \tag{2.60}$$

This equation for $\mathbf{w}$ can be substituted into Ohm's law to relate $\mathbf{E}$ to $\mathbf{j}$. The last term on the right hand side of equation (2.59) can be neglected if terms of order $\frac{d\mathbf{w}}{dt}$ are

small compared with terms of order $\frac{\mathbf{w}}{\tau}$ in the collision terms. This is the same as saying that the time between collisions τ is small in comparison to a typical time scale dt over which plasma variables change, which is exactly the condition required for MHD to apply (Braginskii, 1965). This inertial term is therefore dropped from the equation for $\mathbf{w}$. It is trivial to see that this term is zero for either a fully ionised plasma or a completely neutral gas, as ξ_n is either 0 or 1.

Inserting the equation for $\mathbf{w}$ into equation (2.56) gives the generalised Ohm's law for a partially ionised plasma.

$$\mathbf{E} + (\mathbf{v} \wedge \mathbf{B}) = -\frac{1}{en}\left[\nabla P_e + \iota \mathbf{G}\right] - \frac{\xi_n}{\alpha_n}\mathbf{G} \wedge \mathbf{B} + (1 - 2\iota\xi_n)\frac{\mathbf{j} \wedge \mathbf{B}}{en} \quad (2.61)$$

$$+\frac{(\alpha_e - \iota\alpha_{en})}{(en)^2}\mathbf{j} - {\xi_n}^2\frac{(\mathbf{j} \wedge \mathbf{B}) \wedge \mathbf{B}}{\alpha_n} \quad (2.62)$$

with $\iota = \frac{\alpha_{en}}{\alpha_n}$.

Now that an equation for $\mathbf{w}$ has been derived, the additional divergence term in the equation of motion (2.50) due to the ion-neutral drift $\mathbf{w}$ can be estimated.

$$\frac{\partial}{\partial t}(\rho\mathbf{v}) + \nabla.(\rho\mathbf{v}\mathbf{v}) = -\nabla P + \mathbf{j} \wedge \mathbf{B} - \nabla.(\rho\xi_n(1 - \xi_n)\mathbf{w}\mathbf{w}). \quad (2.63)$$

As mentioned, if the plasma is entirely neutral or completely ionised the last term on the right hand side is zero. If it is partially ionised it needs to be evaluated. However, looking at the equation for $\mathbf{w}$ (2.59), it can be shown that

$$\begin{aligned} \mathbf{w} &\sim \frac{\mathbf{j} \wedge \mathbf{B}}{\alpha_n} \text{ for } \beta << 1 \\ &\sim \frac{\nabla P}{\alpha_n} \text{ for } \beta >> 1. \end{aligned}$$

Using the definition of α_n the condition for neglecting the divergence term compared to the other dominating terms in the momentum equation (2.50) becomes

$$\left(\frac{\tau_{in}}{\tau_A}\right)^2 << 1 \text{ for } \beta << 1 \quad (2.64)$$

$$\left(\frac{\tau_{in}}{\tau_{th}}\right)^2 << 1 \text{ for } \beta >> 1 \quad (2.65)$$

where τ_A is a typical Alfvén time scale and τ_{th} a thermal time scale. This condition means that if the timescale for collisions is much smaller than both the Alfvén time and

the thermal time (which is equal to the length scale over the sound speed) then the last term can be neglected from the equation of motion. This is indeed the case, as MHD assumes the plasma is collision dominated. As a result the extra divergence term in the equation of motion is left out of all subsequent studies.

2.3.2 Maxwell's Equations

These are of course unchanged from ideal MHD.

$$\nabla.\mathbf{B} = 0 \tag{2.66}$$

$$\nabla \wedge \mathbf{E} = -\frac{\partial \mathbf{B}}{\partial t} \tag{2.67}$$

$$\nabla \wedge \mathbf{B} = \mu_0 \mathbf{j} \tag{2.68}$$

Where the displacement current is neglected, as mentioned in chapter 1 (see equation (1.47)).

2.4 Equation of State

Generally speaking, an equation of state is a way of relating the macroscopic thermal properties of a state of matter. A typical example is the ideal gas law for a monatomic gaseous material, which relates gas pressure (P), number density (n), and temperature (T), $P = nk_BT$. In ideal MHD there is a simple relationship between temperature and specific internal energy density (ϵ), in fact they are proportional, so that only one equation of state is needed

$$P = \rho\epsilon(\gamma - 1) \tag{2.69}$$

where γ is the ratio of specific heats. However, for a partially ionised plasma there is a more complicated relationship between ϵ and T, due to the energy contained in ionisation.

For an expression of the gas pressure of a partially ionised plasma the ideal gas formula is used

$$P = n_T k_B T \tag{2.70}$$

where T is the temperature, k_B is Boltzmann's constant and n_T is the total number density of the plasma. For a partially ionised plasma

$$n_T = n_i + n_e + n_n. \tag{2.71}$$

The definition of pressure P can be rewritten using the definition of the neutral fraction

$$\xi_n = \frac{n_n}{n_i + n_n} \tag{2.72}$$

so that

$$P = n_T k_B T = \frac{\rho k_B T}{\mu_m} \tag{2.73}$$

where

$$\mu_m = \frac{m_i}{2 - \xi_n} \tag{2.74}$$

is the reduced mass. As can be seen, when the ionisation level is unity (a fully ionised plasma), the reduced mass is $m_i/2$ which is the expected value for a fully ionised hydrogen plasma. When the plasma tends towards fully neutral, the reduced mass is m_i.

The equation of state used here for a partially ionised hydrogen plasma is, as in the work of Vögler et al. (2005),

$$\epsilon = \frac{P}{\rho(\gamma - 1)} + \frac{n_i X_i}{\rho} \tag{2.75}$$

which can be expressed in terms of temperature using equations (2.73) and (2.72).

$$\epsilon = \frac{k_B T}{\mu_m(\gamma - 1)} + (1 - \xi_n)\frac{X_i}{m_i} \tag{2.76}$$

and X_i is the ionisation level of Hydrogen. This expression for the internal energy density ϵ, contains two separate terms, the ionisation term and the gas pressure term. Any mechanism which changes the internal energy of the plasma will not only affect the temperature of the plasma but also its ionisation level. Conversely, when the plasma temperature is increased, some of this temperature increase will also increase the ionisation level of the plasma, and some will raise the internal energy. This is different from a fully ionised plasma or a neutral gas, where changes in temperature and specific energy density are proportional.

The equations of MHD solve for the specific energy density, ϵ and the density, ρ. Hence any numerical scheme must then use equations (2.73) and (2.76) to calculate the gas pressure and temperature from these two variables. For a partially ionised plasma, equation (2.76) contains an ionisation term $(1-\xi_n)\frac{X_i}{m_i}$, which is a function of temperature. As a result, solving equation (2.76) for temperature T is an implicit equation. How this will be performed is shown in later sections which describe the numerical code used in these studies.

2.5 Summary

These, as derived in this chapter, are the equations governing a partially ionised plasma in the single fluid approach.

$$\frac{\partial}{\partial t}\rho + \nabla.(\rho\mathbf{v}) = 0 \tag{2.77}$$

$$\frac{\partial}{\partial t}(\rho\mathbf{v}) + \nabla.(\rho\mathbf{v}\mathbf{v}) = -\nabla P + \nabla.\Pi + \mathbf{j}\wedge\mathbf{B} \tag{2.78}$$

$$\frac{\partial}{\partial t}(\rho\epsilon) + \nabla.(\rho\epsilon\mathbf{v}) = -P\nabla.\mathbf{v} - \Pi_{ij}s_{ij} + \mathbf{E} + (\mathbf{v}\wedge\mathbf{B})\,.\mathbf{j} \tag{2.79}$$

$$\frac{\partial\mathbf{B}}{\partial t} = -\nabla\wedge\mathbf{E} \tag{2.80}$$

$$\begin{aligned}\mathbf{E} + (\mathbf{v}\wedge\mathbf{B}) = & -\frac{1}{en}\left[\nabla P_e - \iota\mathbf{G}\right] + \frac{\xi_n}{\alpha_n}\mathbf{G}\wedge\mathbf{B} \\ & +(1-2\iota\xi_n)\frac{\mathbf{j}\wedge\mathbf{B}}{en} + \frac{(\alpha_e - \iota\alpha_{en})}{(en)^2}\mathbf{j} \\ & -{\xi_n}^2\frac{(\mathbf{j}\wedge\mathbf{B})\wedge\mathbf{B}}{\alpha_n}\end{aligned} \tag{2.81}$$

where

$$\epsilon = \frac{k_B T}{\mu_m(\gamma-1)} + (1-\xi_n)\frac{X_i}{m_i} \tag{2.82}$$

and

$$P = \frac{\rho k_B T}{\mu_m} \tag{2.83}$$

The viscous terms have been added into the equation of motion (2.78) and the energy equation (2.79). The assumptions made were the same as for MHD (1.46). In the next chapter these equations will be applied to the partially ionised plasma of the solar atmosphere.

Chapter 3

The Partially Ionised Plasma of the Solar Atmosphere

3.1 Introduction

The large length scales associated with structures and dynamics in the solar atmosphere are typically much larger than the gyro-radius (a typical length scale is $10^5 - 10^6$ m whereas the gyro-radius in the corona is a metre for protons). This allows the use of the MHD approximation for the study of the plasma of the solar atmosphere.

MHD assumes the plasma to be completely ionised, i.e it is assumed only ions and electrons are present. The assumption that the plasma is fully ionised is justified in the corona as the extremely large temperatures, typically MK, mean that the electrons are completely stripped from their atoms.

Figure 3.1 shows the density and temperature profile with height for a model of the quiet Sun (Vernazza et al., 1981). The density and temperature were calculated by solving the non-LTE radiative transfer, statistical equilibrium and hydrostatic equilibrium equations. These are solved for heights of up to 2500km, which corresponds to the transition region. As can be seen in figure 3.1, the temperature reaches a minimum of 4000 K at approximately 500 km above the surface. The temperature at this height corresponds to an energy of 0.34 eV which is much less than the first ionisation potential of Hydrogen (13.6 eV). The plasma here is weakly ionised. In these regions it is clearly

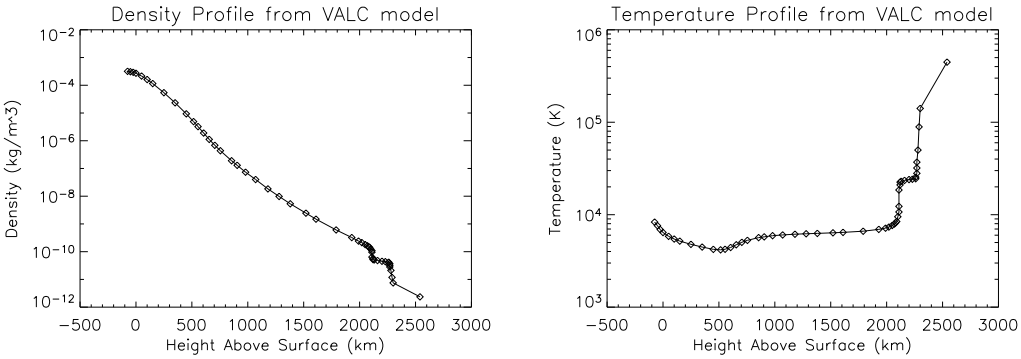

Figure 3.1: The density (left) and temperature (right) stratification taken from the VALC model of the quiet Sun (Vernazza et al., 1981).

not valid to assume that the plasma is fully ionised, and the single fluid approach must now include averages of fluid variables such as velocity and momentum over neutral atoms as well as electrons and ions.

In this chapter the full equations for a partially ionised plasma, as derived in the previous chapter, are simplified based on the conditions in the solar atmosphere. The ionisation levels as functions of temperature and density are calculated based on simple models of the Hydrogen atom. Once the ionisation levels are known, calculations of the momentum transfer during collisions between all three species can be calculated. With these calculations, the governing equations can then be solved numerically to model atmospheric processes, but with the effect of the presence of neutrals directly included.

3.2 Approximations to Ohm's Law for the Solar Atmosphere

The generalised Ohm's law for a partially ionised plasma derived in Chapter 2 is

$$\begin{aligned}\mathbf{E}+(\mathbf{v}\wedge\mathbf{B}) &= -\frac{1}{en}\left[\nabla P_e-\iota\mathbf{G}\right]+\frac{\xi_n}{\alpha_n}\mathbf{G}\wedge\mathbf{B}+(1-2\iota\xi_n)\frac{\mathbf{j}\wedge\mathbf{B}}{en} \\ &\quad +\frac{(\alpha_e-\iota\alpha_{en})}{(en)^2}\mathbf{j}-{\xi_n}^2\frac{(\mathbf{j}\wedge\mathbf{B})\wedge\mathbf{B}}{\alpha_n}.\end{aligned} \tag{3.1}$$

However, this can be simplified for the partially ionised plasma of the solar atmosphere by using a few justified assumptions.

The $\mathbf{j} \wedge \mathbf{B}$ term in equation (3.1) is called the Hall term. Comparing this to the fourth term on the right hand side of equation (3.1), it can be neglected if

$$\frac{|\mathbf{j} \wedge \mathbf{B}|/en}{|\alpha_e \mathbf{j}|/(en)^2} \approx \frac{B^2 en/\mu_0 L}{m_e n {\nu_{ie}}' B/\mu_0 L} << 1 \tag{3.2}$$

where ν'_{ie} is the effective frequency of electron ion collisions. Using the definition of the Larmour frequency ω_c, this condition can be rewritten as

$$\frac{\omega_c}{{\nu_{ie}}'} << 1 \tag{3.3}$$

This is equivalent to stating that the timescale of collisions is much less than a typical time for gyro-rotation of particles around the magnetic field. As the fluid approximation assumes that the plasma is dominated by collisions, then this condition is always upheld.

The term which contains ∇P_e in equation (3.1) is called the *battery term*. It is the electric field that tries to counteract the motion of electrons driven by the pressure tensor, and acts to keep the plasma electrically neutral. Again, comparing to the fourth term in equation (3.1) gives the condition to neglect it as

$$\frac{|\nabla P/en|}{|\alpha_e \mathbf{j}|/(en)^2} << 1 \tag{3.4}$$

which can be written, using $P_e = P_i = n_i m_i {v_{t,i}}^2$, as

$$\frac{{v_{t,i}}^2 en\mu_0}{{\nu_{ie}}' B} << 1 \tag{3.5}$$

which, using the definition of the electron plasma frequency ω_{pe}, the Larmour radius r_L, and the skin depth $\delta = c/\omega_{pi}$, as well as $c^2 = 1/mu_0\epsilon_0$ for the speed of light, can be written as

$$\frac{{r_L}^2}{\delta^2}\frac{\omega_c}{{\nu_{ie}}'} << 1 \tag{3.6}$$

it is not clear if this is true in this case. Although $\frac{\omega_c}{{\nu_{ie}}'} << 1$ as before, $\frac{{r_L}^2}{\delta^2} > 1$ as the skin depth is usually smaller than the Larmour radius. However, for simplicity, the battery term, as in resistive MHD is left out of Ohm's law when studying the solar atmosphere.

In a similar fashion the $\iota \mathbf{G}$ term in equation (3.1) can also be dropped, as $\mathbf{G} \sim \nabla P$, and $\iota << 1$, as

$$\iota = \frac{\alpha_{en}}{\alpha_n} \sim \frac{m_e}{m_{in}} << 1. \tag{3.7}$$

Returning to equation (3.1), neglecting the Hall term and battery terms, there are three terms left to evaluate in the generalised Ohm's law.

$$\mathbf{E} + (\mathbf{v} \wedge \mathbf{B}) = \frac{\xi_n}{\alpha_n}\mathbf{G} \wedge \mathbf{B} + \frac{(\alpha_e - \iota\alpha_{en})}{en^2}\mathbf{j} - {\xi_n}^2\frac{(\mathbf{j} \wedge \mathbf{B}) \wedge \mathbf{B}}{\alpha_n} \tag{3.8}$$

The two terms containing current density can be rewritten using the definition of the Coulomb resistivity (Spitzer, 1962)

$$\eta = \frac{(\alpha_e - \iota\alpha_{en})}{(en)^2} \tag{3.9}$$

and the Cowling resistivity (Cowling, 1957)

$$\eta_c = \eta + \frac{{\xi_n}^2|\mathbf{B}|^2}{\alpha_n}. \tag{3.10}$$

Using the relation

$$(\mathbf{j} \wedge \mathbf{B}) \wedge \mathbf{B} = -\mathbf{j}_\perp|\mathbf{B}|^2 \tag{3.11}$$

where $\mathbf{j}_\perp$ is the component of the current density perpendicular to the magnetic field this generalised Ohm's law becomes

$$\begin{aligned} \mathbf{E} + \mathbf{v} \wedge \mathbf{B} &= \eta\mathbf{j} + (\eta_c - \eta)\mathbf{j}_\perp + \frac{\xi_n}{\alpha_n}\mathbf{G} \wedge \mathbf{B} \\ &= \eta\mathbf{j}_\parallel + \eta_c\mathbf{j}_\perp + \frac{\xi_n}{\alpha_n}\mathbf{G} \wedge \mathbf{B} \end{aligned} \tag{3.12}$$

where $\mathbf{j}_\parallel$ is the component of $\mathbf{j}$ parallel to the magnetic field. The third term in equation (3.12) can be compared to the other two by recalling the definition of $\mathbf{G}$ in equation (2.60).

$$\mathbf{G} = \xi_n\nabla(P_e + P_i) - \xi_i\nabla P_n \tag{3.13}$$

Using the equations for the pressure of each species $P_a = \frac{\rho_a\xi_a k_B T_a}{m_i}$ for a=i,e,n, and assuming that $T_e = T_i = T_n$ (which is not always the case) and that $n_i = n_e$ (which is true for length scales longer than the Debye length), this can be rewritten as

$$\mathbf{G} = \xi_n(1 - \xi_n)\nabla\left(\frac{\rho k_B T}{m_i}\right). \tag{3.14}$$

This is zero for very weakly ionised or fully ionised plasmas ($\xi_n = 0, 1$). The sharp rise in temperatures in the transition region suggest that the plasma changes very quickly from

weakly ionised at the temperature minimum to fully ionised in the corona and $\mathbf{G} = 0$. It is also worth noting that G is negligible compared to the $\mathbf{j} \wedge \mathbf{B}$ if the plasma is cold ($\beta << 1$), which is the case in the low-β corona.

For the solar atmosphere, the generalised Ohm's law simplifies to

$$\mathbf{E} + \mathbf{v} \wedge \mathbf{B} = \eta \mathbf{j}_{\parallel} + \eta_c \mathbf{j}_{\perp}. \tag{3.15}$$

which contains an advection term $\mathbf{v} \wedge \mathbf{B}$ and an anisotropic dissipative term.

The relative importance of advection and dissipation in resistive MHD is related to the magnetic Reynolds number, which comes from comparing the terms in the resistive induction equation (1.29).

$$R_m = \frac{\mu_0 L v}{\eta} \tag{3.16}$$

At high magnetic Reynolds numbers, the evolution of the field is dominated by advection by the fluid, and at low magnetic Reynolds numbers, the evolution is dominated by dissipation. In order to evaluate R_m for the solar atmosphere, estimates for the Coulomb and Cowling resistivities are needed, and are performed later in this chapter.

In fully ionised MHD the dissipation of currents by collisions is isotropic, which leads to isotropic dissipation in the induction equation. This leads to a diffusive term for the magnetic field (see equation (1.38)). Now, for a partially ionised plasma, there is an anisotropy in the current dissipation, where the electron collisions dissipate currents parallel to the field (η), and ion-neutral collisions dissipate currents perpendicular to the field (η_c). This will have consequences for the evolution of the magnetic field in the solar atmosphere.

For a magnetised, cold, partially ionised plasma, the Joule heating term in the energy equation (2.51) is now

$$\begin{aligned} (\mathbf{E} + \mathbf{v} \wedge \mathbf{B}).\mathbf{j} &= (\eta \mathbf{j}_{\parallel} + \eta_c \mathbf{j}_{\perp}).\mathbf{j} \\ &= \eta {j_{\parallel}}^2 + \eta_c {j_{\perp}}^2. \end{aligned} \tag{3.17}$$

3.3 Governing Equations for the Solar Atmosphere

Adding the simplified Ohm's law (3.15) in to Faraday's equation and adding to the single fluid equations derived in chapter 2 gives the governing equation for the partially ionised plasma of the solar atmosphere, which have been converted here into Lagrangian form.

$$\frac{D\rho}{Dt} = -\rho\nabla.\mathbf{v} \tag{3.18}$$

$$\rho\frac{D\mathbf{v}}{Dt} = \mathbf{j}\wedge\mathbf{B} - \nabla P + \nabla.\mathbf{\Pi} = \rho\mathbf{g} \tag{3.19}$$

$$\frac{D\mathbf{B}}{Dt} = (\mathbf{B}.\nabla)\mathbf{v} - \mathbf{B}(\nabla.\mathbf{v}) - \nabla\wedge(\eta\mathbf{j}_{\parallel}) - \nabla\wedge(\eta_c\mathbf{j}_{\perp}) \tag{3.20}$$

$$\rho\frac{D\epsilon}{Dt} = -P\nabla.\mathbf{v} + \eta {j_{\parallel}}^2 + \eta {j_{\perp}}^2 + \Pi_{ij}S_{ij} + H \tag{3.21}$$

The acceleration due to gravity $\rho\mathbf{g}$ has been included in equation (3.19). These equations are very similar to the MHD equations (1.41)-(1.44). In fact the mass and momentum equations are the same. The energy equation has a different form for the Joule heating, as well as a term H representing all the extra heating effects in the solar atmosphere, such as radiative losses. The most significant difference is in the induction equation. The anisotropy in the Ohm's law used for the partially ionised solar atmosphere (3.15) gives an anisotropy in the dissipation of currents in the induction equation. When the plasma is fully ionised, the neutral fraction ξ_n is zero, and $\eta_c = \eta$ and the equations return to the resistive MHD equations.

In resistive MHD the isotropic dissipation of currents translates into a diffusive term for the magnetic field (1.38). However in a partially ionised plasma, no longer can the induction equation be cast as a diffusion equation for the magnetic field, due to the anisotropy in the dissipation of currents. The two resistivities, η and η_c represent electron collisions (with both ions and neutrals) and ion-neutral collisions, respectively. Whereas in MHD the dissipation term $\eta\mathbf{j}$ represented the dissipative effect of electron-ion collisions, the electron collisions now only affect the current parallel to the field, via $\eta\mathbf{j}_{\parallel}$. The ion-neutral collisions affect the current perpendicular to the field, via $\eta_c\mathbf{j}_{\perp}$. In other words the electron collisions dissipate parallel (or field-aligned) currents and ion-neutral collisions dissipate perpendicular (or cross-field) currents.

In order to simulate the partially ionised solar atmosphere, the values of η_c and

η need to be estimated as functions of space. To do this an estimate of the neutral fraction, ξ_n, as a function of space is needed. Using this and estimates of the collisional frequencies (ν_{in} etc.), η and η_c can then be estimated.

Having calculated the resistivities, the importance of these dissipative terms can be estimated relative to other effects. As mentioned in chapter 1, if the Reynolds number is large then dissipative terms are negligible in the induction equation. This has been the case in the majority of MHD studies of solar atmospheric dynamics (Magara, 2001; Archontis et al., 2004, 2005; Galsgaard et al., 2005). The dissipation of currents is assumed to be negligible compared to advection of the magnetic field. However, in a partially ionised plasma, the momentum transfer upon collisions between ions and neutrals may become important.

This may lead to the Cowling resistivity being much larger than the Coulomb resistivity. This would have two effects. Firstly the magnetic Reynolds number would decrease, and dissipation by ion-neutral collisions may become more important. Secondly, a large anisotropy would develop in the dissipation of currents. If $\eta_c >> \eta$ then the dissipation of current only perpendicular to the magnetic field is important. This will have repercussions for solar atmospheric dynamics. In the next section the ionisation levels in the solar atmosphere are estimated, as are the collision times for ions, neutrals and electrons, and hence the Coulomb and Cowling resistivities.

3.4 Estimating the Ionisation of the Solar Atmosphere

To estimate the ionisation level, a method is needed to calculate the ratio of ionised to neutral atoms as a function of the temperature of the plasma. For a plasma such as the solar atmosphere, this would involve solving the ionisation equilibrium equation for not only Hydrogen, but Helium and other heavier elements. This exercise is beyond the scope of this work. For simplicity, the ionisation level is estimated assuming the solar atmosphere is pure Hydrogen. A simple model for the Hydrogen atom is then used to estimate the ionisation level as a function of temperature.

3.4.1 The Saha Equation

In 1920 the Indian physicist Meghnad Saha derived an equation that gave the fraction of atoms in each excited state of a gas in thermal equilibrium at a given temperature and total mass density. When a gas is in thermal equilibrium a single value of temperature is enough to describe the thermodynamic state everywhere. So the velocity distribution for the particles is a Maxwellian with the value of this temperature, T, and the radiation field has the isotropic black-body profile given by the Kirchoff-Planck equation. It is obvious that this rarely happens throughout the whole gas, but it may be true in certain regions. In this case the region is said to be in local thermodynamic equilibrium (LTE). In this certain region a single temperature is enough to describe the local emission and absorption rates of radiation.

The Saha equation for a gas in LTE is

$$\frac{n^+ n_e}{n_n} = \left(\frac{2\pi m_e k_B T}{h^2}\right)^{3/2} 2\frac{U^+}{U_0} \exp\left[-\frac{X_i}{k_B T}\right] \tag{3.22}$$

where n_n is the number density of atoms, n_e the number density of electrons and n^+ the number density of singly ionised ions. $U^+ = 2$ is the degeneracy of singly ionised ions, and $U_0 = 1$ the degeneracy of the neutral atom. X_i is the first ionisation energy of Hydrogen 13.6 eV, k_B is Boltzmann's constant, m_e is the mass of an electron and h is Planck's constant. For pure Hydrogen, $n^+ = n_i = n_e$, and Saha's equation becomes

$$\frac{n_i^2}{n_n} = f(T) = \frac{(2\pi m_e k_B T)^{\frac{3}{2}}}{h^3} \exp\left[-\frac{X_i}{k_B T}\right] \tag{3.23}$$

From this the neutral fraction

$$\xi_n \approx \frac{n_n}{n_i + n_n} \tag{3.24}$$

can be found via

$$r = \frac{n_n}{n_i} = \frac{1}{2}\left(-1 + \sqrt{\left(1 + \frac{4\rho/m_i}{f(T)}\right)}\right) \tag{3.25}$$

and then

$$\xi_n = \frac{r}{1+r}. \tag{3.26}$$

3.4.2 Non-LTE

The Saha equation is valid for a gas in local thermodynamic equilibrium (LTE). A plasma is in LTE if the length scale over which the temperature changes is larger than the *thermalization length* L_T. The thermalization length is defined by the distance a particle or photon emitted by a collision or transition travels before it has undergone enough further collisions or absorption/emissions so that it no longer can be distinguished within the distribution. Examples of plasmas in non-LTE are solar flares, spicules, and the lower chromosphere of the Sun (Brown, 1979; Pottasch and Thomas, 1959; De Pontieu et al., 2001). In this case local distributions are affected by photons originating from larger distances than the temperature change scale, where these protons are described by a different temperature. The plasma is then said to be 'non-local' or in 'non-LTE'. Hence the equilibrium can no longer be described by a single temperature.

The modified Saha equation

As stated, the chromosphere cannot be characterised by one temperature alone. The radiation temperature and the thermodynamic temperature cannot be assumed to be the same. This is because the mean free path of the solar radiation becomes large above the photosphere and the radiation field is of photospheric temperatures. Thus the standard Saha equation (3.23) is no longer valid.

Calculation of ionisation degrees in a non-LTE situation requires solution of the radiative transfer and statistical equilibrium equations. This would be very time consuming in simulations, as it would need to be done at each time step. It happens that approximations to non-LTE effects on Hydrogen ionisation have been developed, and it is to these this work now turns.

Using a two-level model of the Hydrogen atom Brown (1979) calculated non-steady state and non-LTE effects on the ionisation equilibrium of Hydrogen in optical flares. The ionisation equation is described by spontaneous recombination to the second level and by photoionisation for the return route (Ambartsumyan, 1958). Using this model, the modified Saha equation can be derived (Brown, 1979). The steady state

solution to the ionisation equation is given by (Thomas and Athay (1961))

$$\frac{{n_i}^2}{n_n} = \frac{f(T)}{b(T)} \tag{3.27}$$

$$f(T) = \frac{(2\pi m_e k_B T)^{\frac{3}{2}}}{h^3} \exp(-\frac{X_i}{k_B T}) \tag{3.28}$$

$$b(T) = \frac{T}{wT_R} \exp\left[\frac{X_i}{4k_B T}(\frac{T}{T_R} - 1)\right] \tag{3.29}$$

where T_R is the temperature of the photospheric radiation field (the temperature at the surface) and $w = 0.5$ is its dilution factor (Brown, 1979).

Whether the Saha equation or the modified Saha equation is used to calculate ξ_n, both the density and temperature of the plasma are required as a function of space. The calculation presented here adopts a model atmosphere of the quiet Sun, as determined by Vernazza et al. (1981), hereafter referred to as the VALC model. This will show how the profiles of η and η_c look for the quiet Sun. Of course, dynamical simulations must calculate the local values depending on local plasma variables.

3.4.3 Ionisation Levels in the Quiet Sun

Using the density and temperature profiles taken from the VALC model of the quiet Sun (Vernazza et al., 1981), and the modified Saha equation (3.27)-(3.29), the profile of $\frac{n_i^2}{n_n}$ is calculated and shown in figure 3.2. The ratio of $\frac{n_n}{n_i}$ is then given by equation (3.25) and is also shown in figure 3.2. The neutral fraction $\xi_n = \frac{n_n}{n_n + n_i}$ is then calculated and is shown in figure 3.3.

3.5 Estimating Cowling and Coulomb Resistivities in the Solar Atmosphere

Having estimated the ionisation level using the VALC model density and temperature stratification, the resistivities can now be calculated. Recall that

$$\eta = \frac{(\alpha_e - \iota\alpha_{en})}{(en)^2} \tag{3.30}$$

and

$$\eta_c = \eta + \frac{{\xi_n}^2 |\mathbf{B}|^2}{\alpha_n} \tag{3.31}$$

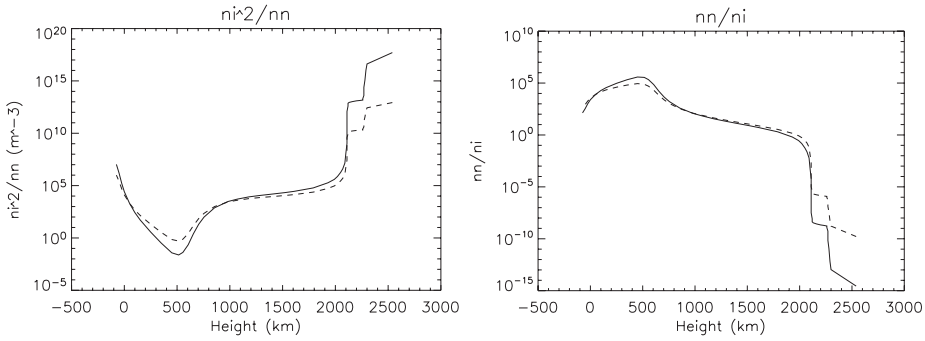

Figure 3.2: $\frac{n_i^2}{n_n}$ (left) and $\frac{n_n}{n_i}$ calculated using the density and temperature from the VALC model. The solid line is from the Saha equation, and the dashed line is from the modified Saha equation.

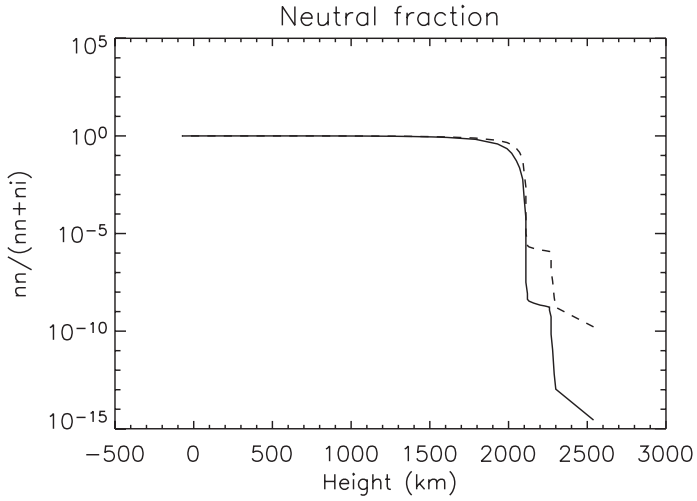

Figure 3.3: The neutral fraction $\xi_n = \frac{n_n}{n_n+n_i}$ calculated using the density and temperature from the VALC model. The solid line is from the Saha equation, and the dashed line is from the modified Saha equation.

where

$$\alpha_n = \alpha_{en} + \alpha_{in} = m_e n_e \nu'_{en} + m_i n_i \nu'_{in} \quad (3.32)$$

$$\alpha_e = \alpha_{ei} + \alpha_{en} = m_e n_e (\nu'_{ei} + \nu'_{en}). \quad (3.33)$$

$\iota = \alpha_{en}/\alpha_n$ and due to the ratio of electron mass and ion mass is very small. Hence

$$\eta \approx \frac{m_e n_e (\nu_{ei}' + \nu_{en}')}{e^2 n} \quad (3.34)$$

3.5.1 Collisional Frequencies

Following the example of Spitzer (1962), the neutral collisions are estimated by

$$\nu_{in} = n_n \sqrt{\frac{8K_B T}{\pi m_{in}}} \Sigma_{in} \quad (3.35)$$

$$\nu_{en} = n_n \sqrt{\frac{8K_B T}{\pi m_{en}}} \Sigma_{en}, \quad (3.36)$$

while

$$\nu_{ei} = 3.7.10^{-6} \frac{n_i \Lambda Z^2}{T^{3/2}}. \quad (3.37)$$

$\Sigma_{in} = 5.10^{-19}\mathrm{m}^2$ and $\Sigma_{en} = 10^{-19}\mathrm{m}^2$ are the ion-neutral and electron-neutral cross-sections respectively. Here Λ is the Coulomb logarithm (Spitzer, 1962).

3.5.2 Resistivities

Profiles of the Coulomb and Cowling resistivities can now be found as functions of height, for various magnetic field profiles using equations (3.31) and (3.34). This will enable a better understanding of the anisotropy in the dissipation of currents in the plasma. This is done for various magnetic field profiles, which are shown in figure 3.4. The profiles consist of both constant profiles of differing values and monotonically decreasing profiles. They are crude representations of the magnetic field in open field regions in the photosphere and chromosphere. The magnetic fields have a power law dependency on density so as to maintain magnetic flux within the tube.

As can be seen in figure 3.5, the Cowling resistivity is larger than the Coulomb resistivity in the chromosphere (heights of 2000 km) for various strengths of magnetic

Profile	Constant	Profile	$B_{ph}\left(\frac{\rho}{\rho_0}\right)^{\alpha}$
A	1000 G	D	$\alpha = 0.1$
B	100 G	E	$\alpha = 0.2$
C	10 G	F	$\alpha = 0.4$

Figure 3.4: A list of the magnetic field strength profiles used to calculate the resistivities. Profiles A-C are constant values. Profiles D-F have a power law dependence on density to maintain magnetic flux with height. $B_{ph} = 1200G$ and $\rho_{ph} = 2.7 \times 10^{-4} kg/m^3$

field. Even though the plasma is most neutral at lower heights, near the temperature minimum (see figure 3.2), the anisotropy in resistivity is most apparent at chromospheric heights. This is due to the inverse dependency of η_c on density (3.31), which falls rapidly off with height in the Sun's atmosphere.

The stronger the field, the larger the ratio of $\frac{\eta_c}{\eta}$, as is obvious from the definition of η_c. The magnetic field in the solar atmosphere is highly inhomogeneous. The actual value for the ratio η_c/η will depend on the local magnetic field used. Simulations performed in later chapters will show how this ratio develops for dynamic events in the solar atmosphere.

Now that typical values of the Coulomb and Cowling resistivity have been calculated, the relative importance of dissipation with respect to advection in the generalised Ohm's law (3.15) can be evaluated. Taking a typical value of η and η_c, the magnetic Reynolds number can be evaluated, assuming typical timescales and lengths scales in the atmosphere. The magnetic Reynolds number for a fully ionised plasma is usually defined as

$$R_m = \frac{\mu_0 L v}{\eta}. \tag{3.38}$$

and an equivalent number can be specified for partially ionised plasmas

$${R_m}^p = \frac{\mu_0 L v}{MAX(\eta, \eta_c)}. \tag{3.39}$$

Using a typical value from these calculations of $\eta = 1 \times 10^{-3}\,\Omega m$ at a height of 2000 km, this gives a value of $R_m = 1 \times 10^6$, so that when only considering electron collisions in a full ionised plasma, the advection term in Ohm's law dominates the dissipative term and the evolution of the magnetic field is dominated by advection. This is the reason that

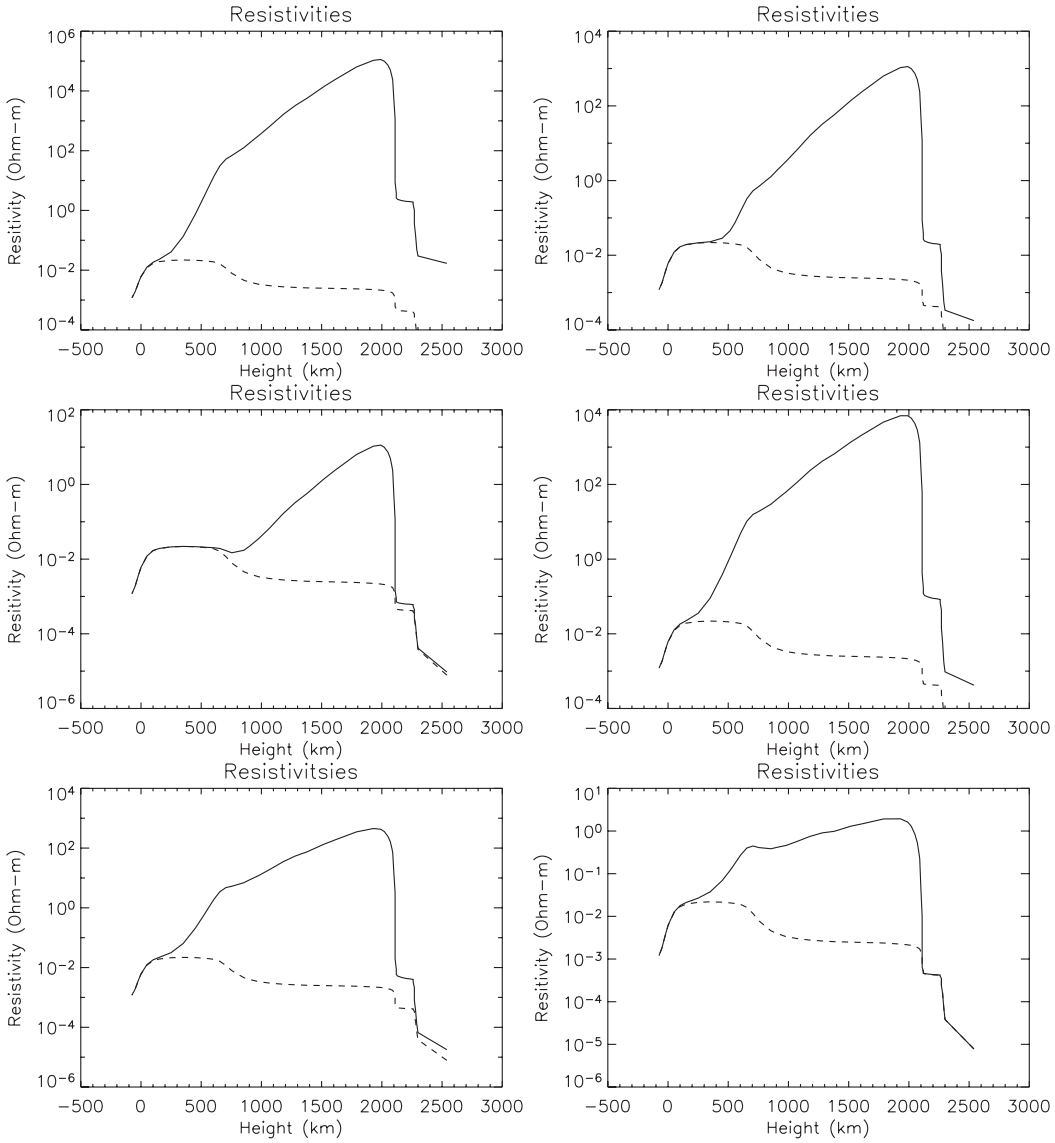

Figure 3.5: The Cowling (solid lines) and Coulomb (dashed lines) resistivities as functions of height for the different magnetic field profiles in figure 3.4. The top left panel is profile A, top right B, middle left C, middle right D, bottom left E, bottom right F.

the majority of numerical simulations of solar atmospheric dynamics use ideal MHD. However, for a partially ionised plasma the situation is different, using a typical value of $\eta_c = 1 \times 10^4\ \Omega m$, the new magnetic Reynolds number ${R_m}^p$ has a value of 0.05. Obviously these calculations are just estimates which depend on the magnetic field strength, but what they show is that it is possible for the Cowling resistivity to be stronger than the Coulomb resistivity. More importantly, they show that the new magnetic Reynold's number can be less than unity, so that the dissipative effect of ion-neutral collisions is a dominant effect on the evolution of the magnetic field. This manifests itself in a large anisotropy in the induction equation which favours the dissipation of cross-field currents rather than field-aligned currents.

As the evolution of the atmosphere is strongly influenced by magnetic field, this new anisotropy in the dissipative mechanisms due to the presence of neutrals in the plasma will have a strong effect on dynamic events in the solar atmosphere. In order to investigate these events, a numerical code is used to solve the governing equations for the partially ionised plasma of the Sun's atmosphere. The next chapter details the basic methods used in this code.

3.6 Heating Mechanisms in the Solar Atmosphere

The energy equation used thus far (equation (3.21)) has only included the adiabatic terms and the joule heating term. To simulate the solar atmosphere realistically the heat transfer effects that are present there must be included. The most obvious of these is radiative losses. The radiation given out from the surface interacts with the hot, sparse plasma of the atmosphere, and this in turn emits electromagnetic radiation.

As mentioned in chapter 1, one of the main problems in solar physics today is the problem of how the outer atmosphere of the Sun is heated. The temperature of the Sun falls with radius from the centre until it reaches the minimum in the photosphere, about 500 km above the surface. Then there is a sharp rise to several million K in a small region known as the transition region. The chromosphere and corona must be heated by some other mechanism or mechanisms.

The equation for the temporal evolution of the internal energy density should include all of these mechanisms

$$\rho\frac{D\epsilon}{Dt} = -P\nabla.\mathbf{v} + \eta {j_{\parallel}}^2 + \eta_c {j_{\perp}}^2 + \Pi_{ij}S_{ij} + S_h - \nabla.\mathbf{q} - L_R + M \tag{3.40}$$

The non-adiabatic terms on the right hand side include the Joule heating, as derived in chapter 3. The other non-adiabatic terms are viscous heating, shock heating, thermal conduction, radiative transfer and the mechanical heating terms. Thermal conduction is given by $\nabla.\mathbf{q}$, where $\mathbf{q} = \kappa\nabla T$ is the heat flux, and κ the thermal conductivity. S_h represents small scale shock dissipation S_h present in the chromosphere. This is caused by waves generated by convective motions at the top of the convection zone which propagate upwards, and due to the stratification, shock, dissipate and heat the local plasma (Narain and Ulmscneider, 1990). L_R represents all radiative losses. As well as these diagnosed heating effects there are many others associated with the coronal heating problem, which include reconnection, and the propagation and dissipation of MHD waves, all represented here by M.

In the next chapter the numerical methods used to solve the governing equations of a partially ionised plasma are presented.

Chapter 4

The Lagrangian-Remap code

4.1 Introduction

The Lagrangian Remap code (Arber et al., 2001), hereafter called *Lare* is a multidimensional code which solves the resistive MHD equations (1.27)-(1.30). The method is based on control averaging and a staggered grid. In a Lagrangian code the grid moves with the fluid, which allows higher resolution in areas of interest. However, for rotations or shocks this causes problems if the grid folds in on itself. A Lagrangian Remap code takes a Lagrangian step but then the variables are mapped conservatively back onto the original grid. The Lare code correctly handles shocks without the need for a Riemann solver, which can develop errors in low-beta simulations. The code itself is written in Fortran90 in a set of modules, and is parallelised using MPI to run on multiple processors. This allows domain decomposition and reduces run times. This chapter briefly explains the methods used in the code. The modifications to the code needed for solving equations describing a partially ionised plasma (3.18)-(3.21) are then presented.

4.2 The Lagrangian Remap code

4.2.1 Equations

The Lare code solves the resistive MHD equations, given here in Lagrangian form and with dimensionless variables.

$$\frac{D\rho}{Dt} = -\rho\nabla.\mathbf{v} \tag{4.1}$$

$$\frac{D\mathbf{v}}{Dt} = \frac{1}{\rho}\mathbf{j}\wedge\mathbf{B} - \frac{1}{\rho}\nabla P \tag{4.2}$$

$$\frac{D\mathbf{B}}{Dt} = (\mathbf{B}.\nabla)\mathbf{v} - \mathbf{B}(\nabla.\mathbf{v}) - \nabla\wedge(\eta\mathbf{j}) \tag{4.3}$$

$$\frac{D\epsilon}{Dt} = -\frac{P}{\rho}\nabla.\mathbf{v} + \frac{\eta}{\rho}j^2 \tag{4.4}$$

The equations (4.1)-(4.4) are made non-dimensional by writing each variable as

$$A = \hat{A}A^* \tag{4.5}$$

where $\hat{A}$ is the dimensionless variable and A^* is a typical value of the variable in the simulation. In the above set of equations the tildas have been dropped from the dimensionless variables.

In practice the continuity equation (4.1) is not used. Instead the density change is related directly to volume changes using mass conservation. Formally, if a plasma fluid element is at position $\mathbf{X} = (X_1, X_2, X_3)$ and moves to position $\mathbf{x} = (x_1, x_2, x_3)$, then $\mathbf{x}$ is a function of $\mathbf{X}$ and time. Hence the change in element length dx_i is

$$dx_i = \frac{\partial x_i}{\partial X_j}dX_j \tag{4.6}$$

with summation convention on j, and $i, j = 1, 2, 3$. This means the new density ρ is related to the old density ρ_0 by

$$\rho = \frac{\rho_0}{\triangle} \tag{4.7}$$

where $\triangle$ is the determinant of the transformation matrix which has elements

$$J_{i,j} = \frac{\partial x_i}{\partial X_j}. \tag{4.8}$$

In Lare $\triangle$ is evaluated by

$$\triangle = 1 + (\nabla.\mathbf{v})dt + O(dt^2). \tag{4.9}$$

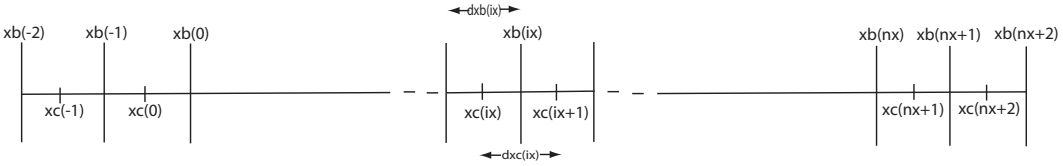

Figure 4.1: The computational domain in the x direction, showing cell boundaries (xb) and cell centres (xc).

which means that the Lagrangian step is second order. This approach of relating density changes to volume changes and using those volume changes elsewhere in the code guarantees exact conservation of mass.

As well as the Lagrangian equations (4.1)-(4.4), the code also needs to use the Lagrangian equations for the control volume averaged magnetic field and the flux through the cell face. These come from integrating equation (4.3) over the volume of a control volumed cell ($d\tau$) and the cell face surface ($\mathbf{dS}$) respectively.

$$\frac{D}{Dt}\int B_i d\tau = \int v_i \mathbf{B}.\mathbf{dS} - \int (\nabla \wedge (\eta \mathbf{j}))_i d\tau \tag{4.10}$$

$$\frac{D}{Dt}\int \mathbf{B}.\mathbf{dS} = -\int \eta \mathbf{j}.\mathbf{dl} \tag{4.11}$$

where $\mathbf{dl}$ is the line integral around surface $\mathbf{dS}$.

4.2.2 The Grid

The grid in the x direction is shown in figure 4.1. The variables are staggered on a computational cell as shown in figure 4.2. The scalars are defined at the centre of the cell, the velocities at the cell vertex. The magnetic field components are defined at cell faces. This allows the supplemental equation $\nabla.\mathbf{B} = 0$ to be maintained to machine precision using the Evans and Hawley constrained transport method (Evans and Hawley, 1988).

4.2.3 The Lagrangian Step

The Lagrangian step is second order in time and space, and is fully three dimensional. It is a simple predictor-corrector scheme and comprises two steps. Firstly the half time

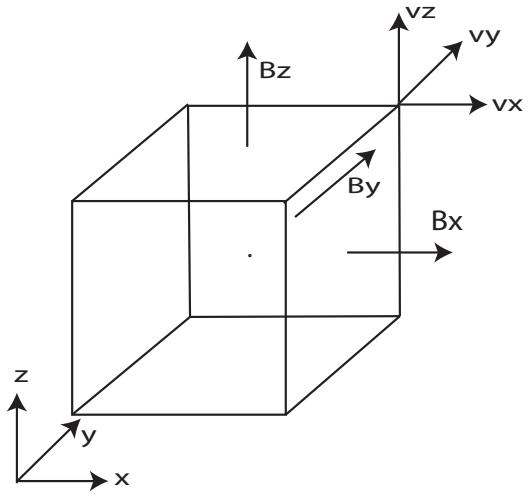

Figure 4.2: The staggered grid showing magnetic field and velocity components.

step pressure, energy density and magnetic field are found, and used to find the half time step vector force $\mathbf{F} = -\nabla P + \mathbf{j} \wedge \mathbf{B}$. Then the full time step density and energy density are calculated from the half time step vector force, along with the full time step velocities.

At the start of the step, all variables are defined at the same time. In the notation to follow a subscript * represents predictor ($\frac{1}{2}$ time step) values and a superscript ^{1} represents corrector (full step) values. At several points in the scheme, variables need to be calculated at different locations. Control volume averaging is used to calculate, for example, the density at the cell vertex, or the magnetic field at the vertex. One complication with at this stage is viscosity, and is dealt with in a later section.

Firstly, the thermal pressure is found from

$$P = \epsilon(\gamma - 1)\rho. \tag{4.12}$$

The predictor value of the internal specific energy density is

$$\epsilon^* = \epsilon - \frac{\delta t}{2}\frac{P\nabla.\mathbf{v}}{\rho} \tag{4.13}$$

The Jacobian of the predictor step is

$$\triangle^* = 1 + \frac{\delta t}{2}\nabla.\mathbf{v} + O(dt)^2 \tag{4.14}$$

and the half time step density and pressure can be found from

$$\rho^* = \frac{\rho}{\triangle^*} \tag{4.15}$$

$$P^* = \epsilon^*(\gamma - 1)\rho^* \tag{4.16}$$

To find the predictor value for the vector force $\mathbf{F}$, the magnetic field $\mathbf{B}$ must be updated so that the Lorentz force is time-centred. The core solver of Lare is ideal, i.e. $\eta = 0$. The predictor step $\mathbf{B}$ field is cell-volume centred. and follows from taking the ideal part of equation (4.10) and performing a finite difference scheme.

Having obtained the predictor pressure and magnetic field the predictor vector force $\mathbf{F}$ at the vertex can be calculated.

$$\mathbf{F}^* = \mathbf{j}^* \wedge \mathbf{B}^* - \nabla P^* \tag{4.17}$$

Control volume averaging is needed as $\mathbf{B}^*$ is defined at cell faces. The calculation of the half time step velocity completes the predictor step, (in the x direction)

$$v_x^* = v_x + \frac{\delta t}{2}\frac{{F_x}^*}{\rho^v} \tag{4.18}$$

The corrector step is straightforward as the $\mathbf{B}$ field does not need to be updated. The $\mathbf{B}$ field components are converted into fluxes. The core solver is for ideal MHD and so fluxes remain constant through the Lagrangian step (Alfvén's theorem). The corrector step is simply an update of the density control volume

$$\triangle^1 = 1 + \delta t \nabla . \mathbf{v}^* \tag{4.19}$$

followed by

$$\epsilon^1 = \epsilon - \delta t \frac{P^* {F_x}^*}{\rho} \tag{4.20}$$

$$\rho^1 = \frac{\rho}{\triangle^1} \tag{4.21}$$

$${v_x}^1 = v_x + \delta t \frac{{F_x}^*}{\rho^v} \tag{4.22}$$

with similar equations in x and y. All variables have been updated a full time step and are defined on the Lagrangian grid, and the next stage is to remap them back onto the original Eulerian grid to complete the entire process. This remap is a completely geometric process.

4.2.4 The Remap Step

The variables are mapped back onto the Eulerian grid in one-dimensional sweeps. This remap step is purely geometrical and is designed to maintain monotonicity. The process follows that of van Leer (1979), using Lagrangian variables to remap ρ and then mass co-ordinates to remap $\mathbf{v}$ and ϵ. The magnetic flux is remapped using a $\nabla.\mathbf{B}$ preserving scheme. For further details see Arber et al. (2001) and references therein.

4.2.5 Viscous Effects

So far no viscous effects have been mentioned. The viscosity is added during the predictor step. Recall that the viscous terms in the velocity and energy equation are

$$\frac{D\mathbf{v}}{Dt} = \frac{1}{\rho}\nabla.\Pi + ... \tag{4.23}$$

$$\frac{D\epsilon}{Dt} = \frac{1}{\rho}\Pi_{ij}S_{ij} + ... \tag{4.24}$$

respectively.

$$\Pi_{ij} = \nu(S_{ij} - \frac{1}{3}\delta_{ij}\nabla.\mathbf{v}) \tag{4.25}$$

and

$$S_{ij} = \frac{1}{2}\left(\frac{\partial v_j}{\partial x_j} + \frac{\partial v_i}{\partial x_j}\right) \tag{4.26}$$

are the stress and strain tensors. These terms are added in to the predictor step, and ν is calculated by

$$\nu = \nu_3 \rho c_f L \tag{4.27}$$

where c_f is the local fast speed, L is the smallest of the cell dimensions and ν_3 is a dimensionless number which is constant throughout the simulations.

In addition to the standard viscosity, Lare also include shock viscosities. Shock-capturing codes such as Lare are used when there is little diffusion present, such as viscosity, but the evolution of sharp gradients is needed. This cannot be done with finite difference codes, which develop Gibb's overshoot with sharp gradients. It is prudent, however to include artificial viscosities in shock-capturing codes to avoid generic numerical problems (Quirk, 1994). These artificial viscosities are applied only at shocks

and are zero in highly resolved smooth regions. The artificial viscosities in Lare follow Wilkins (1980) via the additional viscous pressure

$$q = \nu_1 \rho c_f L |\triangle v| + \nu_2 \rho L^2 \triangle v^2 \tag{4.28}$$

where $\triangle v$ is the difference in velocity across the cell in the direction of acceleration. This viscous pressure is simply added to the thermal pressure $P = \epsilon(\gamma - 1)\rho$ in the predictor and corrector update of ϵ (equations (4.13) and (4.20)). Practically, the two shock viscosities and the background viscosity are controlled by ν_1, ν_2, ν_3.

4.2.6 Resistive Effects

The core solver in Lare is ideal and includes no resistive effects. These effects are included as a separate routine within the main Lagrangian step. The integral of the resistive induction equation around the cell surface is given by equation (4.11) which can be written as an update of the magnetic flux through the cell face $\Phi = \int \mathbf{B}.\mathbf{dS}$.

$$\frac{D\Phi}{Dt} = -\int \eta \mathbf{j}.\mathbf{dl} \tag{4.29}$$

A first order time difference scheme is used for the update of the flux. In the x direction this would be

$$\frac{{\Phi_x}^{n+1} - {\Phi_x}^{n}}{dt} = -\int \eta \mathbf{j}.\mathbf{dl}. \tag{4.30}$$

The integral is performed around the cell face, using (in the update of of Φ_x) the lengths dyc and dzc and the resistivity η at each of the four vertexes. The criteria for stability of this scheme is given by

$$\Delta t < \Delta t_{res} = \frac{\Delta x^2}{\eta} \tag{4.31}$$

Ideally this scheme should be 2nd order and time centred, but this would involve half time step calculations of $\mathbf{j}$ and $\mathbf{dS}$ which is very difficult. This first order scheme is sufficient as resistive effects are diffusive.

Ohmic heating

The Ohmic heating term is given by

$$\frac{D\epsilon}{Dt} = ... + \frac{\eta}{\rho} j^2. \tag{4.32}$$

The current density $\mathbf{j} = \nabla \wedge \mathbf{B}$ and resistivity are defined at the cell vertex, whereas the internal specific energy density ϵ is defined at the cell centre. This means that the total Ohmic heating at each vertex is split eight ways and shared between the eight adjacent cell centres. This way each cell centre receives 8 contributions to its Ohmic heating from the 8 surrounding vertexes.

4.3 Adapting the Lare Code

4.3.1 The Resistive Step

In chapter 2 the governing equations for a partially ionised plasma in the single fluid equations were derived using the equations of motion for the ion, neutral and electron components, and Maxwell's equations for the EM fields, along with a generalised Ohm's law and equation of state. Then in chapter 3 the generalised Ohm's law for the solar plasma was simplified and the resulting equation for the magnetic field was shown to differ for that of standard MHD by an anisotropy in the dissipation of currents. This equation in Lagrangian form is

$$\frac{D\mathbf{B}}{Dt} = (\mathbf{B}.\nabla)\mathbf{v} - \mathbf{B}(\nabla.\mathbf{v}) - \nabla \wedge (\eta \mathbf{j}_{\|}) - \nabla \wedge (\eta_c j_{\perp}). \tag{4.33}$$

The resistive update of the magnetic flux (4.30) must be modified to include this anisotropy,

$$\frac{{\Phi_x}^{n+1} - {\Phi_x}^{n}}{dt} = -\int \eta \mathbf{j}_{\|}.\mathbf{dl} - \int \eta_c \mathbf{j}_{\perp}.\mathbf{dl} \tag{4.34}$$

where $\mathbf{j}_{\|}$ and $\mathbf{j}_{\perp}$ are calculated at the beginning of the Lagrangian step using the vector identities

$$\mathbf{j}_{\|} = \frac{(\mathbf{j}.\mathbf{B})\mathbf{B}}{|\mathbf{B}|^2} \tag{4.35}$$

$$\mathbf{j}_{\perp} = \frac{\mathbf{B} \wedge (\mathbf{j} \wedge \mathbf{B})}{|\mathbf{B}|^2}. \tag{4.36}$$

These are calculated on the numerical grid in the same way that the Lorentz force is in the velocity update. The criteria for the stability of this 1st order update now depends on the Cowling and Coulomb resistivities.

$$\Delta t < \Delta t_{res} = \frac{\Delta x^2}{MAX(\eta, \eta_c)} \tag{4.37}$$

However, as shown in chapter 3, the Cowling resistivity is dominant in the chromosphere ($\eta_c >> \eta$). As well as this, the timestep condition for the stability of the resistive update can be much less than the CFL condition for the Lagrangian update.

$$\frac{\Delta x^2}{MAX(\eta, \eta_c)} << \frac{\Delta x}{C} \tag{4.38}$$

Using typical values of the Cowling resistivity η_c taken from chapter 3 and typical speeds and grid spaces, a typical ratio of $\Delta t_{res}/\Delta t_{adv} = 0.1$

This means that the overall limitation on the timestep of the code is determined by the resistive condition, which will causes unnecessary slowing of the core solver of the code. The Lagrangian step does not need to be limited by this condition. To increase the efficiency of the code the resistive update is subcycled within the Lagrangian step. Firstly, the Lagrangian update is only subject to the CFL condition. Secondly, for every Lagrangian step, the resistive step is performed n times, where

$$n = INT\left(\frac{\Delta t_{adv}}{\Delta t_{res}}\right) + 1. \tag{4.39}$$

In this way if the advection condition is smaller than the resistive condition, there is no subcycling, and if the resistive condition is the smaller then the resistive update is subcycled within the main step. In this way both conditions are satisfied where needed. There is no guarantee that subcycling will be accurate using a 1st order resistive update within a 2nd order Lagrangian scheme. Simple numerical tests were performed to check whether subcycling introduced any errors. For a variety of problems, there were no stability issues, and the subcycling increased the speed of the code, close to the order of $\Delta t_{adv}/\Delta t_{res}$.

Ohmic heating

The Ohmic heating term is now

$$\frac{D\epsilon}{Dt} = ... + \frac{\eta}{\rho} {j_\parallel}^2 + \frac{\eta_c}{\rho} {j_\perp}^2. \tag{4.40}$$

where the parallel and perpendicular components of the current are found from equations (4.35) and (4.36). The heating is split between adjacent cell centres as in the fully ionised case.

4.3.2 The Equation of State

As shown in chapter 2 the equation for the internal specific energy density for a partially ionised plasma can be written

$$\epsilon = \frac{k_B T}{\mu_m(\gamma - 1)} + \frac{(1 - \xi_n)X_i}{m_i} \tag{4.41}$$

where ϵ is the specific energy density and T is the temperature. X_i is the ionisation of the ion and

$$\mu_m = \frac{m_i}{2 - \xi_n} \tag{4.42}$$

is the reduced mass.

The Lare code solves, among others, the time evolution of the specific internal energy density and mass density. The temperature can then be found from this equation of state

$$T = \frac{\epsilon(\gamma - 1)m_i}{k_B(2 - \xi_n)} - \frac{(1 - \xi_n)(\gamma - 1)X_i}{(2 - \xi_n)k_B} \tag{4.43}$$

However, the neutral fraction, which is calculated by the Saha or modified Saha equation, depends on temperature and density $\xi_n(\rho, T)$. So, provided the energy density and density are known, the equation for temperature is an implicit one.

$$T = F(T) \tag{4.44}$$

where

$$F(T) = \frac{\epsilon(\gamma - 1)m_i}{k_B(2 - \xi_n(T))} - \frac{(1 - \xi_n(T))(\gamma - 1)X_i}{(2 - \xi_n(T))k_B} \tag{4.45}$$

and the ionisation level ξ_n is given by the modified Saha equation. This implicit equation is solved at each time step using a simple bisection method to iteratively find the roots of the equation.

$$Y(T) = T - F(T) \tag{4.46}$$

The upper and lower limits of the bisection method are found from the previous calculation of the temperature, so that this method can be kept as fast as possible.

This calculation of the temperature at each step ensures the correct response of the plasma temperature to changes in energy. Once the temperature is found from ϵ,

the thermal pressure can be calculated. For fully ionised plasmas this was

$$P = \rho\epsilon(\gamma - 1) \tag{4.47}$$

but at all points in the code where the pressure is needed, such as the predictor update of ϵ, or the calculation of the vector force $\mathbf{F}$, must now be replaced by

$$P = \frac{\rho k_B T}{\mu_m} \tag{4.48}$$

where μ_m is the reduced mass and depends on the ionisation level, and therefore on the temperature.

4.4 Modeling Heating in the Lower Atmosphere

As already mentioned, the full evolution equation for the internal specific energy density must include all the heating and cooling effects present in the solar atmosphere. All these heating effects give the observed temperatures in the solar atmosphere. Thus a complete numerical study must include them to accurately simulate the emergence of magnetic flux from the convection zone through the photosphere, chromosphere and into the corona. However, simulating these effects directly is extremely problematic. Small scale effects are difficult to include in large scale MHD simulations. Although effects such as thermal conductivity could be added to the governing equations, the undiagnosed effects such as those associated with coronal heating, which are not known explicitly, would be almost impossible to simulate directly.

For this reason a simplified approach to modeling these effects is suggested, following the work of Abbet and Fisher (2003). The non-adiabatic heating and cooling terms mentioned above act to force the temperature profile of the Sun to that which is observed. Rather than include the terms individually it would be simpler to model their effects, namely that of forcing the temperature to the observed profile, by applying a forcing or relaxation term to the temperature profile. When the local temperature of the plasma deviates form the pre-defined value, it is forced back to this value, on a time-scale which reflects the different mechanisms of heating/cooling present locally.

This can be done by a simple Newton-cooling equation, which given in terms of the specific energy density, ϵ, is

$$\frac{d\epsilon}{dt} = -\frac{\epsilon - \epsilon_0(\rho(t=0))}{\tau} \tag{4.49}$$

where τ is the time-scale of the relaxation. The equilibrium specific energy density ϵ_0 is chosen to be a function of the density ρ.

A form for the time-scale of this relaxation is required. For this the approach of Gudiksen and Nordlund (2005) is adopted. In simulating coronal heating they chose τ to depend on some power of the density

$$\tau = \left(\frac{\rho}{\rho_{ph}}\right)^{-1.7} \tag{4.50}$$

so that at the relatively dense photosphere ($\rho = \rho_{ph}$) the time-scale is about 0.1s and is large enough that the effect becomes negligible in the sparse corona.

Now the equation for the evolution of the specific internal energy density is

$$\frac{D\epsilon}{Dt} = -\frac{P}{\rho}\nabla.\mathbf{v} + \frac{\eta}{\rho}{j_\parallel}^2 + \frac{\eta_c}{\rho}{j_\perp}^2 + \frac{1}{\rho}\Pi_{ij}s_{ij} - \frac{\epsilon - \epsilon_0(\rho(t=0)}{\tau} \tag{4.51}$$

A numerical method is needed to implement the Newton-cooling term in the code. A first order implicit finite difference scheme on equation (4.49) is used here,

$$\frac{\epsilon^{n+1} - \epsilon^n}{dt} = -\frac{\left(\epsilon^{n+1} - \epsilon_0(\rho)\right)}{\tau} \tag{4.52}$$

where the superscript represent the discrete time sequence. The update of ϵ due to this Newton-cooling term is given by

$$\epsilon^{n+1} = \frac{\epsilon^n + \frac{dt}{\tau}\epsilon_0(\rho)}{1 + \frac{dt}{\tau}}. \tag{4.53}$$

The reason for choosing this scheme becomes obvious when considering the stability. Applying the standard Von-Neumann stability analysis shows that the multiplication factor is

$$g = \frac{1}{1 + \frac{dt}{\tau}} < 1 \tag{4.54}$$

and the scheme is therefore unconditionally stable. The update of ϵ due to this extra term is performed at the end of each Lagrangian step. Whether it is performed at the start or the end has no effect on the solution.

In the next three chapters simulations of events in the solar atmosphere using the adapted Lare code are presented. The next chapter details studies of the evolution of waves in the partially ionised chromosphere. The two following chapters present methods and results from simulations of the emergence of magnetic flux through the partially ionised regions of the solar atmosphere.

Chapter 5

Collisional Damping of Alfvén Waves

5.1 Introduction

The inclusion of neutral species in the MHD treatment of plasmas has modified the collisional dissipation mechanism. As already stated this dissipation mechanism is caused by the relative velocities of ions and neutrals, which is large in regions of strong magnetic fields as neutrals are not driven by the Lorentz force. This relative velocity causes momentum transfer upon collisions between ions and neutrals and hence increased dissipation of energy into the plasma.

This dissipation mechanism manifests itself in the anisotropic dissipation of currents. As was shown in section 3.5, in the Sun this leads to preferential dissipation of currents perpendicular to the magnetic field, and is most prominent in the quiet chromospheric plasma, but is also dependent on the local magnetic field strength.

This dissipation mechanism also provides a mechanism for the damping of oscillations in the solar atmosphere. Any dissipation mechanism can convert energy of oscillations into energy in the medium in which the oscillations are present.

The magnetically dominated corona is an elastic and compressible medium which can support various types of waves. For waves with wavelengths above the Larmour radius and periods longer than the gyroperiod, these waves can be described by MHD.

These MHD waves perturb the macroscopic variables of the plasma such as density and pressure. Observations of oscillations of these variables have been observed with wavelengths comparable to characteristic sizes of coronal loops, plumes, active regions etc, and with periods from a few seconds to a few minutes.

The study of MHD waves is an important field in solar physics. Some of the unanswered questions such as the mechanisms for coronal heating, and flares, require detailed knowledge of the plasma parameters. These parameters cannot yet be directly measured to the required degree of accuracy. In particular the local magnetic field cannot be obtained accurately enough by Zeeman spitting or gyroresonant emission, or by less direct methods such as extrapolation from photospheric/chromospheric sources. Other parameters such as viscosity, resistivity, and thermal conduction cannot be determined accurately enough from observational data.

The detection of coronal waves provides a tool for determining these parameters, *coronal seismology*. Using a combination of theoretical modeling and observed properties of waves such as periods, damping rates and wavelengths, estimates of magnetic field strength and plasma transport coefficients can be made to a higher degree of accuracy. For a thorough review of the theoretical treatment of MHD waves see Roberts (2000, 2002); Goossens et al. (2002); Roberts and Nakaraiakov (2003); Roberts (2004).

5.1.1 Theory of MHD Waves

Plasmas can support coherent phenomena such as waves. In the low-frequency, large length-scale approximation of MHD, waves are driven by the Lorentz force and the pressure force.

By linearising the equations of MHD about a static equilibrium, and deriving dispersion relations, the wavemodes of MHD can be found. In the absence of magnetic field, the plasma pressure and compressibility generate sound waves. When the magnetic field is non-zero, the Lorentz force plays a part in the generation of MHD waves. The wavemodes of MHD are more complicated in nature than the acoustic modes of fluid dynamics, due to an induced anisotropy caused by the equilibrium magnetic field direction. Neglecting the effect of gravity, there are three types of MHD waves. The

three types of waves are called *Alfvén*, *slow magneto-acoustic* and *fast magneto-acoustic* waves.

Linear Alfvén waves displace magnetic field and velocity, but not plasma pressure or density. Moreover the displacement is incompressible and perpendicular to the magnetic field and the direction of propagation $\mathbf{k}$. They are a purely magnetic wave driven solely by magnetic tension. If $\mathbf{k}_{\|}$ is the component of the wave vector parallel to the magnetic field, and θ is the angle between the wave vector and the equilibrium magnetic field $\mathbf{B_0}$, then the dispersion relation for Alfvén waves is given by

$$\omega^2 = \frac{(\mathbf{k}.\mathbf{B}_0)^2}{\mu_0 \rho_0} = \frac{{k_{\|}}^2 {B_0}^2}{\mu_0 \rho_0} = k_{\|}^2 {v_A}^2 = k^2 {v_A}^2 cos^2\theta \tag{5.1}$$

Here $v_A = \frac{{B_0}^2}{\mu_0 \rho_0}$ is the Alfvén velocity, and a 0 in the subscript represents equilibrium values. Alfvén waves are highly anisotropic. As can be seen from equation (5.1), the frequency depends only on the component of the wave vector parallel to the equilibrium magnetic field $k_{\|}$. So although the wave vector can have components perpendicular to the magnetic field, the group velocity is always directed along the field. This means that Alfvén waves transport energy along the magnetic field and in no other direction.

The other two wavemodes, slow and fast magneto-acoustic waves, are solutions of the dispersion relation

$$\left(\omega^2 - k^2 {v_A}^2 cos^2\theta\right)\left(\omega^2 - {C_s}^2 k^2\right) - k^2 \omega^2 {v_A}^2 sin^2\theta = 0. \tag{5.2}$$

The slow magneto-acoustic wave is a longitudinal wave, and is characterised, to first order, by oscillations in the perturbed magnetic field parallel to the equilibrium field, as well as density and plasma pressure. In low-β plasmas, the slow mode is essentially an acoustic mode modified by the presence of the magnetic field. The group speed for the slow mode is finite for only small θ and so energy is transported in a narrow cone centred about the direction of the equilibrium magnetic field. The fast magneto-acoustic wave is also longitudinal, but characterised by oscillations in the perturbed magnetic field perpendicular to the equilibrium field, as well as density and plasma pressure. Moreover, the group speed is finite for all values of θ and therefore can transport energy in any direction.

5.1.2 Waves in the solar atmosphere

There is now a wealth of evidence of oscillations and waves in the atmosphere of the Sun. With the launch of the SOHO and TRACE satellites, detailed observations have been obtainable. In particular observations of EIT waves/coronal Moreton waves (Thompson et al., 1998), compressible waves in solar plumes (Ofman et al., 1997; Deforest and Gurman, 1998; Ofman et al., 1999) and in coronal loops (Berghmans and Clette, 1999; De Moortel, 2000; Robbrecht et al., 2001). Also flare-generated global kink oscillations of coronal loops (Aschwanden et al., 1999, 2002; Nakariakov et al., 1999; Schrijver et al., 2002) and longitudinal standing waves in loops (Kliem et al., 2002; Wang et al., 2002) have been observed. This large diversity in wave phenomena in the Sun can be explained by different modes of MHD waves. For a thorough review see Nakariakov et al. (2003); Aschwanden (2003, 2004) and references therein.

Alfvénic disturbances have been observed in the solar wind by various spacecraft, as close as 0.3 AU from the Sun and it is accepted that solar wind disturbances are of solar origin. Direct observations of Alfvénic oscillations closer to the Sun have proven difficult to find. However, magnetic field oscillations in the 5 minute period band have been interpreted as outgoing Alfvén waves (Ulrich, 1996). Waves of frequencies up to 0.1 Hz have been detected in the upper chromosphere and transition region (DeForest, 2004). These waves were visible in the TRACE 1600 Angstroms passband. The exact source of these waves is uncertain and they are not energetically significant to the chromosphere. Higher frequency waves (> 0.1 Hz) in the lower chromosphere have proved harder to find (Fossum and Carlsson, 2005). It has been suggested that high frequency Alfvén waves in the range 1 to 800 Hz can be created by small scale reconnection in the chromospheric network, and their dissipation was considered as a possible heating mechanism for the corona above (Marsch and Tu, 1997).

The convection zone, like any turbulent flow, generates acoustic waves of a wide range of frequencies which propagate in all directions, and as mentioned in Chapter 3, the subsequent shocking of these waves in the strong density stratification of the atmosphere above causes heating of the solar plasma. The continuing evolving convection below the photosphere is also a possible source for a wide range of MHD fluctuations, including

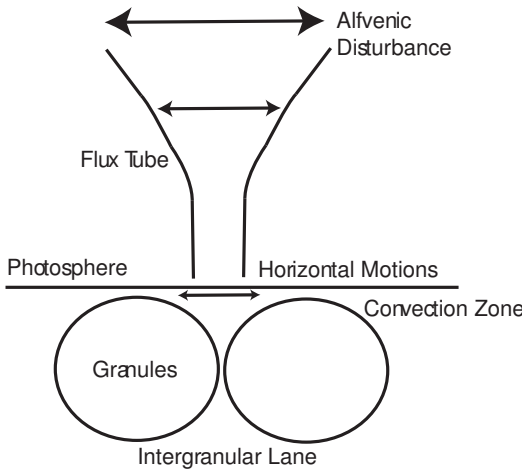

Figure 5.1: A cartoon diagram of how Alfvénic disturbances can be generated by horizontal motions at the surface and propagate upwards along open field structures which build up in inter-granular lanes.

Alfvén waves. As with the majority of atmospheric phenomena this effect is closely connected to the structure of the magnetic field.

It is well established that isolated strong vertical magnetic fields exist outside sunspots, in particular at the boundary of supergranulation cells (Proctor, 2004). In open field regions the solar wind is fed by oscillations originating in the convection zone, in particular Alfvén waves (Belcher, 1971; Hollweg, 1975; Tu, 1995; Goldstein et al., 1995). Open field structures can be formed by the concentration of vertical field at downdrafts at the edges of convection cells on the solar surface, and further magnification of the magnetic field occurs due to the convective instability (Stix, 2002). Horizontal motions at the surface can propagate upwards along these open flux tubes and reach the outer solar atmosphere, thus feeding the solar wind (see figure 5.1).

Typical frequencies of Alfvénic oscillations at the surface, derived from the horizontal motion of bright spots associated with magnetic fields, are in the range 3 seconds to 3 days, which correspond to frequencies of 1 Hz down to 1×10^{-6} Hz (Cranmer and Van Ballegooijen, 2005).

Not only is the study of the generation and propagation of Alfvén waves im-

portant for the solar wind but it is also important in the heating of the lower solar atmosphere. Waves generated at the photosphere can deposit their energy in the atmosphere above due to various damping mechanisms.

5.1.3 Damping of Alfvén Waves

The heating effect of MHD waves is connected with dissipation by a particular mechanism which converts the energy of the waves into energy of the background plasma. In the solar atmosphere the main damping mechanisms are collisional friction dissipation, viscosity and thermal conductivity. Viscous damping of MHD waves is caused by the momentum transfer of the thermal motion of particles. Collisional friction is caused by the relative velocities of the species in the plasma, while thermal conductivity is also related to kinetic effects and momentum transfer. These three energy dissipation mechanisms in the solar atmosphere have been studied in previous work (Khodachenko et al., 2004; Khodachenko et al., 2006). For a partially ionised plasma collisional friction damping is enhanced due to the ion-neutral drag which is driven by the Lorentz force. The efficiency of these mechanisms were compared for solar conditions by estimating effective damping timescales in the linear damping approximation. For waves propagating in the partially ionised chromosphere, the most dominant mechanism was shown to be the collisional friction due to ions and neutrals.

The passage of Alfvén waves through both the chromosphere and corona has been studied using measurements of magnetic bright point (MBP) positions in the photosphere. A frequency power spectrum for horizontal motions (Cranmer and Van Ballegooijen, 2005) at the photospheric level was derived in the frequency range 10^{-5} to 0.1 Hz. Using this as a lower boundary condition, a WKB approximation was applied to derive power spectra at different heights in the atmosphere to show the effective damping of waves in different regions. It was shown that waves in this range (10^{-5} to 0.1 Hz) may be evident up to a few solar radii which suggests that horizontal perturbations in this frequency range may be unaffected by the partially ionised chromosphere.

The damping of Alfvén waves, among other mechanisms, has been suggested as the driving mechanism behind spicules. Spicules are high, thin jet like structures

consisting of chromospheric plasma. They can reach heights of between 5000 and 9500 km whereupon they either fall back or fade in the hot corona. It has been suggested that they are driven by the dissipation of upwardly travelling Alfvén waves in open magnetic field structures, with the main damping mechanism being the collision friction transfer between ions and neutrals in the partially ionised chromosphere (De Pontieu and Haerendel, 1998; De Pontieu, 1999). Numerical simulations of Alfvén waves of frequencies around 0.5 Hz damped by ion-neutral collisions have been conducted in the WKB approximation. This approximation assumes that over a single wavelength there is no spatial variation of variables. More specifically, the wavelength itself does not change much on its own scale and the damping scale is much larger than the wavelength. De Pontieu et al. (2001) analytically calculated the damping time for Alfvén waves of varying frequencies in model chromospheres of various solar structures, given estimates for the plasma parameters in these regions. They estimated that frequencies above about 0.1 Hz are unable to penetrate through to the corona from the photosphere. In addition waves of these frequencies were able to provide enough momentum to the chromospheric plasma to cause upwards velocities which matched observations of spicules.

In other studies, James et al. (2003) obtained similar results by relaxing the WKB approximation, with waves with periods of 20s (0.05Hz) experienced little damping, while waves with periods of 2s (0.5Hz) were significantly attenuated. However, the ionisation levels were calculated using the Saha equation assuming local thermodynamic equilibrium (LTE). As chromospheric plasma is not in LTE these results need to be verified for non-LTE calculations, as outlined in Chapter 3.

In this Chapter MHD simulations of Alfvén waves are performed to find out which frequencies of Alfvén waves generated at the surface are damped by ion-neutral collisions in the partially ionised chromosphere. The simulations use realistic models for the solar atmosphere, and use the modified Saha equation to estimate the ionisation levels and therefore the profile of the Coulomb and Cowling resistivities. *Filter functions* are created which give the attenuation, or efficiency of damping of this mechanism as a function of frequency. The numerical results are then compared to analytic estimates of damping efficiency based on the linear damping approximation (Braginskii, 1965),

as well as the calculations made in the WKB approximation by the authors mentioned herein (De Pontieu et al., 2001; Cranmer and Van Ballegooijen, 2005) and in the MHD simulations also mentioned (James et al., 2003). The results contained in this chapter have been published in Astronomy and Astrophysics (Leake et al., 2005).

5.2 The Efficiency of Collisional Frictional Damping of Alfvén Waves

5.2.1 Analytic Approach

To obtain analytic expressions for the damping efficiency of ion-neutral collisions, the profiles of the Cowling and Coulomb resistivities for the quiet Sun, as derived in chapter 3, are used along with a model magnetic field. By using linear damping MHD analysis, the efficiency of damping of Alfvén waves which propagate through the partially ionised atmosphere of the Sun can be estimated.

Magnetic field model

The propagation of Alfvén waves is assumed to be restricted to propagation upwards along a vertical flux tube, which spreads out with height due to the decreasing gas pressure in the surrounding plasma (see figure 5.1). As Alfvén waves propagate along field lines the analysis can be restricted to one spatial dimension, along the field lines. Hence only the variation of the total magnetic field strength in this direction is needed. By varying this magnitude in such a way so that the total flux through the cross-section of such a flux tube is constant, the horizontal expansion does not enter explicitly into the calculations. A power law dependence on density is chosen

$$B = B_0 \left(\frac{\rho}{\rho_{ph}} \right)^{\alpha} \tag{5.3}$$

where ρ_{ph} is the photospheric density $2.7 \times 10^{-4}\,\mathrm{kg/m^3}$ taken from the VALC model of the quiet Sun and B_0 is 1200 G. This profile is chosen so that at the base of the domain the magnetic field is approximately 1000 G and falls to a value of about 10 G at a height of 3000km. This is a simplistic model for the magnetic field but captures the

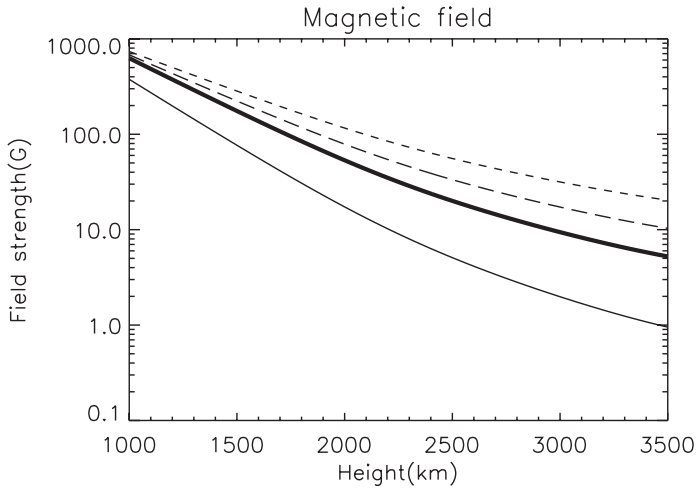

Figure 5.2: The variation of the model background magnetic field with height. The four curves relate to the value of the exponent $\alpha = 0.2$ (small dash line), 0.35 (large dash line), 0.4 (thick solid line) and 0.6 (thin solid line).

observed decrease with height and enables comparison of analytic and numerical results. Martinez-Pillet et al. (1997) showed that the field strength in flux tubes can drop to as little as 300 G at heights of only 800km so this is used as the minimum value of magnetic field at this height for the model. The magnetic field profile for four different power law profiles are shown in figure 5.2.

As in chapter 3, using this field model, η_c can be calculated as a function of height in the quiet Sun, and can be compared to η. Figure 5.3 shows the resistivities for a magnetic field profile given by equation (5.3) and with $\alpha = 0.2$.

Linear damping

Braginskii (1965) derived damping length-scales for various damping mechanisms in a partially ionised plasma, for fast, slow and Alfvén waves . These damping length-scales or *damping decrements* can be used to express the inverse timescale of damping of propagating waves, and hence be used to gain an estimate of the efficiency of the damping mechanism. An Alfvén wave propagating with angular frequency ω and with

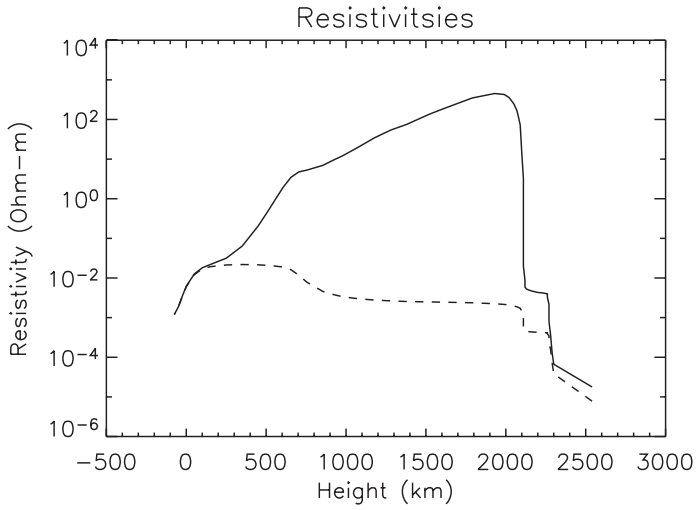

Figure 5.3: Cowling (solid line) and Coulomb (dashed line) resistivities as a function of height calculated using ionisation levels from the modified Saha equation using varying $|\mathbf{B}|$ with height, with $\alpha = 0.2$.

wave number k can be expressed by the harmonic expression

$$\exp\left(-i(\mathbf{k}.\mathbf{r} - \omega t)\right) \tag{5.4}$$

for the perturbations in magnetic field and velocity.

The damping decrement δ for collisional friction damping, as calculated by Braginskii (1965) is given by

$$2\omega\delta \equiv \frac{1}{\tau} = \eta_{\parallel} {k_{\perp}}^2 + \eta_c {k_{\parallel}}^2. \tag{5.5}$$

$k_{\parallel}$ is the wavenumber parallel to the magnetic field $\mathbf{B}$, and wavenumber $k_{\perp}$ is perpendicular.

The linear MHD analysis used to obtain these damping decrements (Braginskii, 1965) assumes that the damping decrement δ is much less than 1. This implies that

$$\delta = \frac{\eta_c {k_{\parallel}}^2}{2\mu_0\omega} \ll 1 \tag{5.6}$$

or that

$$\omega \ll \omega_{crit} = \frac{2\mu_0 {c_A}^2}{\eta_c}. \tag{5.7}$$

For the model used here both η_c and the Alfvén speed

$$c_A = \frac{B}{(\mu_0 \rho)^{\frac{1}{2}}} \tag{5.8}$$

are functions of height so the damping decrement also varies with height. Over a small timestep *dt* the amplitude A of the propagating wave changes by

$$\begin{aligned} A &= A_0 \exp\left(-\frac{dt}{\tau}\right) \\ &= A_0 \exp\left(-dt\frac{\eta_c(z)}{\mu_0}k_{||}(z)^2\right) \\ &= A_0 \exp\left(-dz\frac{\eta_c(z)}{\mu_0 c_A(z)^3}\omega^2\right) \end{aligned} \tag{5.9}$$

By integrating over the entire vertical domain an estimate for the total change in amplitude due to the damping can be made

$$E = \frac{A_0 - A}{A_0} = 1 - exp\left[-\omega^2 \int \frac{\eta_c(z)}{\mu_0 c_A(z)^3} dz\right] \tag{5.10}$$

where the integral can be performed numerically. The results from this approximation are shown in figure 5.4 for the four different magnetic field models (different α). From these estimates it appears that in the absence of any other damping mechanisms and stratification effects, high frequency Alfvén waves are unable to pass through this partially ionised region without being completely damped. For the magnetic field model with $\alpha = 0.2$ this upper limit can be as low as 0.1 Hz.

5.2.2 Numerical Simulations

Alfvén wave propagation is simulated by numerically solving the governing equations for a partially ionised plasma derived in chapter 2. In this way a realistic model for the atmosphere can be constructed, which includes gravitation and stratification. The propagation of Alfvén waves can be simulated by driving waves in the model photosphere and following their evolution through the partially ionised region. The values of the ionisation level and resistivities are obtained using the modified Saha equation. This method thus represents a more realistic approach to modeling the propagation of Alfvén waves in the chromosphere. This approach does not rely on the WKB approximation,

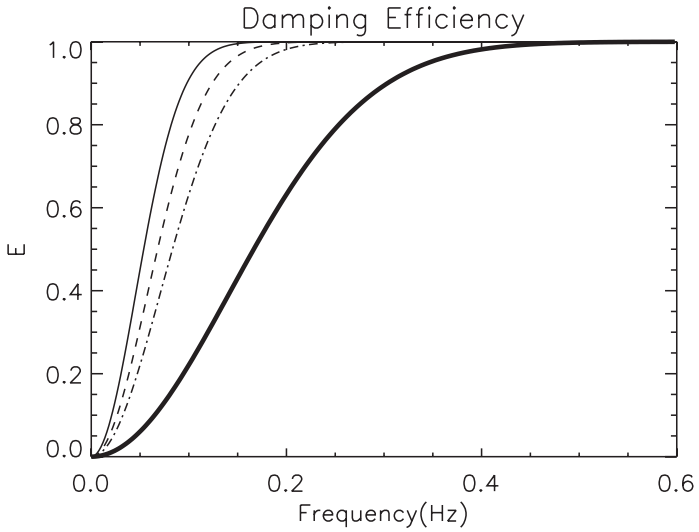

Figure 5.4: Analytical estimates for the damping efficiency of Alfvén waves in the partially ionised region of the solar chromosphere, as a function of frequency. The four lines represent the four magnetic field profile given by $\alpha = 0.2$ (thin solid line). 0.35 (dashed line), 0.4 (dot-dashed line) and 0.6 (thick solid line).

and so the results can be compared with the work of De Pontieu et al. (2001) to verify their results.

To simulate the motion of waves in the chromospheric region of the solar atmosphere, the magnetic field model used is a spreading vertical flux tube representing an open magnetic structure with its footpoint in the photosphere (see equation (5.3)). The footpoint is assumed to be the generation point of Alfvén waves and the propagation to be vertical upwards.

Model atmosphere

In order to define the model atmosphere the temperature profile in the VALC model (Vernazza et al., 1981) is used as a guide for the model temperature in these simulations. The temperature profile used is

$$T(y) = T_{ph} + \frac{(T_{cor} - T_{ph})}{2}\left[\tanh\left(\frac{y - y_{cor}}{w_{tr}}\right) + 1\right]. \qquad (5.11)$$

This represents two isothermal regions (models of the photosphere/chromosphere at temperature T_{ph} and corona at temperature T_{cor}) separated by a transition region of width w_{tr}. The values used in these simulations are

$$T_{ph} = 5700\,\mathrm{K} \tag{5.12}$$

$$T_{cor} = 150\,T_{ph} \tag{5.13}$$

$$y_{cor} = 3750\,\mathrm{km} \tag{5.14}$$

$$w_{tr} = 750\,\mathrm{km} \tag{5.15}$$

Assuming the unperturbed atmosphere is in hydrostatic equilibrium gives

$$\frac{d}{dy}\left(\frac{\rho k_B T}{\mu_m}\right) = -\rho g. \tag{5.16}$$

It was shown in chapter 2 that for a Hydrogen plasma of varying ionisation

$$\mu_m = \frac{m_i}{2-\xi_n}. \tag{5.17}$$

However, the solar atmosphere also contains Helium. As the first ionisation of Helium is higher than that for Hydrogen, there will also be neutral Helium present. A full calculation of the pressure would include the relative number of neutral Helium to Helium ions, but this is over-complicated. To account for the effect of Helium on the mean mass a prefactor of 1.2 is used (the value represents the fractional increase in mean mass using the relative abundances of Hydrogen and Helium). This is a simplification, but the relative number of Helium to Hydrogen is small (around 0.1), so the effect of neutral Hydrogen on the mean mass calculation is small.

Equation (5.16) is a differential equation for the density, provided the mean mass and the temperature are known. However, the mean mass depends on the ionisation level and hence, via the modified Saha equation, on both density and temperature.

$$\mu_m = \frac{m_i}{2-\xi_n} = f(\rho, T) \tag{5.18}$$

In order to solve for the density using equation (5.16), the mean mass must already be known, which is itself a function of density, meaning an implicit method must be used. A simple iterative method is used to simultaneously find the density and

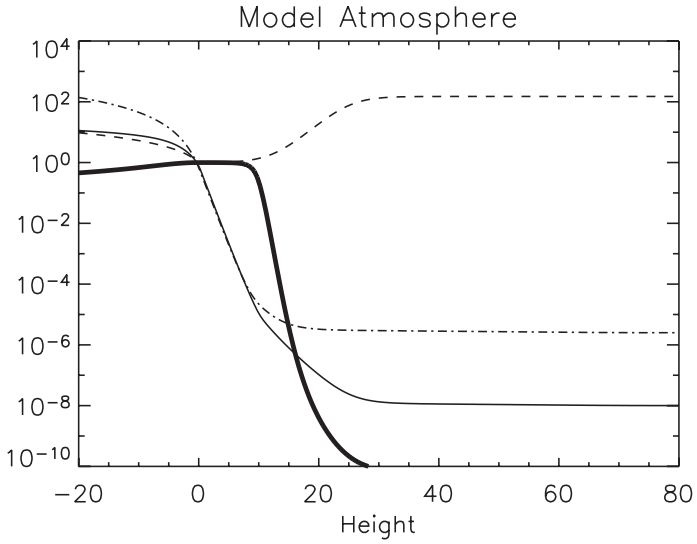

Figure 5.5: Model atmosphere showing density (thin solid line), temperature (dashed line), gas pressure (dot-dashed line) and neutral fraction (thick solid line). The height is in units of photospheric scale height.

mean mass profiles, given the temperature profile. This is done by initially setting the mean mass to a constant profile and then iteratively solving (5.16) and recalculating μ_m until both profiles of μ_m and ρ converge.

The hydrostatic equation (5.16) must be solved numerically. The details of this are given in appendix A. The resultant density, temperature and gas pressure are shown in figure 5.5 along with the neutral fraction. As can be seen, the neutral fraction falls to zero as the temperature passes the ionisation temperature of Hydrogen. The magnetic field profile is the same as used in the analytic approach.

Alfvén wave initialisation

To initiate Alfvén waves at the base of the domain, the horizontal velocity v_x is driven with a sinusoidal function continuously at the bottom of the domain. The frequency of the sinusoidal function represents the frequency of the travelling wave. The amplitude of the driving function varies with typical driving velocities of 600 m/s and a range of 80 to 800 m/s being used. The amplitudes had little effect on the results presented

here.

Numerical method

The propagation of Alfvén waves in a partially ionised plasma is modeled in 1D by numerically solving the non-ideal partially ionised MHD equations, given here in dimensionless form.

$$\frac{D\rho}{Dt} = -\rho\nabla.\mathbf{v} \tag{5.19}$$

$$\frac{D\mathbf{v}}{Dt} = -\frac{1}{\rho}\nabla P + \frac{1}{\rho}\mathbf{j}\wedge\mathbf{B} + \mathbf{g} \tag{5.20}$$

$$\frac{D\mathbf{B}}{Dt} = (\mathbf{B}.\nabla)\mathbf{v} - \mathbf{B}(\nabla.\mathbf{v}) - \nabla\wedge(\eta\mathbf{j}_{\parallel}) - \nabla\wedge(\eta_c\mathbf{j}_{\perp}) \tag{5.21}$$

$$\frac{D\epsilon}{Dt} = -\frac{P}{\rho}\nabla.\mathbf{v} + \frac{1}{\rho}\eta {j_{\parallel}}^2 + \frac{1}{\rho}\eta_c {j_{\perp}}^2 + \frac{1}{\rho}\Pi_{ij}S_{ij} - \frac{\epsilon-\epsilon_0}{\tau} \tag{5.22}$$

which also include the Coulomb and Cowling resistivities. $\mathbf{B}$ is the magnetic field, $\mathbf{j} = \nabla\wedge\mathbf{B}$ is the current density, and $\mathbf{j}_{\parallel}$ and $\mathbf{j}_{\perp}$ are its components parallel and perpendicular to the magnetic field, respectively. $\mathbf{v}$ is the velocity, P is the thermal pressure, and ϵ is the specific internal energy density. The constants μ_0 and γ have the standard meanings of magnetic permittivity of free space and the ratio of specific heats respectively. Although for a partially ionised plasma $\gamma < 5/3$ the value had little effect on the results so $5/3$ was used in all simulations.

It is worth noting that no viscous effects are included in these model equations as only collisional damping is being investigated in this work. However, as mentioned at the start of this chapter, the main damping mechanism in the partially ionised regions of the solar atmosphere is ion-neutral collisions.

The simulations are carried out using the 2D Lare code, adapted as in chapter 4. Although the code is run in 1D all vector variables have 3 components.

The simulation domain extends 3000 km vertically, while the computational grid consists of 2000 cells. The number of cells vertically is restricted by the need to resolve the smallest wavelengths in the parametric study. The grid is stretched so that higher resolution is used at the lower part of the domain where the wavelengths are shorter

(the wavelength of the upwardly propagating wave increases with height due to the change in the Alfvén speed. The vertical boundary conditions are line-tied which are perfectly reflecting, and the simulation ends when the Alfvén waves have reached the upper boundary.

All quantities are non-dimensionalised by using values at the photosphere.

$$\begin{aligned} r^* &= 150\,\mathrm{km} \\ \rho^* &= 2.7 \times 10^{-4}\,\mathrm{kg/m^3} \\ v^* &= 6515\,\mathrm{m/s} \\ t^* &= 23\,\mathrm{s} \\ T^* &= 6420\,\mathrm{K} \\ P^* &= 1.17 \times 10^4\,\mathrm{Pa} \\ B^* &= 1000\,\mathrm{G} \end{aligned}$$

Conversion to variables with dimensions merely requires the multiplication of internal variables by these values.

As has been shown in chapter 3 the Cowling resistivity $\eta_\mathbf{c}$ is much larger than the Coulomb resistivity η at chromospheric heights. In fact over the domain being simulated, the calculated value of η using the density and temperature values for the plasma never exceeds the value of numerical roundoff in the code, and hence all simulations are run with $\eta = 0$.

Results

The dissipation of these waves can now be investigated by observing the change in amplitudes of the Alfvénic perturbations as they propagate upwards along the field lines of the vertical flux tube. Figure 5.6 shows a typical profile of the perpendicular velocity and magnetic field perturbations with height for a driving frequency of 0.07 Hz, for two cases. The first is when there is no damping mechanism present and the second is when collisional friction damping is applied with the given profile of η_c with the value of α being 0.2.

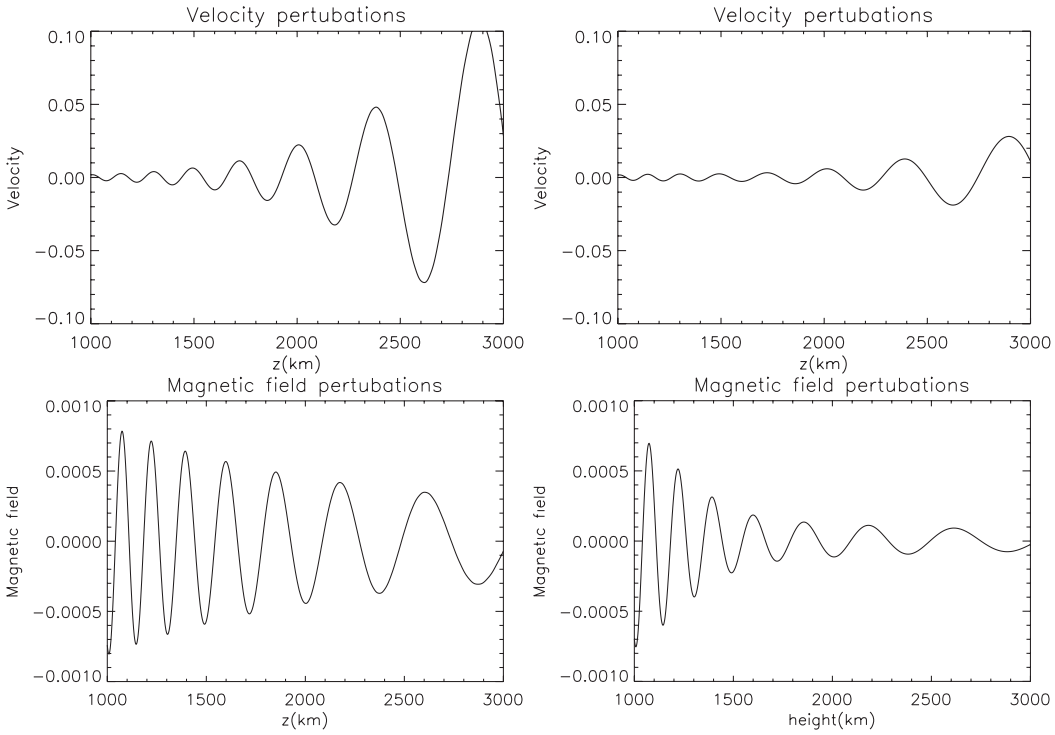

Figure 5.6: Velocity (top panels) and magnetic field (bottom panels) perturbations as a function of height for a typical run with $f = 0.07$Hz, The left hand panels are for the case of $\eta_c = 0$ and the right hand panels are for the η_c calculated at each step. The velocity and magnetic field are given in dimensionless units.

By comparing the propagation of Alfvén waves in the presence of a partially ionised region and without, the efficiency of damping due to collsional friction of ions and neutrals in the partially ionised chromosphere can be estimated.

As can be seen from the two left panels from figure 5.6, the gravitational stratification causes an increase in amplitude of the velocity perturbation and a decay in the corresponding magnetic field perturbations. This is a consequence of energy conservation in the travelling wave. For a rigorous mathematical treatment of this see De Moortel and Hood (2004). This makes a direct calculation of the efficiency of the collisional frictional damping non-trivial.

In order to obtain an estimate for the efficiency of collisional friction damping the Poynting flux carried by the waves is compared for the two simulations. Poynting flux is given by

$$\mathbf{S} = \frac{\mathbf{E} \wedge \mathbf{B}}{\mu_0}. \tag{5.23}$$

Hence the time-averaged Poynting flux for the Alfvén waves is given by

$$< S >= \frac{B_0 < b_x v_x >}{\mu_0} \tag{5.24}$$

where B_0 is the vertical background magnetic field and b_x, v_x are the perturbations in magnetic field and velocity. By calculating the ratio of Poynting flux at a height above the partially ionised region of the model chromosphere for the two simulations the efficiency of the damping mechanism is found. The ratio of damped to undamped Poynting flux at a height of 2500km above the surface (i.e. above the region of high Cowling resistivity) is given by

$$\gamma_r = \frac{< S >_{damped}}{< S >_{undamped}} \tag{5.25}$$

and for direct comparison with the analytic results the efficiency of damping is estimated simply by

$$E = 1 - \gamma_r. \tag{5.26}$$

Figures 5.7-5.10 show this estimate as a function of frequency, along with the estimate from the analytic approach. The four different plots are for the four different magnetic field profiles, with α being 0.2, 0.35, 0.4 and 0.6 respectively. As the power

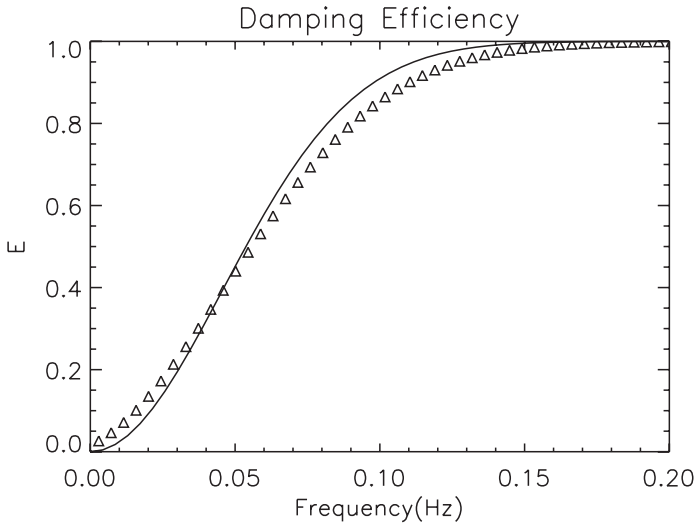

Figure 5.7: Estimates of the efficiency of damping due to ion-neutral collisions for the magnetic field profile with power law $\alpha = 0.2$. The solid line is the estimate due to analytic approaches and the triangles represent the estimates obtained from numerical data.

law for the magnetic field changes so does the estimate for the damping efficiency, as the value of η_c is dependent on $|\mathbf{B}|$.

The numerical data agrees best with the analytical estimates when α is smallest (see figure 5.7). For this profile the two approaches agree in the middle of the frequency range, but disagree at low and high frequencies. The differences at low frequencies are due to limitations in the procedure outlined in equations (5.24)-(5.26). The differences at high frequencies are due to the fact that the analytic approach is only applicable when the driving frequency is well below the critical value (criteria (5.7)), i.e in the linear damping approximation.

The difference between numerical and analytic data increases as the value of α increases (figures 5.7-5.10). By increasing the power in the magnetic field profile in equation (5.3), the effect of ion-neutral collsional friction damping is decreased, as η_c becomes smaller. This increases the relative importance of any other effects on the wave amplitude, such as stratification. Thus the difference in numerical and analytic data is due to the fact that the numerical approach includes the stratification effects on the

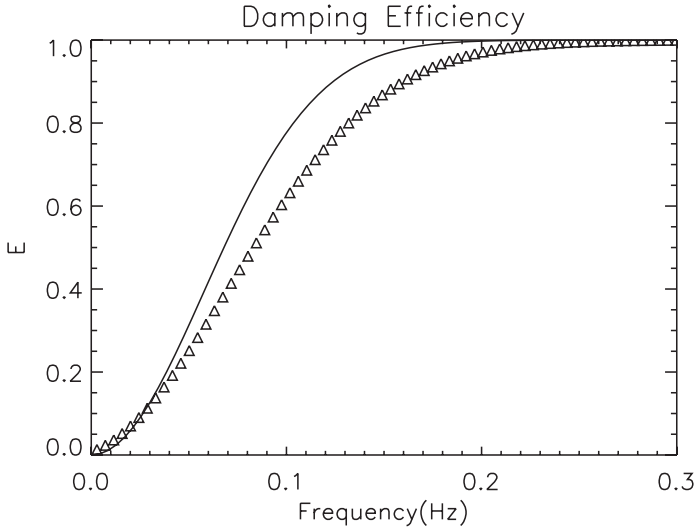

Figure 5.8: Estimates of the efficiency of damping due to ion-neutral collisions for the magnetic field profile with power law $\alpha = 0.35$. The solid line is the estimate due to analytic approaches and the triangles represent the estimates obtained from numerical data.

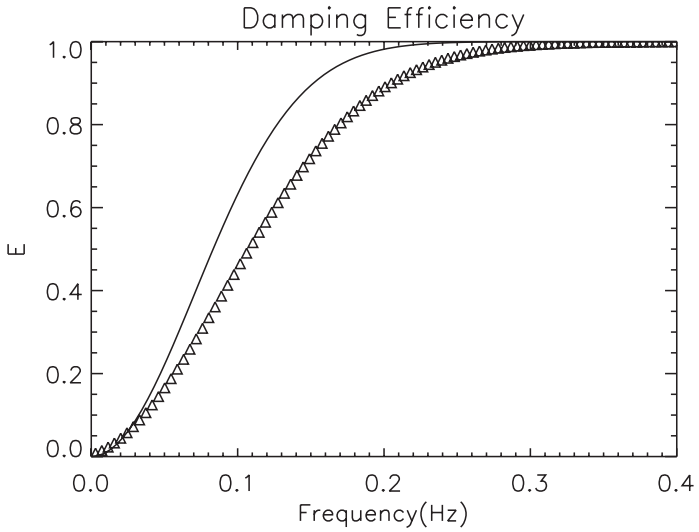

Figure 5.9: Estimates of the efficiency of damping due to ion-neutral collisions for the magnetic field profile with power law $\alpha = 0.4$. The solid line is the estimate due to analytic approaches and the triangles represent the estimates obtained from numerical data.

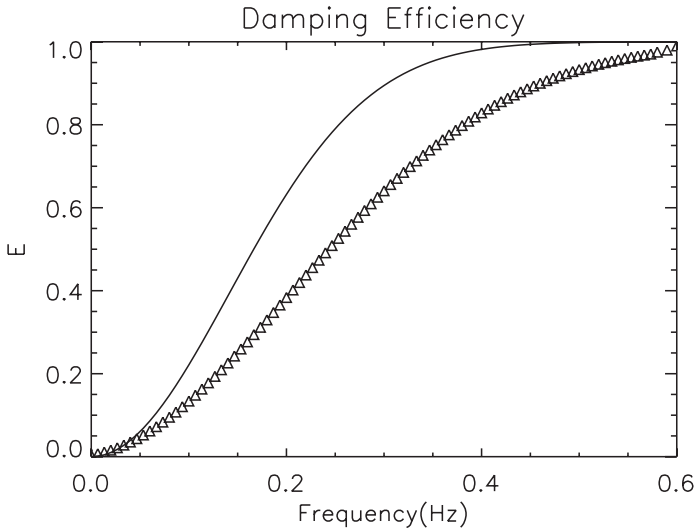

Figure 5.10: Estimates of the efficiency of damping due to ion-neutral collisions for the magnetic field profile with power law $\alpha = 0.6$. The solid line is the estimate due to analytic approaches and the triangles represent the estimates obtained from numerical data.

wave amplitudes, whereas the analytic approach does not.

From both analytical and numerical data it can be seen that Alfvén waves with frequencies below 0.01 Hz are unaffected by this damping mechanism, and propagate through the partially ionised region with little diffusion. Waves with frequency above 0.6 Hz are completely damped by this mechanism.

5.3 Conclusions

The efficiency of the partially ionised solar chromosphere in damping Alfvén waves generated at the surface has been estimated. The estimates are based on analytic and numerical approaches, which agree in the linear damping approximation. The damping mechanism is the collisional friction between neutral and ion species in a model partially ionised Hydrogen plasma with temperature and density values based on the VALC model of the quiet Sun (Vernazza et al., 1981).

Alfvén waves of frequencies above 0.6 Hz are completely damped by the partially

ionised layer in the chromosphere, whereas waves of frequency below 0.01 Hz are unaffected by the presence of neutrals and experienced no damping due to this mechanism. This lower value agrees with work conducted on MBP's and power spectra of horizontal motions at different heights in the atmosphere (Cranmer and Van Ballegooijen, 2005). They showed that using the WKB approximation the power spectra for motions with frequencies below 0.01 Hz are essentially unchanged as one progresses up the chromosphere to the transition region. This suggests that there is very little damping of low frequency waves due to any kind of dissipation mechanism in the solar chromosphere.

The form of the dissipation efficiency calculated from numerical data differs from that obtained from linear analytic approximations. Small differences could be seen at low frequencies (due to errors in the estimation of small damping decrements). Differences also occurred at higher frequencies, although both analytic and numerical estimates of the efficiency converge to 1 at high frequencies. The difference at higher frequencies is due to the fact that the linear damping approximation is not valid (5.7).

The numerical simulations were performed in the non-ideal MHD approximation with an additional term relating to the Cowling resistivity in the generalised Ohm's law. Previous work on Alfvén wave propagation in the lower solar atmosphere has used the WKB assumption, as used by (De Pontieu et al., 2001). This assumes that the change in wavelength, as well as plasma variables, is small over a typical wavelength. They estimated that in this regime the ion-neutral collisions in the chromosphere damped waves of frequencies above 0.1 Hz. However, the WKB approximation fails at low frequencies when the wavelength is larger. These results show that high frequency waves are heavily attenuated by ion-neutral collisions but as is clear from figures 5.7-5.10 the result is very sensitive to the spreading out of the flux tube and decrease in $|\mathbf{B}|$. Over the range of values of α, chosen to match estimates of $|\mathbf{B}|$ from observations, the damping is very effective over a range 0.1 to 0.6 Hz depending on α. This work is also in broad agreement with the work of James et al. (2003), which gives similar upper limits on the frequency that can propagate through the partially ionised regions of the solar atmosphere. However, these simulations used non-LTE calculations of the ionisation whereas pervious work did not.

Although higher frequency waves are difficult to observe directly, photospheric motions can theoretically generate a large spectrum of Alfvén waves. The fact that the partially ionised layer completely damps any waves above 0.6 Hz for these magnetic field models means that any high frequency waves present in the upper atmosphere must have been created by other sources than photospheric motions.

This work is based on upward travelling waves generated at the photospheric level. Downward travelling waves from the corona would be reflected at the density contrast above the chromospheric region where the Cowling resistivity is large and it is unclear whether this damping mechanism would be important. The case of downward propagating waves will be subject to further investigation.

The model atmosphere is assumed to be magnetised, and thus the Generalised Ohm's law does not include the Hall term. In the upper photosphere, the electrons are tightly bound to the magnetic field whereas the ions are not. In this case there is a separation electric field due to the neutrals drag on the non-magnetised ion, which should be taken into account in the single fluid equations. However, it was shown that the damping of Alfvén waves is most efficient at heights of 1000 km to 2000 km and in this region the plasma can be regarded as magnetised.

Chapter 6

2D Simulations of Emerging Magnetic Flux

6.1 Introduction

The study of the emergence of magnetic field into the solar atmosphere is important for understanding the coupling of dynamo fields in the interior of the Sun not only with active regions on the surface, but also with the associated events in the atmosphere above.

It is well established that magnetic flux can be lifted from the base of the convection zone in the form of thin twisted flux tubes (Matthews et al., 1995). These flux tubes can rise to the surface due to the super-adiabatic nature of the convection zone. The emergence of these flux tubes is thought to be the cause of new active regions being formed (Parker, 1955; Zwann, 1978). The flux tubes at the base of the convection zone are thin in the sense that the tube radius is small compared to the local scale height, which is not true in the upper regions of the convection zone. More importantly, the temperature gradient at the surface becomes sub-adiabatic, so that buoyancy cannot drive the flux tubes from beneath the surface into the atmosphere above. Another mechanism must do this, and the most likely candidate is the magnetic buoyancy instability (Parker, 1979; Matsumoto and Shibata, 1992; Matsumoto et al., 1993; Magara and Longcope, 2001; Shibata et al., 1989; Shibata et al., 1989).

Current models of flux emergence have very simple treatments of the energy exchange in the solar atmosphere. This is due to the complications involved in including in the models all the heating/cooling mechanisms in the solar atmosphere. While previous work on flux emergence has given valuable insight into the nature of flux emergence into the solar atmosphere, the effect of heat transfer as flux emerges though the lower atmosphere and into the corona is still unknown.

Previous work on flux emergence has modeled the solar atmosphere as a fully ionised plasma of high magnetic Reynold's number (Archontis et al., 2004; Fan, 2001; Manchester, 2001). In previous chapters it has been shown that the solar atmosphere cannot be assumed to be fully ionised everywhere, but that the ionisation level changes with height. The presence of neutrals introduces an additional dissipation mechanism, which manifests itself in anisotropic dissipation of currents. For the quiet Sun, it was shown that this dissipation can become important relative to advective effects. The partially ionised region can have low magnetic Reynolds numbers and thus the evolution of the magnetic field can be dominated by diffusion rather than advection. Furthermore it has been shown that given solar parameters, this additional dissipation mechanism can heavily attenuate high frequency upflowing Alfvén waves

In this chapter the importance of including the additional effects of partial ionisation in flux emergence models is investigated. The results presented here are from 2.5D simulations, i.e 2 independent spatial variables and 3D vector dependent variables. In this way the evolution of a flux tube's cross-section can be simulated. This obviously includes no phenomena which occurs along the tube axis, which may be important for the emergence of flux into the atmosphere (Manchester, 2001; Manchester et al., 2004). Results from 3D simulations are presented in chapter 7. Some of the work presented in this chapter has been published in Leake and Arber (2006).

6.2 Numerical Simulations

The simulations presented in this chapter model the evolution of magnetic field in the upper convection zone and atmosphere of the Sun. Firstly, a simple model for

the unperturbed solar atmosphere is constructed. This model comprises the upper convection zone, photosphere/chromosphere, transition region, and corona, and is based on values taken from the VALC model of the Sun (Vernazza et al., 1981). Secondly a magnetic flux tube is superimposed on this background atmosphere. This magnetic field profile will have a number of free parameters, which in principle can be varied systematically to investigate the effect of the initial model on the results. The buoyant rise of this flux tube can be initiated in a variety of ways, mentioned later in this chapter. The evolution of this flux tube is then simulated by numerically solving the governing equations.

6.2.1 Model atmosphere

The model temperature profile for these simulations is similar to that used in chapter 5, comprising an isothermal photosphere/chromosphere, transition region and isothermal corona. In addition the upper convection zone immediately beneath the surface is modeled by a linear polytrope. The temperature profile is

$$T(y) = T_{ph} - a\frac{g}{m+1}y\,,\; y<0 \tag{6.1}$$

$$= T_{ph} + \frac{T_{cor}-T_{ph}}{2}\left[\tanh\left(\frac{y-y_{cor}}{w_{tr}}\right)+1\right]\,,\; y>0. \tag{6.2}$$

The photospheric temperature, T_{ph} is 5700K, the coronal temperature T_{cor} is 8.5×10^5K. The width of the transition region w_{tr} is 750km. The vertical domain (y) extends from 3000 km below the surface to 10000 km above the surface.

The polytropic index is given by m and is set to the adiabatic value $\frac{1}{\gamma-1}$. The parameter a is used to control how superadiabatic the model convection zone is. If $a=1$ then the temperature profile is on the critical value for convection to occur

$$\frac{dT}{dy} < \left(\frac{dT}{dy}\right)_a = \frac{(\gamma-1)}{\gamma}\frac{T}{P}\frac{dP}{dy}. \tag{6.3}$$

If $a>1$ then the temperature gradient satisfies the condition for instability and any initial buoyancy of a parcel of plasma will persist until the atmosphere becomes stable.

This temperature profile is shown together with values taken from the VALC model of the quiet Sun (Vernazza et al., 1981) in figure 6.1. Although a simplistic

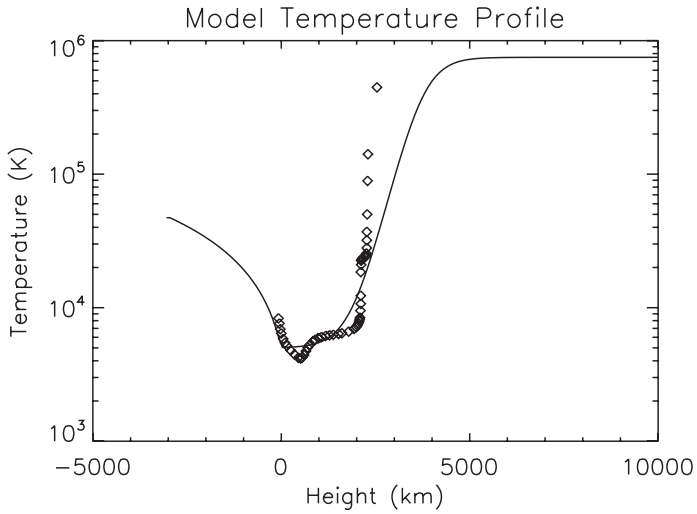

Figure 6.1: The initial temperature profile of the model background atmosphere (solid line), along with values taken from the VALC model of the quiet Sun (diamonds).

version of the real solar atmosphere, it captures the main features of the temperature profile.

As in Chapter 5, the density and pressure of the background atmosphere are found from solving the hydrostatic equation

$$\frac{dP}{dy} = -\rho g \tag{6.4}$$

where

$$P = \frac{n_T k_B T}{\mu_m}. \tag{6.5}$$

For a fully ionised Hydrogen plasma, $\mu_m = \frac{m_p}{2}$. Previous simulations of flux emergence have used a value of $\mu_m = m_p$, which is designed to account for the effect of heavier elements and neutral atoms on the mean mass (Archontis et al., 2004; Magara, 2001). For comparison with these simulations, this is the value used here for the fully ionised model of the solar atmosphere. For a partially ionised Hydrogen plasma, it was shown in chapter 2 that $\mu_m = \frac{1}{2-\xi_n}$. As in chapter 5, the following form for μ_m is used.

$$\mu_m = \frac{1.2}{2 - \xi_n} \tag{6.6}$$

The mean mass depends on the neutral fraction ξ_n which is a function of temperature. The factor 1.2 represents contribution from heavier elements. As in chapter 5, given the

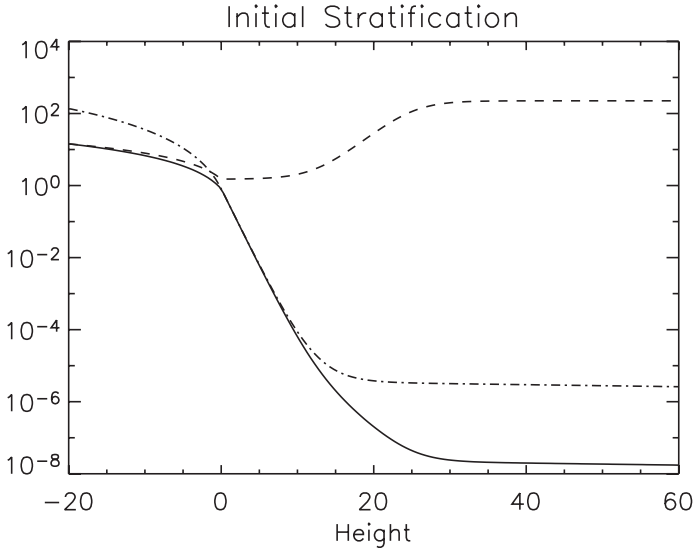

Figure 6.2: The initial stratification of the background atmosphere. The dashed line is the temperature, the solid line is the density and the dot-dash line is the gas pressure. All values are normalised to values at the surface, y=0. The height is normalised to the scale height at the surface.

temperature profile of the background atmosphere, the hydrostatic equation and mean mass equation are solved simultaneously to obtain the stratification, which is shown in figure 6.2.

6.2.2 Initial Magnetic Field Profile

To simulate the evolution of a magnetic flux tube in the convection zone, a magnetic field profile is superimposed on the background stratification. This is done by defining a magnetic field profile which represents a twisted flux tube, having axial field B_a and azimuthal field B_T. There are generally two choices of magnetic field profile.

The first is the *Gold-Hoyle* force-free flux tube. This is force-free ($\mathbf{j} \wedge \mathbf{B} = 0$) and therefore exerts no force on the surrounding plasma, and the entire initialisation is in equilibrium. In previous literature this initialisation is commonly called mechanical equilibrium (MEQ). To initiate the rise of the flux tube, vertical velocities must be imposed upon the flux tube (Magara, 2001; Manchester et al., 2004).

However, the plasma β in the convection zone is much greater than unity and

gas pressure dominates over magnetic pressure. In this case the equilibrium equation reduces to $\nabla P = \rho \mathbf{g}$ not $\mathbf{j} \wedge \mathbf{B} = 0$ as it does in the low β corona. Therefore there is no reason to specify the magnetic field in the convection zone as force-free.

The second choice is to use a non-force free field, so that the tube will exert a force on the plasma ($\mathbf{j} \wedge \mathbf{B} \neq 0$). A typical non-force free profile, as used by Fan (2001) is

$$B_a = B_0 \exp\left(-\frac{r^2}{a^2}\right) \tag{6.7}$$

$$B_T = qrB_a \tag{6.8}$$

where r is the radius from the centre of the tube's cross-section, a is the width and q is known as the twist.

$$q = \frac{B_T}{rB_a} \tag{6.9}$$

The plasma pressure inside the tube differs from the field-free pressure ($p_0(r)$) by $p_1(r)$, where

$$\frac{dp_1(r)}{dr}\hat{\mathbf{e}_\mathbf{r}} = \mathbf{j} \wedge \mathbf{B}, \tag{6.10}$$

so that the pressure gradient matches the Lorentz force. The change in density inside the flux tube relative to the field free atmosphere is specified by assuming the tube to be in thermal equilibrium with its surroundings.

$$T_0(y) = \frac{p_0(y)\mu_m}{\rho_0(y)} = \frac{(p_0(y) + p_1(r))\mu_m}{\rho_0(y) + \rho_1(r)} \tag{6.11}$$

Hence the density inside the tube differs from the field-free atmosphere ($\rho_0(y)$) by

$$\rho_1(r) = \frac{p_1(r)\mu_m}{T_0(y)}. \tag{6.12}$$

It has been argued that MEQ is preferable to TBL as an initialisation (Caligari et al., 1998), as it has less free-parameters. TBL is used here because there is no specific reason to assume the sub-surface field as force-free. Also the level of buoyancy in the tube in TBL initialisations can be varied to match observations of motions of emerging active regions (Caligari et al., 1995).

As mentioned in chapter 1, there is a range of twist which a flux tube can have to survive the convection zone. The minimum value is

$$|q_{min}| = \frac{1}{a}. \tag{6.13}$$

For these simulations, a value of $B_0 = 5$ is used which corresponds to 6000 G, using the gas pressure from the model at the tube depth, this corresponds to a value of plasma β of 10. The width is set to 2, which corresponds to a value much smaller than the typical size of sunspots. However, as the flux tube reaches the less dense atmosphere there will be significant expansion. The twist is set to the minimum value required to avoid fragmentation (6.13). As only a small amount of convection zone is being modeled, the tube will experience little deformation. For a full investigation into the effect of initial magnetic field models on the buoyant rise in the convection zone see Magara (2001).

6.2.3 Equations

The equations used to model the partially ionised plasma of the convection zone and atmosphere are given here in Lagrangian dimensionless form, with all the usual meanings.

$$\frac{D\rho}{Dt} = -\rho\nabla.\mathbf{v} \tag{6.14}$$

$$\frac{D\mathbf{v}}{Dt} = -\frac{1}{\rho}\nabla P + \frac{1}{\rho}\mathbf{j}\wedge\mathbf{B} + \mathbf{g} + \nabla.\mathbf{S} \tag{6.15}$$

$$\frac{D\mathbf{B}}{Dt} = (\mathbf{B}.\nabla)\mathbf{v} - \mathbf{B}(\nabla.\mathbf{v}) - \nabla\wedge(\eta\mathbf{j}_{\|}) - \nabla\wedge(\eta_c\mathbf{j}_{\perp}) \tag{6.16}$$

$$\frac{D\epsilon}{Dt} = -\frac{P}{\rho}\nabla.\mathbf{v} + \frac{\eta}{\rho}{j_{\|}}^2 + \frac{\eta_c}{\rho}{j_{\perp}}^2 + \frac{1}{\rho}\Pi_{ij}S_{ij} - \frac{\epsilon-\epsilon_0(\rho)}{\tau} \tag{6.17}$$

The energy equation includes the ad-hoc heating term which represents all heating mechanisms which cannot be included directly into the code but are present in the atmosphere of the Sun. As in chapter 5, these equations were normalised to values at

the photosphere,

$$\begin{aligned} r^* &= 150\,\mathrm{km} \\ \rho^* &= 2.7 \times 10^{-4}\,\mathrm{kg/m^3} \\ v^* &= 6515\,\mathrm{m/s} \\ t^* &= 23\,\mathrm{s} \\ T^* &= 6420\,\mathrm{K} \\ P^* &= 1.17 \times 10^4\,\mathrm{Pa} \\ B^* &= 1000\,\mathrm{G}. \end{aligned}$$

Unless stated all values are in dimensionless units and should be multiplied by these values to recover dimensional units.

Equations (6.14)-(6.17) reduce to the equations for a fully ionised plasma when $\xi_n = 0$ and $\eta_c = \eta$, so comparison between fully ionised and partially ionised simulations is straightforward.

6.2.4 Numerical Method

The computational domain extends from -20 to 80 in the vertical direction (corresponding to heights of -3000 km to 12000 km) with the surface being defined by $y = 0$. The horizontal domain extends from -50 to 50 (-7500 km to 7500 km). The horizontal domain is a uniform grid with open boundaries at each side. These open boundaries allow the flow of matter and magnetic field out of the domain. The vertical domain is stretched so that more grid points are located within the region -20 to 20 so as to capture the structure of the magnetic field better. The vertical boundary conditions are open at the top and line-tied at the bottom, representing the denser plasma in the convection zone beneath the simulation domain.

The total number of grid points used varies, and resolution is increased to check that the results converge. A typical run has a maximum resolution of 512^2 grid points. By stretching the vertical domain the cell size can be as low as 0.1 in regions where the magnetic flux tube is located and goes up to 0.5 at the top of the domain. By using

larger cells at the top of the domain the CFL condition for advection

$$\Delta t < \frac{\Delta x}{C_s} \tag{6.18}$$

can be kept reasonable even though the sound speed C_s increases with temperature towards the top of the simulation domain.

6.3 Evolution of the Magnetic Field in the Convection Zone and Photosphere

The flux tube is initially buoyant as there is a density deficit which is stronger in the centre of the tube. As a convectively unstable atmosphere will allow upward buoyant motions to continue, the tube should continue to rise until the stratification becomes sub-adiabatic, or drag forces have fragmented the tube.

Magara (2001) reasoned that if a flux tube's cross section remains constant during the rise, its evolution in this region can be modeled by a rigid cylinder rising in a gravitationally stratified layer. As a result the rise speed of the flux tube should increase linearly with time,

$$v_y = Mt \tag{6.19}$$

where M is a constant which depends on the initial set-up of the tube. Figure 6.3 shows the rise speeds at the centre of the tube as a function of time along with the theoretically calculated values. The tube is initially at rest but then its rise speed approaches the theoretical value. As the tube reaches the stable photosphere, its velocity begins to fall away from the theoretical value due to the stable stratification halting further motion.

Magnetic flux in the tube must be conserved, in this 2D situation this gives

$$B_a A = const \tag{6.20}$$

where A is the area of the cross-section of the tube. In addition mass must be conserved in the tube

$$\rho A = const \tag{6.21}$$

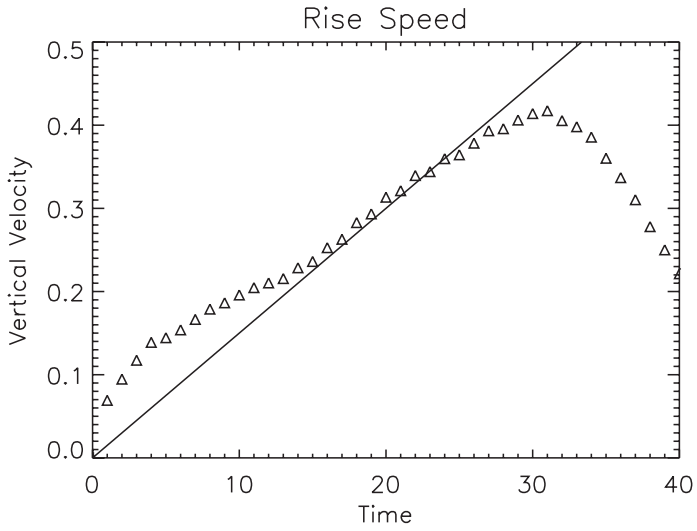

Figure 6.3: The rise speed at the centre of the flux tube (triangles) along with the theoretical linear evolution (solid line). Velocity is normalised to the Alfvén speed at the surface, and the time is normalised to $t_0 = H_p/v_A$.

which means that

$$\frac{B_a}{\rho} = const \tag{6.22}$$

Hence as the tube rises the axial field strength falls as

$$B_a(y) = B_a(y_0)\frac{\rho(y)}{\rho(y_0)} \tag{6.23}$$

where y_0 is the height of the tube initially. This means that the axial field strength will diminish as the tube gets further up the convection zone. Figure 6.4 shows the axial field strength B_a as a function of height through the centre of the horizontal domain at five different times in the rise of the flux tube. The field strength at the centre of the tube is proportional to the fall in density as the flux tube rises up the convection zone. At later times this proportionality falls away as the evolution of the flux tube becomes no longer determined by buoyancy.

The flux tube will only continue to rise as long as the stratification is superadiabatic. The photosphere is convectively stable (being almost isothermal), and this inhibits the buoyant rise of the flux tube. This can be seen in figure 6.3 which shows the rise speed fall at later times in the rise. This halt in the vertical motion of the flux

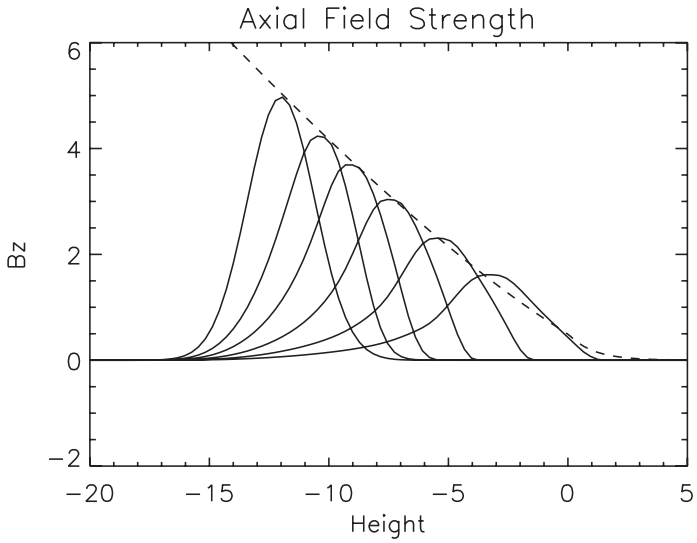

Figure 6.4: The axial field component though the centre of the tube as a function of position at five different times at t=0,10,20,30,40,50, shown by the solid lines in order from left to right. The dashed line shows the ratio of the density to the density at the tube's initial height.

tube causes it to expand more in the horizontal direction. This can be seen in figure 6.5 which shows the magnetic pressure at four different times in the simulation. The initially circular cross-section is now flattened out to form a magnetic layer at the surface, and no further rise due to buoyancy occurs.

This horizontal layer forms a contact surface with the plasma above. This layer is effectively holding up denser plasma due to magnetic buoyancy, as can be seen in figure 6.6. This magnetic layer, which is holding up denser gas, is unstable to an instability similar to the Rayleigh-Taylor instability, where the destabilising effect is the gradient in the magnetic field. This instability is commonly referred to as the Parker instability or a mixed mode of the magnetic-buoyancy instability, or MBI (Archontis et al., 2004; Newcomb, 1961; Thomas and Nye, 1975; Acheson, 1979).

Criteria for the onset of this instability for a magnetic field in an isothermal adiabatic atmosphere has previously been derived (Newcomb, 1961; Gilman, 1970; Acheson, 1979; Parker, 1979). The criteria for onset of the magnetic buoyancy instability can be regarded as a competition between the destabilising effect of the gradient in the

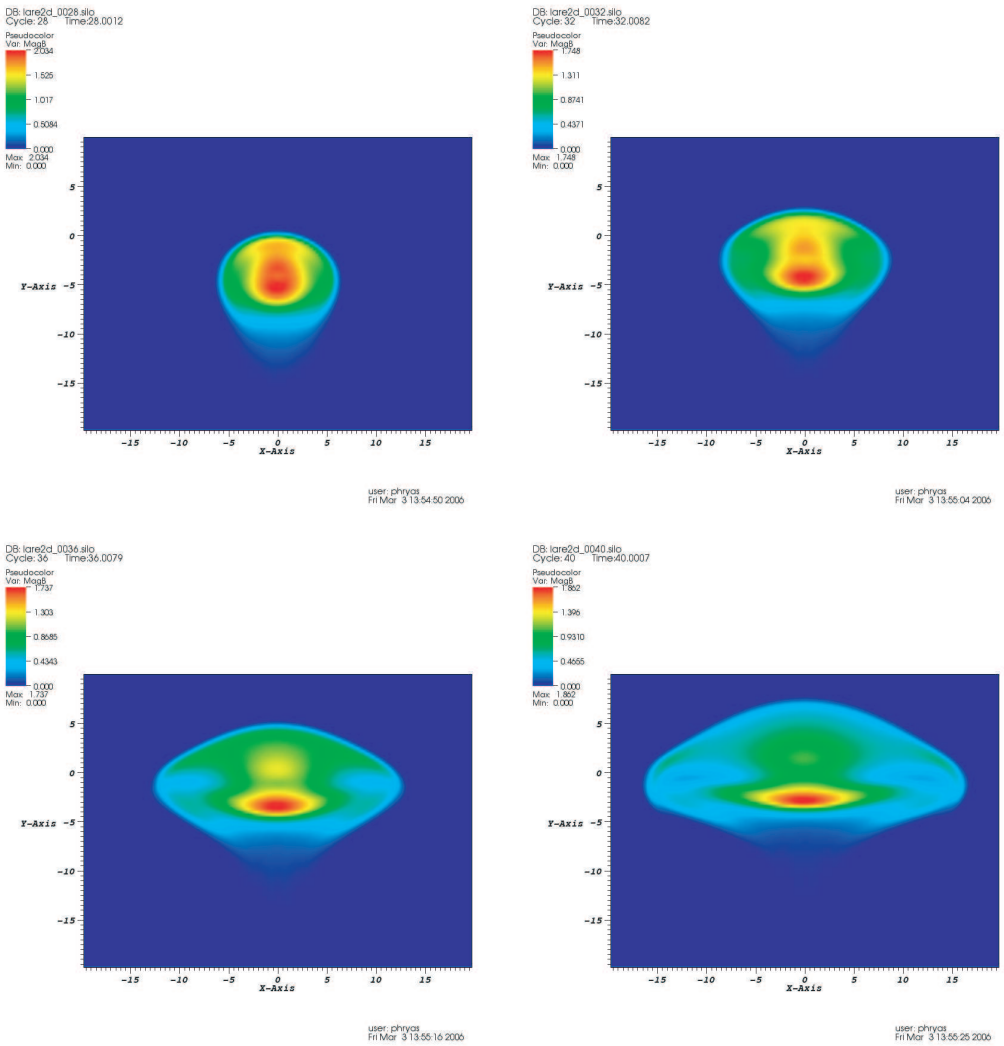

Figure 6.5: The magnetic pressure at 4 different times in the simulations. Top left:t=28, top right:t=32, bottom left:t=36, bottom right:t=40.

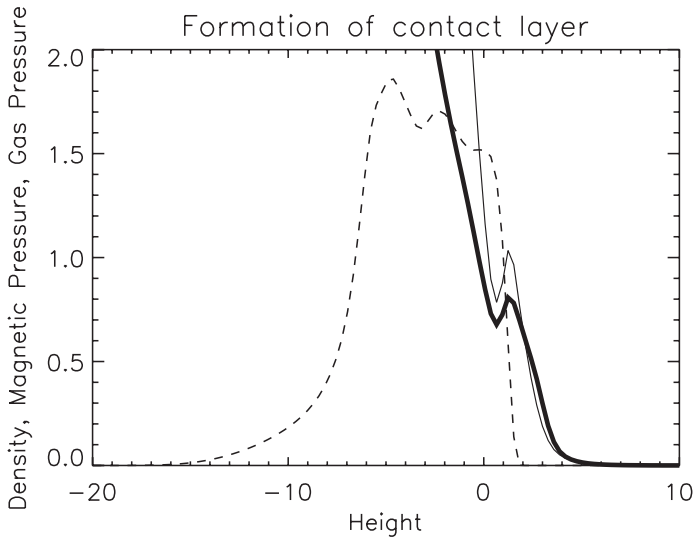

Figure 6.6: The magnetic pressure (dashed line), gas pressure (thin solid line) and density (thick solid line) as functions of height in the centre of the horizontal domain at time t=30. The density is depleted at the top of the layer, and consequently the magnetic field is holding up denser gas.

magnetic field and the stabilising effect of the convectively stable temperature gradient.

For modes that do not twist field lines the criteria for onset is given by

$$-\frac{g}{\gamma {C_s}^2}\frac{d}{dy}ln\left(\frac{B}{\rho}\right) > \frac{N^2}{{C_A}^2}. \tag{6.24}$$

Modes that do twist the field lines are more easily generated (Acheson, 1979) and the criteria for onset is given by

$$-\frac{g}{\gamma {C_s}^2}\frac{d}{dy}ln(B) > k^2\left(1+\frac{l^2}{n^2}\right)+\frac{N^2}{{C_A}^2}. \tag{6.25}$$

Here B is the magnetic field strength, ρ the density, γ the ratio of specific heats, C_s the sound speed, C_A the Alfvén speed. N is the Brunt-Wäisälä frequency which can be written as

$$N^2 = \frac{g}{\gamma}\frac{d}{dz}ln\left(p\rho^{-\gamma}\right) \tag{6.26}$$

which is equivalent to the definition given in (1.7). k is the wave number in the x direction (along the field), l is the wave number normal to the field in the horizontal direction and n is the wave number in the vertical direction. The perturbations are

assumed to be of the form

$$\sin(lz)\exp(i(kx+ny-\omega t)). \tag{6.27}$$

Criteria (6.25) can be rewritten as (Archontis et al., 2004)

$$-H_p\frac{d}{dy}ln(B) > k^2\left(1+\frac{l^2}{n^2}\right)-\frac{\gamma}{2}\beta\delta \tag{6.28}$$

where H_P is the local scale height and δ is called the super-adiabatic excess, which is the difference between the logarithmic temperature gradient and the adiabatic value and is always negative in the solar atmosphere (Stix, 2002).

In order for the mixed mode of the MBI to develop the destabilising effect of the presence of magnetic field holding up dense plasma, represented by the LHS in (6.28), must outweigh the stabilising term on the RHS. The stabilising term, which depends on δ and the plasma β, prevents further rise of magnetic field above the contact layer. However, after the upper part of the flux tube forms the horizontal magnetic layer at the base of the photosphere, more and more flux from the bottom of the tube is pushed up below it, as the buoyantly unstable convection zone is still pushing the lower part of the tube upwards. As more flux rises, the local plasma β decreases and the effect of the stabilising term in (6.28) becomes less and less important. There reaches a stage when the local β is sufficiently small so that the dominant term is the destabilising term. When this happens any perturbations in the magnetic layer will grow exponentially as the instability develops.

6.4 The Effect of Heating in the Lower Atmosphere

As mentioned in chapter 3 there are various heating mechanisms in the solar atmosphere that cannot be included directly in the simulations of the solar atmosphere, and some are not specifically known, such as the coronal heating term. Rather than attempt to simulate theses heating mechanisms directly, it is easier to model them. The effect of these heating mechanisms is to give the observed temperature profiles in the quiet Sun. In chapter 4 a simple ad-hoc model was introduced which models these effects using a Newton-cooling approach. An extra term for the time variation of the specific internal

energy density was then included which causes the local value of the plasma temperature to relax to the value it had initially. The mechanisms are modeled to be more effective in the denser photosphere and negligible in the corona.

The effect of this heating on simulations of flux emergence is now investigated. These effects are investigated separately from the effects of partial ionisation, which are investigated in the following section.

The previous section shows how the magnetic buoyancy instability can occur when a flux tube is halted at the convectively stable photosphere and spreads horizontally to form a magnetic layer holding up denser plasma. With this expansion comes an associated cooling, related to the $P\nabla.\mathbf{v}$ in the energy equation (6.17). If the effects of the extra heating mechanisms in the photosphere are not included, then the flux tube cools (assuming the magnetic Reynolds number is high and Joule heating is negligible) and produces temperatures in the magnetic layer well below anything observed on the Sun (Archontis et al., 2004). Indeed for the simulations shown so far this is indeed what happens. Dense matter is brought up in the flux tube and cools to very low temperatures, due to the lack of heating mechanisms present in the model. Figure 6.7 shows the temperature and density as a function of height in the centre of the horizontal domain for a typical simulation.

The inclusion of the Newton cooling term

$$\frac{D\epsilon}{Dt} = ... - \frac{\epsilon - \epsilon_0(\rho)}{\tau} \tag{6.29}$$

representing the combined effect of all the extra heating mechanisms, should reduce this unrealistic cooling. By comparing simulations with and without this additional term, this can be verified. If the timescale for the modeled heating mechanisms is quicker than the timescale of the adiabatic cooling associated with the expansion, then the dense matter brought up in the flux tube should remain at photospheric temperatures. The timescale τ is made to depend on density via

$$\tau(\rho) = \rho^{-\alpha}. \tag{6.30}$$

In this way the term is negligible in the sparse corona but most effective in the lower atmosphere. Figures 6.8 and 6.9 show the final temperature and density for three

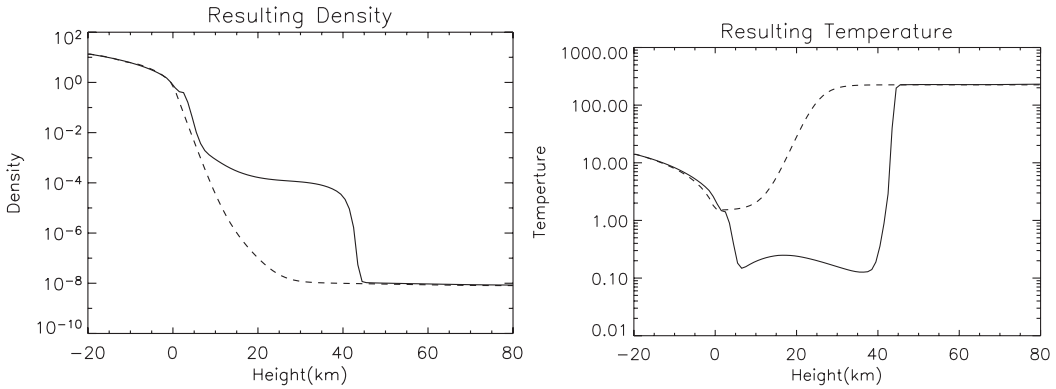

Figure 6.7: Left panel: The initial (dashed line) and final (solid line) density as a function of height in the centre of the horizontal domain, for the adiabatic case where no heating/cooling terms are included. Right panel: The initial (dashed line) and final (solid line) temperature as functions of height for the same simulation. All values are normalised to values at the photosphere.

different simulations. The first is with $\alpha = \infty$ (no Newton-cooling), the second is when the Newton-cooling term is implemented with a timescale power law of $\alpha = 1.67$, and the third is when $\alpha = 1$.

As can be seen, dense matter is still emerging into the atmosphere, but now this matter is not being cooled to sub-photospheric temperatures, but remains at photospheric temperatures.

As well as affecting the temperature of emerging plasma, the inclusion of heating mechanisms in the atmosphere will also affect the instability which forces magnetic field from the photosphere into the corona. The simple interchange derivation for the onset of the magnetic buoyancy instability (Newcomb, 1961; Gilman, 1970; Acheson, 1979; Parker, 1979) assumes that as a parcel of gas moves upwards into its new surroundings, the motion is adiabatic and no heat transfer occurs. However by attempting to simulate the effects of various non-adiabatic terms in the energy equation the criteria for the instability to occur must be modified. Gilman (1970) applied the same argument as Acheson (1979) but instead of assuming adiabatic motion, the displaced parcels of gas instantaneously acquire the temperature of their new surroundings (this corresponds to the thermal conductivity being infinite). The criteria for the onset of the magnetic

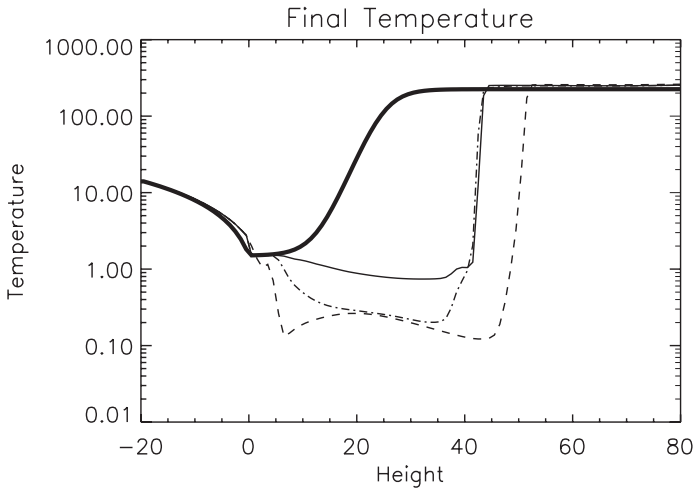

Figure 6.8: The temperature in the centre of the domain as a function of height for t=0 (thick solid line). Also shown are the final temperature profiles for the case when $\alpha = \infty$ (dashed line), for $\alpha = 1.67$ (dot-dashed line) and $\alpha = 1$ (thin solid line).

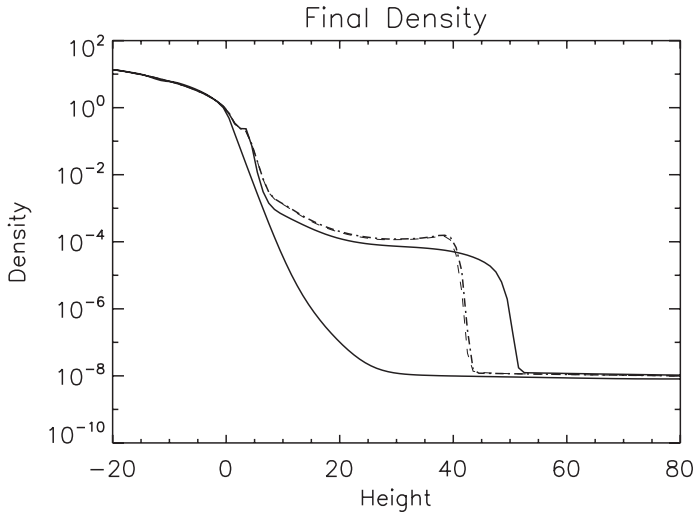

Figure 6.9: The density in the centre of the domain as a function of height for t=0 (lower solid line). Also shown are the final density profiles for the case when $\alpha = \infty$ (upper solid line), for $\alpha = 1.67$ (dot-dashed line) and $\alpha = 1$ (dashed line).

buoyancy instability for modes that twist field lines is then

$$-\frac{g}{\gamma {C_s}^2}\frac{d}{dy}\ln(B) > k^2\left(1+\frac{l^2}{n^2}\right). \tag{6.31}$$

It can be seen by comparison with equation (6.25) that the stabilising effect of the convectively stable gradient of the photosphere has been destroyed by this instantaneous heat transfer.

In these simulations, although the heat transfer is not instantaneous, there is heat transfer on a finite time-scale, represented by the relaxation term for the energy (see equation (6.17)). So it is expected that with the heat transfer present in these simulations the stabilising term in the criteria for stability (6.25) will be reduced by some amount, just as for instantaneous transfer the stabilising term is negligible. So the onset of the magnetic buoyancy instability should occur earlier in the simulation than in the adiabatic case. This is because less magnetic field is needed to decrease the effect of the competing stabilising term, which is now less important.

The magnetic field in the centre of the unstable magnetic layer bends upwards and flux is forced into the atmosphere above. Thus to measure the growth of the instability the vertical velocity at the centre of the domain just above the magnetic layer at a height of 10 (1500 km) is plotted as a function of time. Figure 6.10 shows these plots for both the adiabatic case and the non-adiabatic case. As can be seen the non-adiabatic atmosphere allows onset of the instability much earlier in the simulation. This is because less magnetic field has to build up to nullify the stabilising term in equation (6.25). The growth rates are also different, the one for the non-adiabatic case being larger. The instability quenches earlier for the non-adiabatic case. The magnetic field is emerging at a greater rate than the adiabatic situation and so the velocities at this height will decrease quicker to background values as the instability quenches.

6.5 The Effect of Partial Ionisation

It has been shown how magnetic field can emerge from the photosphere, where its buoyant rise has been stopped by stable stratification, into the corona, via the magnetic

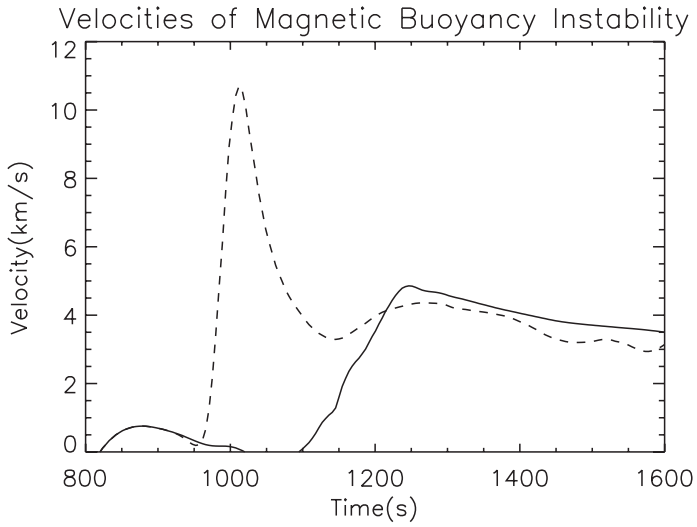

Figure 6.10: Plasma velocity at a height of 1500 km above the surface as a function of time showing the onset of the magnetic buoyancy instability. The solid line is the adiabatic case and the dashed line is the case non-adiabatic case.

buoyancy instability. It has also been shown how heating/cooling effects in the lower atmosphere can affect the onset and development of this instability.

The effect of partial ionisation is now investigated by comparing results from two simulations, one where the atmosphere is modeled as a fully ionised plasma (FIP), and one where it is modeled as a partially ionised plasma (PIP), with the ionisation level ξ_n and Cowling resistivity η_c calculated locally as functions of density and temperature, using the methods described in previous chapters.

In a partially ionised plasma, the dissipation of currents is anisotropic, where cross-field currents are dissipated by η_c, and field-aligned currents are dissipated by η. Using the equations for η, in these simulations the value of η never exceeds the numerical round-off value in the code, and so all simulations are run with $\eta = 0$. The value of η_c depends on local density, temperature, ionisation level and magnetic field strength and is calculated at each time step in the simulations.

As magnetic field emerges through the partially ionised atmosphere, η_c will vary. If this value gets high enough so that the local magnetic Reynolds number, R_m, is less than unity then the evolution of the magnetic field will be diffusion dominated. This

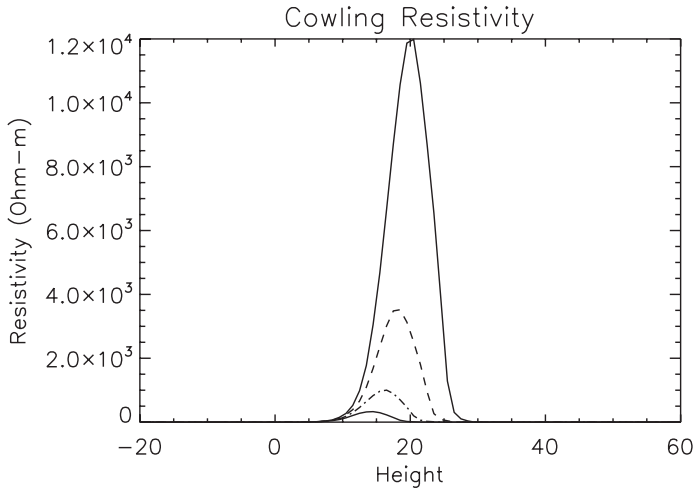

Figure 6.11: The value of η_c in Ωm as a function of height in the centre of the horizontal domain at times t=40 (lower solid line), t=44 (dot-dash line), t=48 (dash line) and t=52 (upper solid line). The height is normalised to the scale height at the surface.

is in contrast to the fully ionised case, where $\eta = 0$ and the evolution is dominated by advection. This difference in the evolution of magnetic field as it emerges though the atmosphere may effect the rate of emergence of magnetic flux into the corona.

Moreover, the anisotropy in the dissipation of currents in a partially ionised atmosphere will affect the currents that emerge with the field. If η_c becomes large enough, then this anisotropy becomes important because cross-field currents will be preferentially dissipated as opposed to field aligned currents. This may have important consequences for the nature of the magnetic field that forms in the corona.

6.5.1 Emergence of Magnetic Flux

As the buoyancy instability develops, magnetic field emerges from the photosphere into the chromosphere. In chapter 5, it was shown that given varying magnetic field strengths, perpendicular dissipation of currents was most prominent in chromospheric plasma. Figure 6.11 shows the value of η_c as a function of height, calculated in the centre of the horizontal domain, for different times in the simulation, as magnetic field emerges into the partially ionised atmosphere.

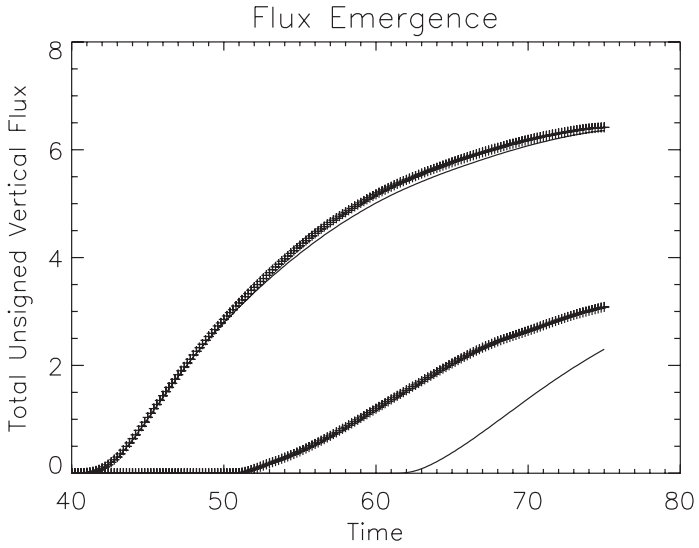

Figure 6.12: Total unsigned flux at two different heights as a function of time in the simulation. The two left plots are at heights 1500km, and the two right plots are at 4500 km above the surface. The solid lines are for the FIP model and the crosses are for the PIP model.

The values of the magnetic Reynold's number for these values of η_c reach a minimum of 0.01-0.1. Thus figure 6.11 represents a region of approximately 10 photospheric scale heights (1500 km) in extent where the evolution of the magnetic field is dominated not by advection but by diffusion.

As magnetic field emerges through the atmosphere, the presence of a diffusive layer will affect the rate of emergence, as the time-scale for diffusion will be much smaller than that for advection.

By comparing the amount of flux emerging through various heights of the atmosphere for the two models, the importance of this diffusive layer can be evaluated. This is done using the amount of unsigned vertical flux

$$\Phi = \int |B_y| dx \tag{6.32}$$

where the integral is over the horizontal extent of the domain. Figure 6.12 shows the total flux emerging at two different heights for the two models, as a function of time. The lower height is $y = 10$ (1500km), which corresponds to a height where $\eta_c = 0$

for both the PIP and FIP models. The upper height is $y = 30$ (4500 km), above the diffusive layer. At the lower height the flux emerging for the FIP model and the PIP model are almost identical, as at this height $\eta_c = \eta = 0$. At 4500 km the flux emerging is greatly increased by the presence of the diffusive layer in the PIP model compared to the FIP model. As the magnetic field passes through this layer it is diffused on a time-scale

$$t_d = \frac{L^2 \mu_0}{\eta_c} \tag{6.33}$$

where L is the vertical extent of the region. The profile of η_c is changing during the simulation as the plasma variables change. Using the maximum values of η_c in these simulations gives a diffusive time-scale of $t_d \approx 5s$ which compares to the local transit time of flux across this region of $t_t \approx 500s$. Hence the magnetic field takes many diffusive time-steps to transit the partially ionised layer. Hence, locally, the magnetic Reynolds number (using η_c rather than η) is well below unity, even though the majority of the computational domain is high Reynolds number.

The amount of magnetic flux has been greatly increased by considering the partial ionisation in the solar atmosphere. It follows that the resultant structure will be different. Figure 6.13 shows isocontours of the total magnetic field strength at t=75 for the two models. Clearly the resultant field is stronger higher up in the partially ionised model due to the diffusion caused in the partially ionised region. This can be seen more clearly in figures 6.14 and 6.15. Figure 6.14 shows a slice of these isocontours along the centre of the horizontal domain. Figure 6.15 shows 2D field-lines in x and y for the two different models. The field-lines are given by the contours in A_z where $\mathbf{B} = \nabla \wedge \mathbf{A}$.

As can be seen from figures 6.13-6.15, the magnetic field in the PIP model is much more diffuse, as it's evolution has been dominated by diffusion as it emerged through the partially ionised atmosphere. As a result, the field-lines extend further into the corona, and more flux emerges in the upper atmosphere.

6.5.2 Cross-Field and Field-Aligned Currents

Observations of magnetic fields in the solar atmosphere suggest that the solar corona is predominantly force-free (Georgoulis and LaBonte, 2004). The low β plasma of the solar

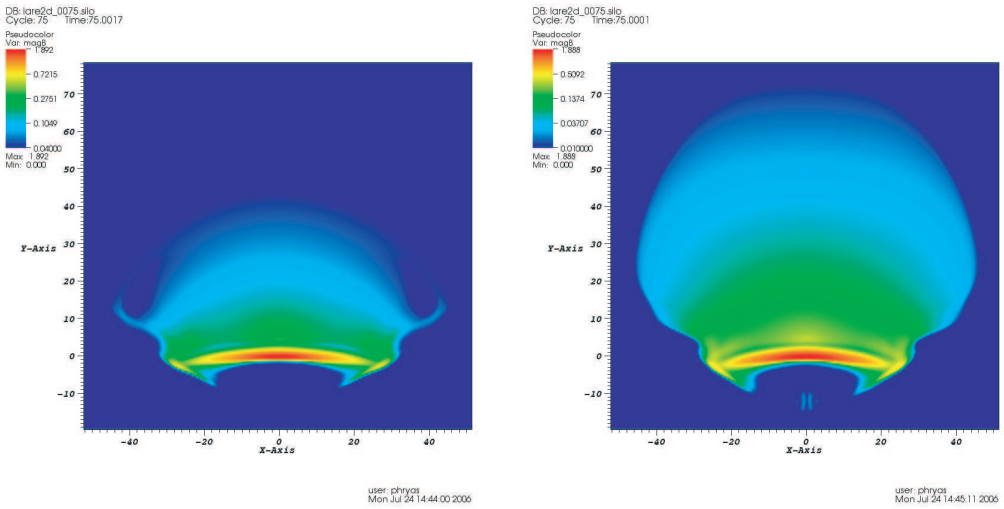

Figure 6.13: Magnetic field strength at t=75 for the fully ionised model (left panel) and partially ionised model (right panel).

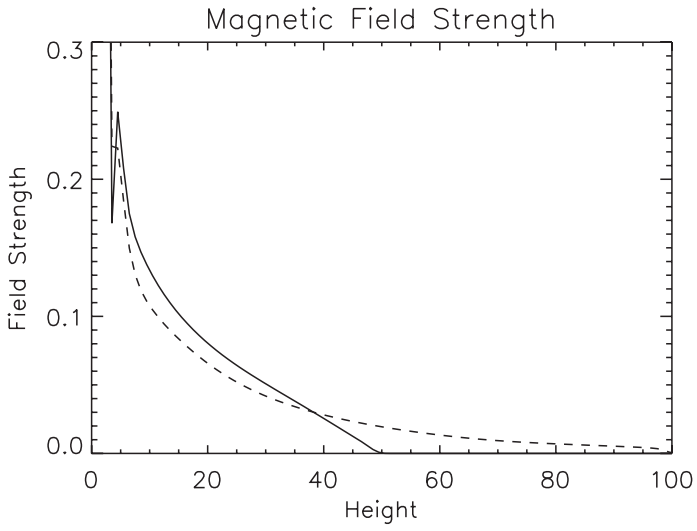

Figure 6.14: Magnetic field strength in the centre of the domain at t=75 for the fully ionised model (solid line) and partially ionised model (dashed line).

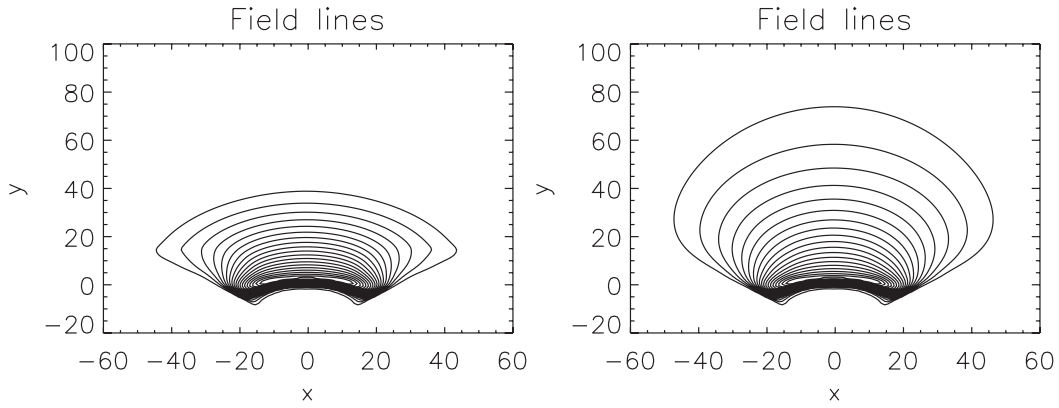

Figure 6.15: Field-lines in x and y given by contours in A_z where $\mathbf{B} = \nabla \wedge \mathbf{A}$. The left panel is the FIP model, the right is the PIP model. Both plots use the same contour levels.

corona is magnetically dominated, and the pressure and gravity terms in the momentum equation are small in comparison to the Lorentz force. The equilibrium equation is given simply by

$$\mathbf{j} \wedge \mathbf{B} = 0. \tag{6.34}$$

This is equivalent to saying that the current is aligned with the magnetic field $\mathbf{j} \parallel \mathbf{B}$, or that there are no cross-field currents, $\mathbf{j}_\perp = 0$.

Beneath the surface the plasma β becomes greater than unity, and therefore pressure forces dominate magnetic forces. The field in this region cannot be assumed to be force-free.

If active regions are the product of emerging sub-surface field as evidence suggests (Zwann (1978)), then the force-free coronal field must be formed from non force-free fields. This raises an important question. How is the magnetic field of sub-surface flux tubes converted into force-free magnetic coronal field?

For a partially ionised plasma, the current is not diffused isotropically. The Coulomb resistivity η acts parallel to the field, and η_c acts perpendicular to it. However, it has been shown that for the solar chromosphere η_c/η can be orders of magnitude. In fact η is less than numerical round-off and $\eta = 0$ is used in these simulations. This means that as the magnetic field emerges through the partially ionised region of the

model atmosphere, the only component of the current to be diffused directly is the cross-field current.

This gives a mechanism for the formation of force-free current during flux emergence. As magnetic field is driven though the partially ionised layer by the magnetic buoyancy instability, the energy of cross-field currents are dissipated by the ion-neutral interactions, while the field-aligned currents are not directly affected. Hence if the value of η_c is large enough the field that emerges through the partially ionised region will have no cross-field currents and will therefore be force-free.

By comparing the amount of cross-field current emerging into the corona for the two models, the efficiency of this mechanism in forming force-free currents can be investigated. A measurement of the amount of cross-field current is obtained by performing the integral

$$J_\perp(y) = \int |\mathbf{j}_\perp(x,y)|\, dx, \tag{6.35}$$

over the horizontal extent of the domain. The same can be done for the parallel current,

$$J_\parallel(y) = \int \left|\mathbf{j}_\parallel(x,y)\right| dx. \tag{6.36}$$

Figure 6.16 shows these as a function of height for the initial magnetic field profile representing the magnetic flux tube in the convection zone. As can be seen the magnitude of the perpendicular and parallel currents is comparable.

After magnetic field has emerged into the corona, the same calculation can be performed on the final magnetic field profile. Figure 6.17 shows the total perpendicular current magnitude $J_\perp$ as a function of height at t=75, for both the fully ionised model and the partially ionised model. Figure 6.18 shows the same for the total parallel current magnitude $J_\parallel$.

As can be seen from figures 6.17 and 6.18, when the atmosphere is partially ionised, even though magnetic field is emerging into the corona, currents perpendicular to the field are not emerging. However, when the atmosphere is fully ionised, perpendicular current is allowed to emerge with the field. The presence of neutrals in the partially ionised model causes dissipation of perpendicular currents before they can emerge into the corona.

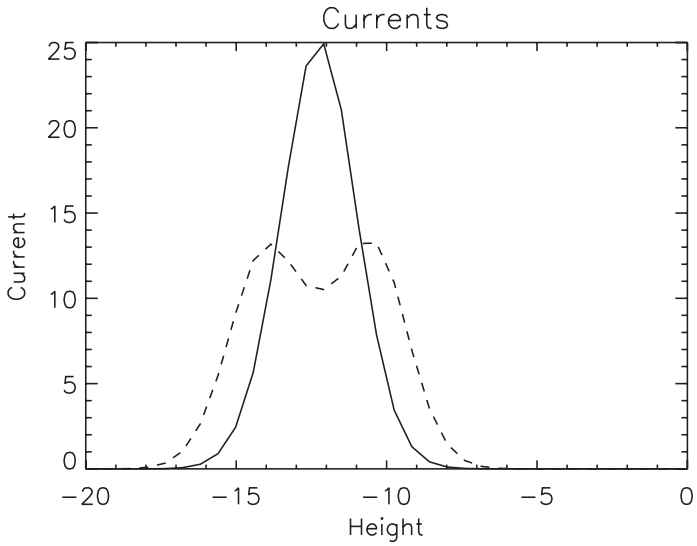

Figure 6.16: Total perpendicular (dashed line) and parallel current (solid line) integrated across the horizontal domain as a function of height for the initial flux tube configuration All values are normalised.

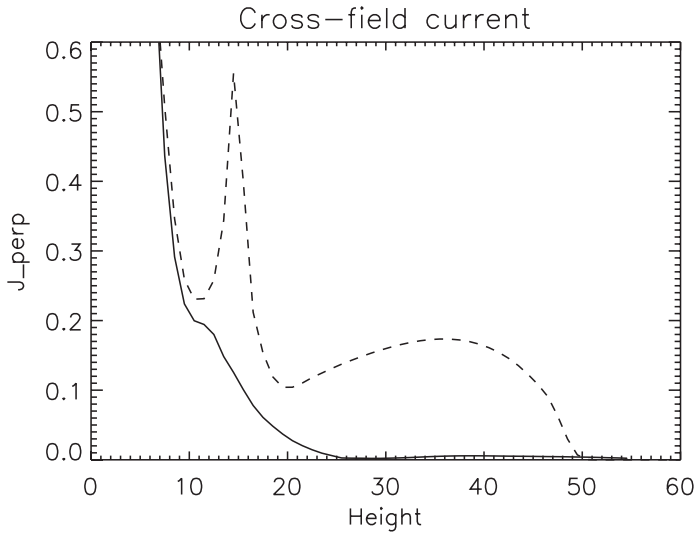

Figure 6.17: Total perpendicular current across the domain as a function of height for the FIP model (dashed line) and the PIP model (solid line). All values are given in normalised units.

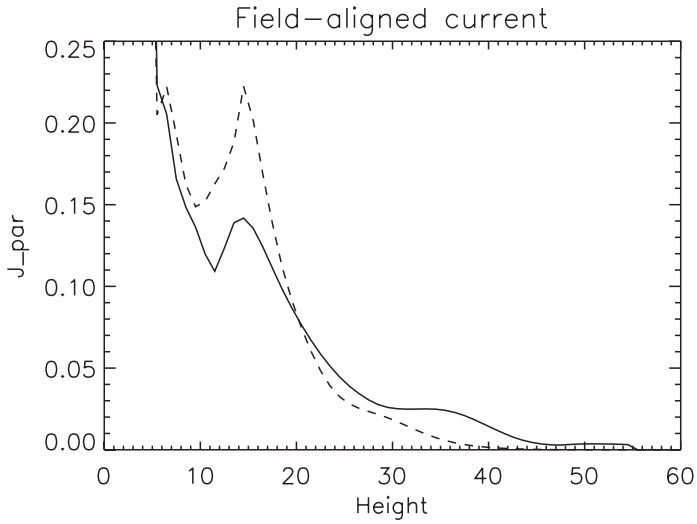

Figure 6.18: Total parallel current across the domain as a function of height for the FIP model (dashed line) and the PIP model (solid line). All values are given in normalised units.

Although $\eta = 0$ in both models, there is a difference in $J_{\parallel}(y)$ in figure 6.18. The equations for the evolution of $\mathbf{j}_{\parallel}$ and $\mathbf{j}_{\perp}$ are coupled to each other, and as the two models have different values of η_c, it is expected that the amount of $\mathbf{j}_{\parallel}$ emerging will differ slightly between the two models.

Evidently, the presence of a partially ionised region in the solar atmosphere has destroyed the cross-field current but allowed similar amounts of field-aligned current to emerge as in the case for a fully ionised plasma. Hence the field has been converted from a general configuration to one approaching a force-free state. The ion-neutral collisional dissipation has given a direct mechanism for the formation of force-free magnetic field in the corona.

Calculations of the force-free nature of atmospheric magnetic field have been made based on observations using the Michelson Doppler Imager (MDI) on the SOHO spacecraft (Georgoulis and LaBonte, 2004), (Metcalf et al., 1995) where vector magnetograms were extrapolated to reconstruct the coronal field. Estimates of the height at which the field becomes force-free are typically 400-1000 km (y=3-6) above the photosphere. A typical height for these simulations based on figure 6.17 is much larger

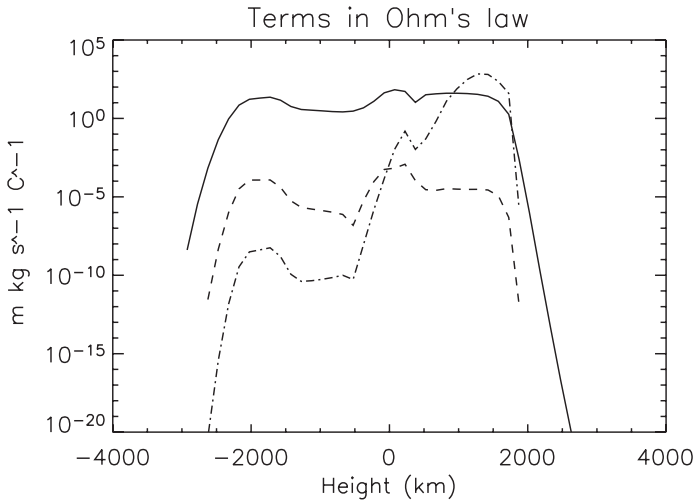

Figure 6.19: Vertical profile of estimates of the terms in Ohm's law in the centre of the horizontal domain at t=75. The solid line is the advection term, the dashed line is the Hall term, and the dash-dot line is the diffusive term due to ion-neutral collisions.

than this, around 3000 km (y=20). This discrepancy may lie in the 2D nature of the simulations, and further 3D work will be performed to better diagnose the height at which field becomes force-free. However, these results show that in 2D at least, the emerging field is not force-free unless the partially ionised regions of the atmosphere are included in the models.

Throughout these simulations the Hall term has been neglected from Ohm's law. Figure 6.19 shows the magnitudes of the Hall term ($|\frac{\mathbf{j}\wedge\mathbf{B}}{en_e}|$), the advection term ($|\mathbf{v}\wedge\mathbf{B}|$) and the diffusive term for ion-neutral collisions ($|\eta_c\mathbf{j}_\perp|$), as functions of height at the centre of the horizontal domain for a simulation run at t=75. These plots represent typical values for the entire domain. The Hall term is always orders of magnitude lower than the advection term. Figure (6.19) also shows that the magnetic Reynolds number for the partially ionised plasma can reach values less than unity, as previous calculations in chapter 3 have inferred.

6.6 Conclusions

2D simulations of the emergence of magnetic flux into the solar atmosphere have been performed. The standard model used was that of a weakly twisted flux tube inserted into a model convection zone. The atmosphere of the Sun was modeled by two isothermal layers, representing the photoshere/chromosphere and corona, separated by a transition region. The flux tube evolution was initiated by dropping the density inside to start a buoyant rise to the surface. The resultant evolution agrees with previous work of flux tubes in the convection zone (Magara and Longcope, 2003; Fan, 2001).

Having briefly investigated the emergence mechanism, the effects of heating and cooling mechanisms in the solar atmosphere were added to the model. Rather than simulate these effects (such as radiative heating, thermal conduction and shock heating) directly, a simple approach was used to model there effects. Direct simulation of these effects is difficult in large scale models, and as already stated, not all heating mechanisms are known well enough to simulate directly. The combination of these mechanisms, both known and unknown, give the temperature observed through emission lines (Vernazza et al., 1981). Thus, a simple ad-hoc approach to modeling these effects is to relax the temperature to these observed values, or in the case of these simulations, the initial model temperature profile. This was done using a Newton-cooling term in the equations.

By modeling these heating/cooling terms, it was shown that the criteria for the onset of the magnetic buoyancy instability was modified. The onset of the instability, which drives flux into the corona, occurred earlier. Also the resultant rate of expansion of magnetic field into the corona was greater for this new model, and the reaction of the plasmas to the expansion was much more realistic. In the adiabatic case (no external heating/cooling present), there were no competing terms to the cooling of plasma from the $P\nabla.\mathbf{v}$ expansion. This lead to vastly lower temperatures of the photospheric plasma, which are not observed. By including heating/cooling mechanisms through this ad-hoc approach, the expansion of the plasma as the magnetic buoyancy instability developed did not lead to unrealistic cooling when dense plasma was brought up through the photosphere. The resultant temperature profile was more realistic for this new model.

The next set of simulations investigated the effect of the partially ionised regions

of the solar atmosphere on flux emergence. The relatively low temperatures (4×10^3K) mean that the fully ionised approximation used in standard MHD is not valid everywhere in the domain. The model was modified to include the effects of a partially ionised region. Assuming the solar atmosphere to be composed only of Hydrogen, ionisation levels and neutral fractions were calculated using the equations in chapter 3. The governing equations used were the single fluid equations derived in chapter 2.

For a partially ionised plasma the Coulomb resistivity η acts parallel to the magnetic field, and the Cowling resistivity η_c acts perpendicular to it. Using the model profiles for density and temperature, η and η_c were calculated locally, with η effectively zero throughout the simulations, and η_c being largest at chromospheric heights, depending on the local magnetic field strength.

The effect of partial ionisation was investigated by comparing the fully ionised plasma (FIP) and partially ionised plasma (PIP) models for the solar atmosphere. The region of high η_c in the partially ionised model represented a region dominated by dissipation, and as the magnetic field emerged through this region, the field became more diffuse than in the FIP model, where $\eta_c = 0$. The resultant field structure was more diffuse, with field lines extending further into the corona for the PIP model.

Coronal field is force-free, as the plasma is low β. However, field originating in the high β convection zone is not necessarily force-free. The main aim of this work is to find a mechanism for the conversion of non force-free sub-surface magnetic field into force-free coronal field. In the FIP model, substantial cross-field currents emerged into the corona. However, in the PIP model little to no cross-field currents emerged. Thus in the PIP model, the magnetic field emerges with no cross-field currents, i.e. force-free.

The presence of neutrals in the PIP model lead to a large resistivity perpendicular to the field, η_c, and so dissipated the cross-field currents as they emerged with the magnetic field. Conversely $\eta = 0$ in both models meant that similar amounts of field aligned current emerged.

It has been shown that the presence of neutrals is very important when investigating the nature of emerging magnetic fields. The ion-neutral collisions in the partially ionised plasma increased the resistivity perpendicular to the field. The dissipation of

cross-field currents by these ion-neutral collisions is a viable mechanism for the conversion of a generic magnetic field configuration to one approaching force-free.

The work presented here is a first attempt at simulating flux emergence through a partially ionised atmosphere. The initial stratification is an over-simplified model of the Sun, with no pre-existing convection beneath the surface. In addition these results are 2D simulations. To fully understand flux emergence it is necessary to work in 3D. The importance of shear forces and plasma drainage along field lines in a flux tube which is emerging into the atmosphere has already been shown to be important for flux emergence (Manchester, 2001; Manchester et al., 2004), as has the interaction with pre-existing coronal field (Archontis et al., 2004).

The next chapter will include simulations of flux emergence in 3D, in order to verify if this mechanism for the formation of force-free coronal field is relevant for the emergence of magnetic flux into the solar atmosphere.

Chapter 7

3D Simulations of Emerging Magnetic Flux

7.1 Introduction

The 2D model of emerging magnetic flux in the solar atmosphere fails to capture any phenomena that occur along the tube axis. However, emerging active regions are far from simple structures, as can be seen in so called δ-spots. δ-spots are active regions where the bipolar structure remains very compact during emergence, and rather than drift apart the two sunspots rotate about a common point. These active regions develop a large amount of magnetic shear, and the amount of twist is an important feature of the emerging magnetic field. It is for this reason that the kink instability has been suggested as a mechanism for the formation of δ-spot active regions (Linton et al., 1998, 1999; Fan et al., 1999). For these reasons the realistic modeling of flux emergence requires a full 3D approach.

Previous work on flux emergence has shown the importance of the 3D nature of emerging flux tubes (Fan, 2001; Magara and Longcope, 2001; Manchester, 2001; Magara and Longcope, 2003; Magara, 2004; Manchester et al., 2004; Gibson and Fan, 2006). The main feature of these simulations is the later expansion of magnetic flux into the atmosphere, which does not occur in 2D simulations. Plasma is able to drain down Ω-shaped tubes and allow further lifting of fieldlines. This has been suggested as

a way of getting the body of the flux tube into the atmosphere, rather than just the upper part, as was seen in chapter 6.

In this chapter 3D numerical simulations of flux emergence are carried out, based on the work done in chapter 6. The emergence of a magnetic flux tube from beneath the surface into the solar atmosphere is modeled. The effect of neutrals present in the weakly ionised plasma of the lower solar atmosphere is investigated. In particular the effect of ion-neutral collisions on the rate of flux emergence and the nature of the emerging fields.

7.2 3D Model

The background atmosphere is a 1D hydrostatic model with a temperature profile based on the observed values taken from the VALC model (Vernazza et al., 1981). z is now the vertical coordinate with x and y being horizontal co-ordinates. The temperature dependence on height is defined as in equation (6.2). As in previous simulations, the density and mean mass are found from solving the hydrostatic equation using the definition of pressure (see equations (6.4) and (6.5)). The resultant 1D stratification is exactly the same as in chapter 6 (see figure 6.2).

The initial magnetic field profile is given by a twisted flux tube, consisting of axial and azimuthal components (B_A and B_T respectively)

$$B_A = B_0 \exp\left(-\frac{r^2}{a^2}\right) \tag{7.1}$$

$$B_T = qrB_a \tag{7.2}$$

with the twist q defined by

$$q = \frac{B_a}{rB_T}, \tag{7.3}$$

a is the width of the tube and r is the radial distance from the centre of the tube. The tube is aligned along the x-axis. The choice of twist is more important in 3D simulations, as now the kink instability is allowed to develop if the tube becomes kink unstable. As mentioned in section 1.6, if a flux tube has too much twist it will become kink unstable as its radius increases during the rise and it cannot have survived the convection zone.

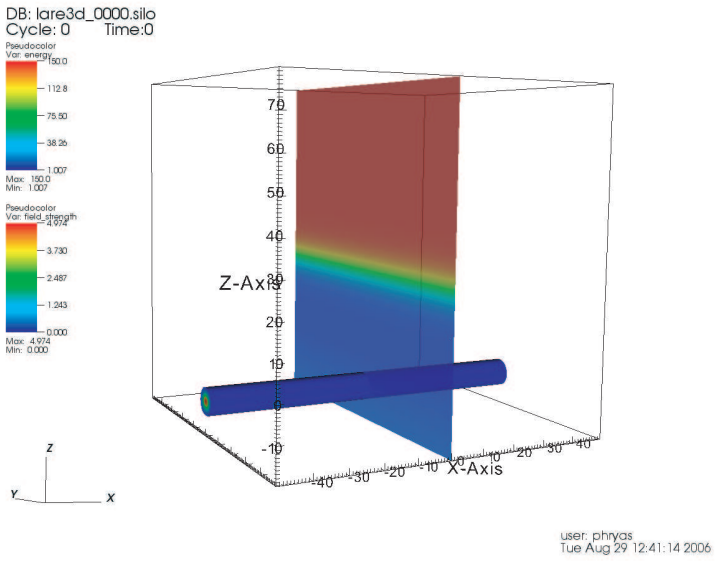

Figure 7.1: Isovolume of magnetic field strength showing the initial tube configuration. Also shown is a vertical slice of the initial temperature profile. All values are normalised to values at the surface.

For this reason the amount of twist given to the flux tube is the minimum required to avoid fragmentation in the convection zone

$$|q| = \frac{1}{a} \tag{7.4}$$

where a is the radius of the tube, and as in chapter 6, is set to 2. The initial magnetic field profile is shown in figure 7.1, along with the initial 1D temperature profile.

Again, a choice must be made as to how to initialise the rise of the flux tube in the convection zone. It is thought that flux tubes formed from the toroidal field in the tachocline remain connected to the large scale field by their roots (Zwann, 1978), while the apex of the tube rises to the surface, as shown in figure 1.10. As a result a flux tube which reaches the surface will be significantly 'bent' into an Ω-shape. In order to force the tube into this shape in these simulations, the centre is made buoyant while the ends are left in mechanical equilibrium. This is done by setting the pressure in the tube different to the field-free atmosphere ($p_0(z)$) by $p_1(r)$ where

$$\frac{dp_1(r)}{dr}\hat{\mathbf{e}_\mathbf{r}} = \mathbf{j} \wedge \mathbf{B}, \tag{7.5}$$

so that the pressure gradient matches the Lorentz force. The density in the tube differs from the field-free density ($\rho_0(z)$) by $\rho_1(r)$ where

$$\rho_1(r) = \frac{p_1}{p_0(z)}\rho_0(z)\exp\left(-\frac{x^2}{\lambda^2}\right) \tag{7.6}$$

In this way the centre of the tube, at $x = 0$, is buoyant while for $x > \lambda$ the tube is in mechanical equilibrium ($\rho_1 = 0$). The value of λ is chosen to be 20, as in Fan (2001).

The equations solved are the governing equations derived for the solar atmosphere

$$\frac{D\rho}{Dt} = -\rho\nabla.\mathbf{v} \tag{7.7}$$

$$\frac{D\mathbf{v}}{Dt} = -\frac{1}{\rho}\nabla P + \frac{1}{\rho}\mathbf{j}\wedge\mathbf{B} + \mathbf{g} + \nabla.\mathbf{S} \tag{7.8}$$

$$\frac{D\mathbf{B}}{Dt} = (\mathbf{B}.\nabla)\mathbf{v} - \mathbf{B}(\nabla.\mathbf{v}) - \nabla\wedge(\eta\mathbf{j}_\parallel) - \nabla\wedge(\eta_c\mathbf{j}_\perp) \tag{7.9}$$

$$\frac{D\epsilon}{Dt} = -\frac{P}{\rho}\nabla.\mathbf{v} + \frac{\eta}{\rho}{j_\parallel}^2 + \frac{\eta_c}{\rho}{j_\perp}^2 + \frac{1}{\rho}\Pi ij S_{ij} - \frac{\epsilon - \epsilon_0(\rho)}{\tau} \tag{7.10}$$

with the same definitions as in the 2D case. The variables are now dependent on all three spatial variables. These have been normalised to values at the photosphere.

$$\begin{aligned} r^* &= 150\,\mathrm{km} \\ \rho^* &= 2.7\times10^{-4}\,\mathrm{kg/m^3} \\ v^* &= 6515\,\mathrm{m/s} \\ t^* &= 23\,\mathrm{s} \\ T^* &= 6420\,\mathrm{K} \\ P^* &= 1.17\times10^{4}\,\mathrm{Pa} \\ B^* &= 1000\,\mathrm{G}. \end{aligned}$$

The computational domain extends from -20 to 80 (-3000 to 12000 km) in the vertical and -50 to 50 in both horizontal directions (-7500 to 7500 km). To help resolve the flux tube better the grid is stretched in the vertical direction so that there are more grid cells in regions of high $\mathbf{B}$. A typical value of dz at the centre of the flux tube is 0.1, rising to 0.5 at the top of the vertical domain. All results were tested for convergence by increasing the resolution. A typical maximum resolution simulation used 512^3 grid points.

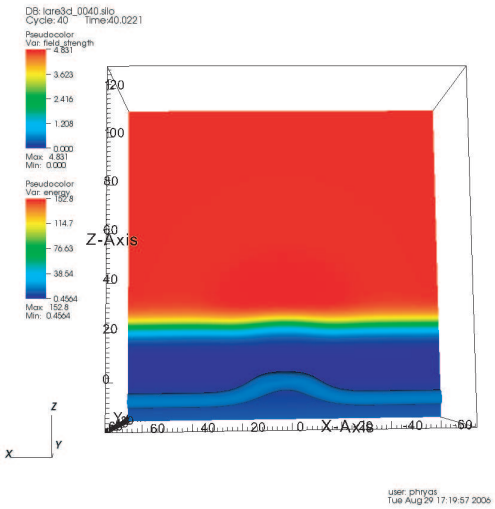

Figure 7.2: Isovolume of magnetic field strength at t=30 showing the Ω-shape formed due to the centre of the tube being more buoyant than the feet. Also shown is a 1D slice of the temperature.

7.3 Emergence of Magnetic Field into the Atmosphere

A flux tube which has enough twist to survive the convection zone should keep its cross section regular during the rise in the convection zone. Also the total magnetic flux should be conserved in the tube. The apex, being buoyant, rises and due to the super-adiabatic nature of the convection zone continues to rise until it meets the stable atmosphere (see figure 7.2). For a more rigorous treatment of the initial phase of a 3D flux tube in the convection zone see Archontis et al. (2004).

The tube apex continues to rise in the convection zone until it meets the convectively stable photosphere. Figure 7.3 shows simulated magnetograms at the surface As can be seen, the vertical component of the magnetic field forms a bipolar structure initially (t=40). As time proceeds, the bipoles separate as more of the flux tube emerges through the surface.

At this point in the evolution of the magnetic field, the vertical motion halts and a large amount of horizontal expansion can be seen. Figure 7.4 shows this expansion which occurs mainly in the x direction (along the tube axis).

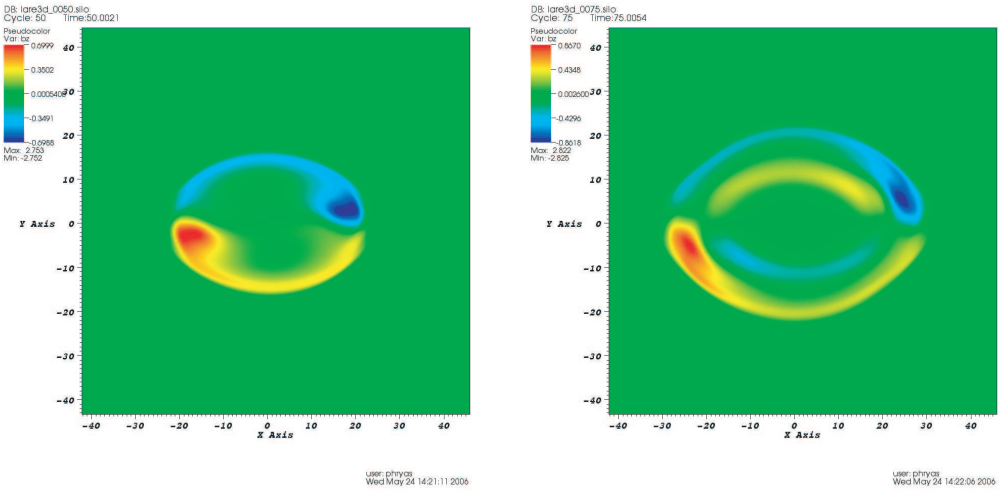

Figure 7.3: Simulated magnetograms of flux emergence, showing vertical magnetic field in the z=0 plane. The left panel is at t=40 and the right panel is at t=49. All values are normalised to non-dimensional units.

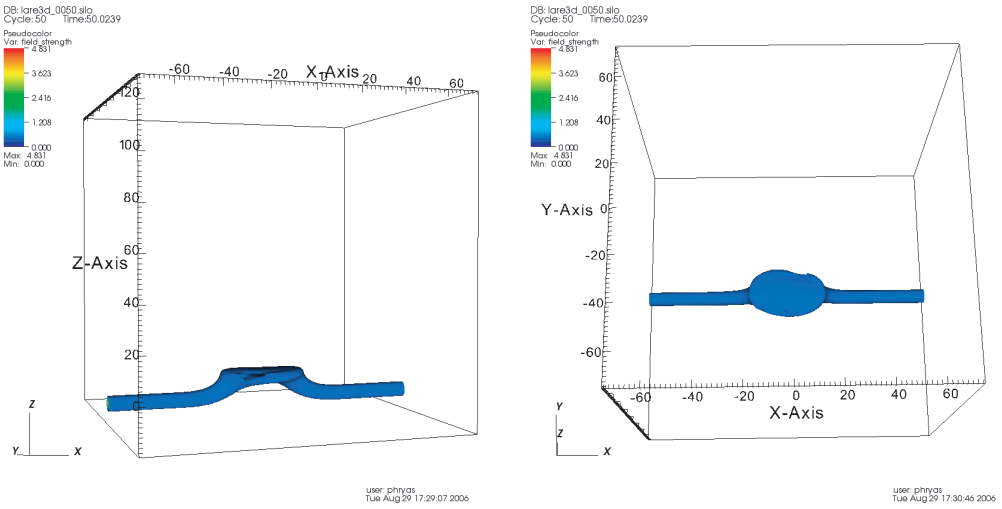

Figure 7.4: Isosurface of magnetic field strength at t=50, shown from two different angles. All values are normalised to values at the photosphere.

This horizontal expansion causes a 3D magnetic layer to be formed. The presence of magnetic field in this layer causes the density to be less due to total pressure balance. As a result the magnetic layer is holding up denser gas and is unstable to a mixed mode of the magnetic buoyancy instability.

As in the 2D case, the magnetic layer remains stable until enough flux is pushed up into the layer that the local plasma β becomes small enough that the destabilising effect of the magnetic field outweights the stabilising stratification (Archontis et al., 2004). Once this happens flux expands into the atmosphere above. This expansion can be seen in figure 7.5.

The expansion of the magnetic field into the atmosphere can cause velocity shear to build up. As the top part of the tube expands into the corona, the rest of the tube remains compact at the photosphere (figure 7.5). This causes a large vertical gradient in the magnetic field, in particular the axial field. Manchester (2001) suggested that this vertical gradient could lead to a velocity shear about the apex of the tube, caused by the Lorentz force being negative on the left side of the tube apex and positive on the right side. This shear can lead to plasma draining down the field line. Figure 7.6 shows the velocity along the tube axis at different times in the simulation. To the left of the apex it is negative and to the right it is positive, which shows that plasma is indeed capable of draining from the apex. This reduces the amount of mass at the apex and helps further expansion into the atmosphere.

7.4 The Effect of Partial Ionisation

The effect of partial ionisation is investigated by comparing results from two sets of simulations. The first is using the fully ionised plasma model (FIP) where $\xi_n = 0$ and $\eta_c = 0$. The second is the partially ionised plasma model (PIP) when the ionisation level ξ_n is calculated as a function of temperature, and the Cowling resistivity calculated locally as a function of temperature, density and magnetic field strength. As in the 2D case, the Coulomb resistivity η, which depends on electron collisions with both neutrals and ions, is negligible and all simulations are run with $\eta = 0$.

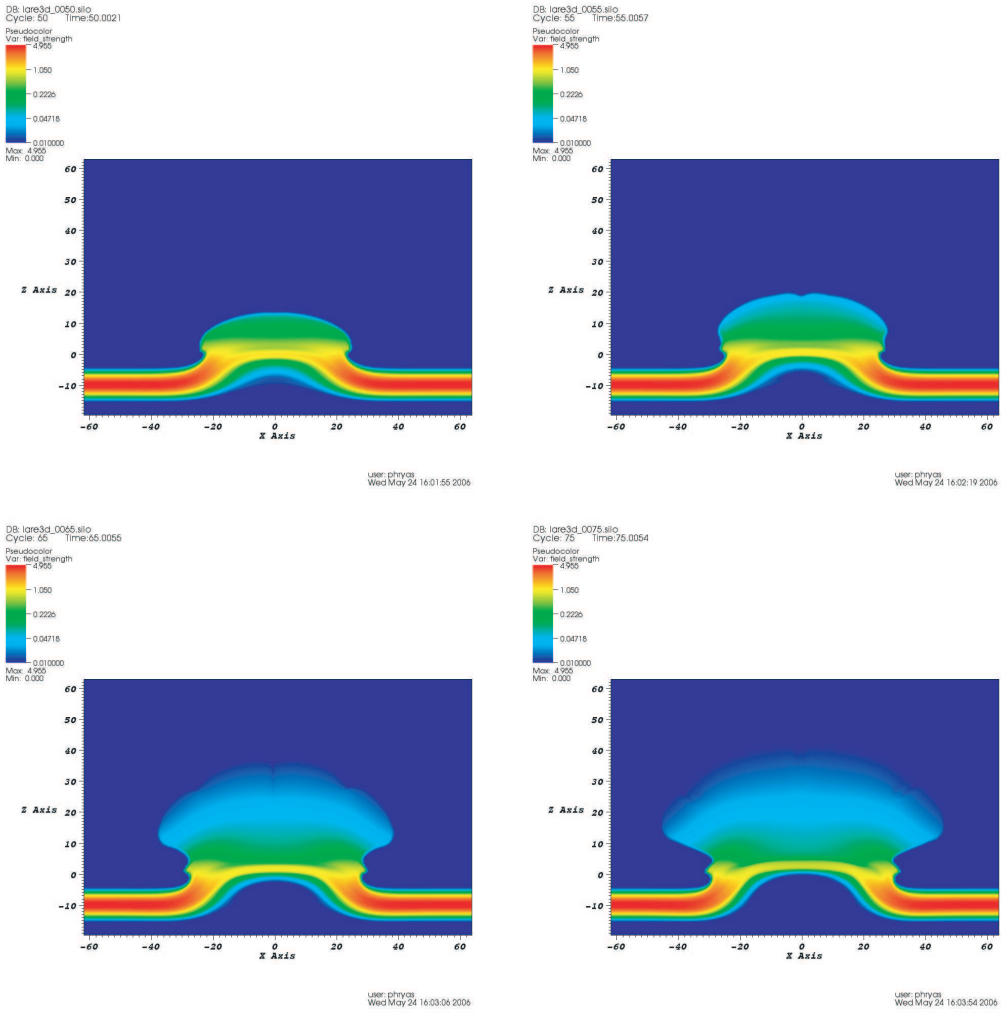

Figure 7.5: Isosurface of the magnetic field strength in the y=0 plane showing the expansion of the top of the flux tube into the model corona. Top left panel is for t=50, top right t=55, bottom left t=60 and bottom right t=65. All values are normalised to non-dimensional units.

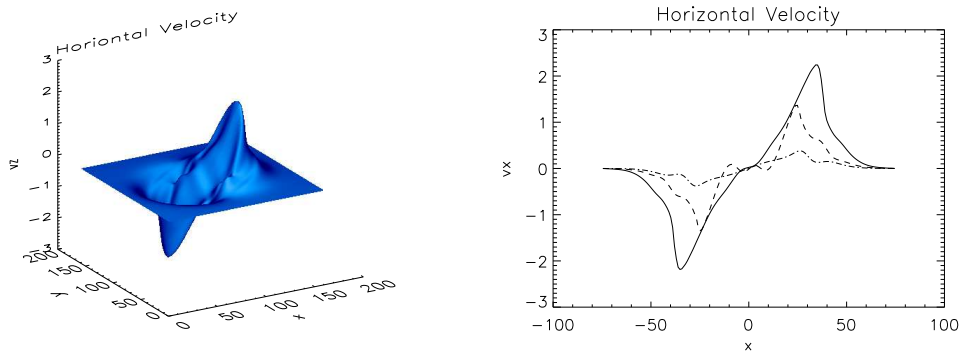

Figure 7.6: Horizontal velocity along the tube axis. The left panel shows a surface plot of v_x in the x,y plane at the height of the tube axis at t=55. The right panel shows a plot of v_x along the tube axis (y=0) at three different times. Dot-dashed line is for t=45, dashed line is for t=50, solid line is for t=55.

The previous chapter showed how the ion-neutral collisions are sufficient enough that the dissipation of cross-field currents forces the emerging magnetic field to be force-free. It also increased the rate of emergence of flux. In 3D, motions along the tube axis are now allowed, and this may cause a faster emergence because material is allowed to flow down the tube axis and thus increase buoyancy in the centre of the tube. This may cause the effect of ion-neutral collisions to be less important. If magnetic field moves faster through the partially ionised region, dissipation may be less important relative to advection (this corresponds to a higher R_m).

Figure 7.7 shows the development of the Cowling resistivity during the simulation. As time goes by more magnetic field rises from the photosphere due to the magnetic buoyancy instability and the value of η_c increases.

The Cowling resistivity reaches a maximum of about $3 \times 10^4 \Omega m$ which is larger than in the 2D case. A typical timescale for diffusion is approximately 2.5 s, which is less than the 2D case. However, as mentioned emergence in 3D is faster, and estimates of typical timescales for the transit of magnetic fields across the partially ionised region of the atmosphere are about 200 s. This gives an estimate of the Reynolds number similar to the 2D case. Even though the emergence is faster in 3D the relative importance of ion-neutral collisions appears to be the same as in 2D.

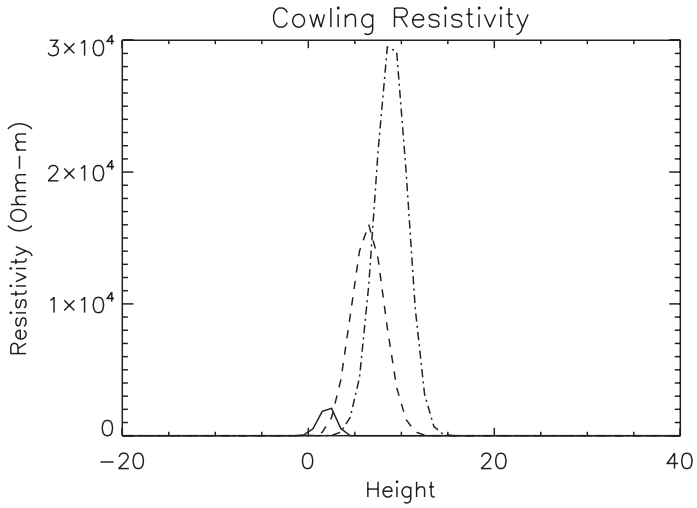

Figure 7.7: The Cowling resistivity in Ωm as a function of height in the centre of the horizontal domain. The solid line is for t=45, the dashed line is for t=48 and the dash-dotted line is for t=53. The height is given in dimensionless units.

This large increase in the Cowling resistivity means the magnetic field that passes through this region will be strongly affected by ion-neutral collisions. The evolution of the field will be diffusively dominated and the amount of flux emerging into the corona will increase. This can be seen in figure 7.8, which shows the total unsigned vertical flux

$$\Phi = \int_{xy} |B_z| dx dy \tag{7.11}$$

at different heights in the simulation. The partially ionised model has more flux emerging at coronal heights than the fully ionised model.

As in the 2D case, the region of large η_c in the partially ionised model means that the dissipation of currents is anisotropic, with only perpendicular currents being dissipated. If the emergence of magnetic field is slow enough then the dissipation of cross-field currents is enough that the only current to emerge with the magnetic field will be force-free. The total amount of field-aligned and cross-field current emerging

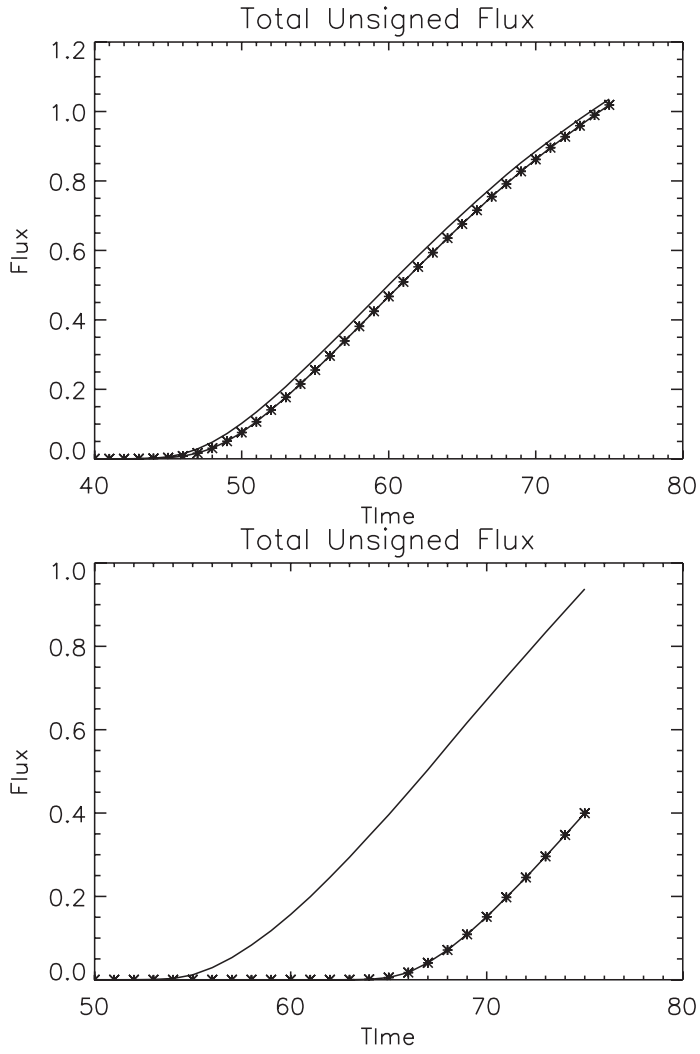

Figure 7.8: Total unsigned vertical flux (in dimensionless units) as a function of time at two different heights. The upper panel is for $z = 10$ and the lower panel is for z= 30. Solid lines are for PIP and asterisks are for FIP.

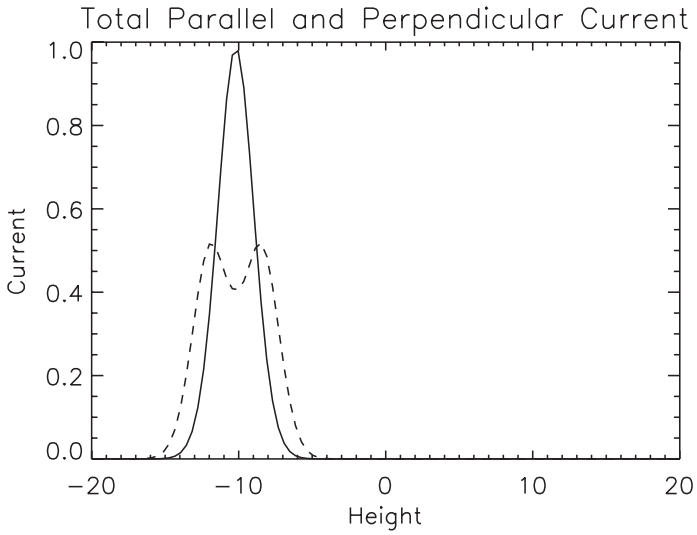

Figure 7.9: The total parallel (solid line) and total perpendicular currents at t=0 as a function of height.

with the field can be measured by the integrals

$$J_{\parallel}(z) = \int_{x,y} |j_{\parallel}(x,y,z)| dxdy \tag{7.12}$$

$$J_{\perp}(z) = \int_{x,y} |j_{\perp}(x,y,z)| dxdy. \tag{7.13}$$

The integrals are performed numerically over the horizontal domain. Figure 7.9 shows these integrals for the initial magnetic field profile at t=0. This calculation can be performed again at the end of the simulation. The total amount of perpendicular and parallel current that has emerged in the fully ionised case and the partially ionised case are shown in figure 7.10.

As can be seen, in the fully ionised case equivalent amounts of perpendicular and parallel current have emerged. However, in the partially ionised case, there is hardly any perpendicular current at coronal heights even though there is significant amounts of parallel current.

Again, as in the 2D case, parallel current is allowed to emerge in both simulations. However perpendicular current emerges only in the fully ionised model, whereas in the partially ionised model, perpendicular current is destroyed at heights of about z=15. In

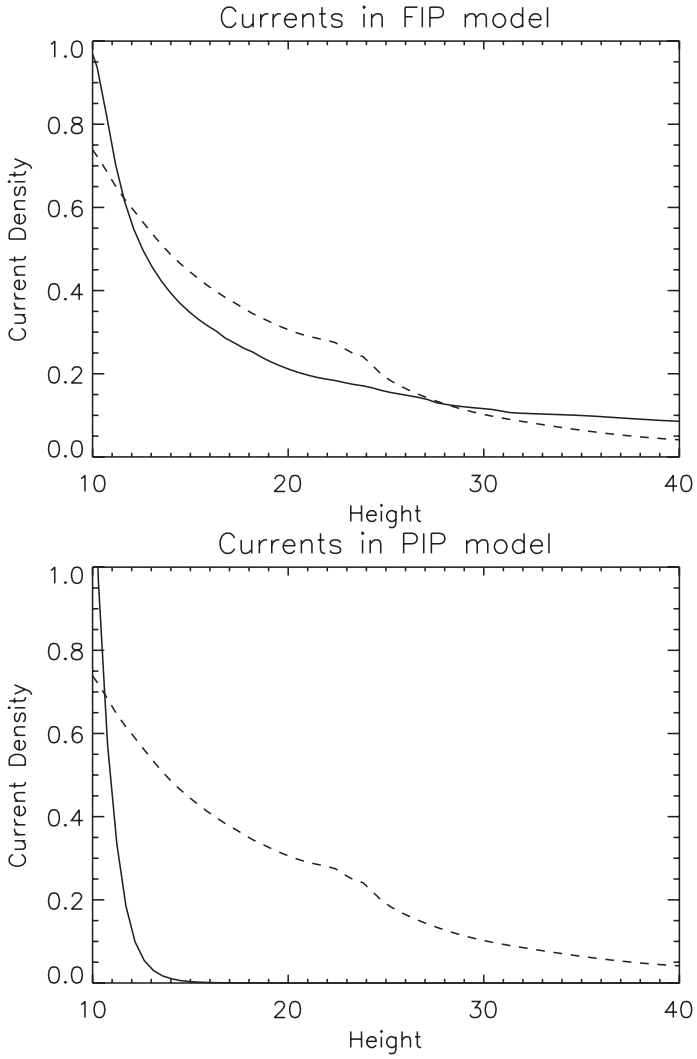

Figure 7.10: The two components of current as functions of height for the fully ionised model (top panel) and partially ionised model (bottom panel). Solid lines are total perpendicular current and dashed lines are total parallel current.

the partially ionised case, the magnetic field that has emerged has become force-free as the only currents to emerge with the field are aligned with the field, and therefore $\mathbf{j} \wedge \mathbf{B} = 0$.

7.5 Conclusions

3D simulations of the emergence of magnetic field from the convection zone into the corona have been performed. The evolution of the tube in the convection zone and lower atmosphere was similar to that in previous work (Fan, 2001; Archontis et al., 2004) with the magnetic buoyancy instability providing the mechanism for emergence into the atmosphere. The development of velocity shear provided further emergence by allowing plasma to drain down the tube axis and increase buoyancy, as in Manchester (2001) and Manchester et al. (2004).

As in chapter 6, the effect of the presence of neutrals on the emergence of magnetic flux was investigated by comparing two models. The first was the fully ionised plasma (FIP) model, as used by previous simulations, and the second was the partially ionised plasma (PIP) model, which included the effect of neutrals.

The results that were shown in chapter 6 also held in the 3D case. The presence of a region of large η_c lead to the magnetic field that emerged into the corona being much more diffuse. In addition the amount of flux reaching coronal levels was increased in the PIP model, as the evolution of the magnetic field was dominated by dissipation not advection, which was the case in the FIP model. Furthermore, the large anisotropy in dissipation in currents, caused by a large value of η_c, meant that perpendicular currents were preferentially dissipated. This anisotropic dissipation meant that only field aligned currents emerged with the field, and so the field became force-free.

Estimates at the height at which field becomes force-free were $y = 15$, which were lower than the values obtained in the 2D simulations. (Georgoulis and LaBonte, 2004) and (Metcalf et al., 1995) estimated that magnetic field becomes force-free about 400-1000 km (3-6 in dimensionless units) above the photosphere, based on extrapolations of vector magnetograms. The difference in observed values and ones from these

simulations may be due to the fact that observations were based on current active regions rather than newly forming ones, and as such the magnetic field will be in a less energetic state and more likely to be force-free at lower heights than in these simulations.

The results in this chapter support the notion that the presence of neutrals in the partially ionised atmosphere of the Sun has a strong effect on the emergence of magnetic fields. In particular the rate of emergence and the formation of force-free coronal field due to ion-neutral collisions.

Chapter 8

Conclusions and Future Work

8.1 Thesis Summary

The work in this thesis lead to the development of numerical techniques to simulate partially ionised plasmas in the fluid approximation. Using the multi-fluid equations for each species of a partially ionised plasma, single fluid equations were derived for a general Hydrogen plasma of arbitrary ionisation, along with a generalised Ohm's law. These governing equations were then recast for the partially ionised plasma of the Sun's atmosphere, and estimates of transport parameters were made. A Lagrangian Remap MHD code was then adapted to simulate the evolution of a partially ionised plasma.

The code was applied to the simulation of the propagation of Alfvén waves in the solar atmosphere in chapter 5. The efficiency of ion-neutral collisions in damping upwardly propagating Alfvén waves was investigated. Results from 1D simulations were in agreement with theoretical estimates based on linear damping, with ion-neutral collisions, being the most efficient damping mechanism, attenuating waves of frequencies greater than 0.1 Hz. Filter functions were derived for the efficiency of damping. These results were in broad agreement with previous work performed in the WKB approximation, and showed that the damping is heavily dependent on the local magnetic field strength. The simulations showed that Alfvén waves which are generated at the surface with frequencies greater than 0.5 Hz will be completely damped by ion-neutral collisions. One consequence is that any waves with frequencies greater than this detected in the

upper solar atmosphere cannot have originated at the surface.

Chapter 6 showed simulations and results from 2D simulations of the emergence of magnetic field from the convection zone of the Sun into the corona. One particular question regarding flux emergence is how magnetic field emerges through the convectively stable atmosphere, where buoyancy no longer operates. The magnetic buoyancy instability was shown to be a possible mechanism for emergence, caused by the development of a magnetic layer when a flux tube reaches the stable photosphere. Additional heating and cooling mechanisms, present in the lower atmosphere, where shown to affect the onset of this instability, and increased the growth of the instability which forces magnetic field into the corona. Further simulations investigated the effect of neutrals present in the partially ionised regions. Two important results came out of these simulations. The first was that the presence of neutrals introduced an additional dissipation term, and this term was significant enough that the evolution of the magnetic field in the partially ionised atmosphere was dominated by dissipation rather than advection. Magnetic field emerging into the corona was therefore more diffuse, and greater amounts of flux appeared at coronal levels. The second result, and arguably the more important, was that the ion-neutral collisions caused anisotropic dissipation of currents as magnetic field traversed the partially ionised region. This lead to the destruction of cross-field currents of the resultant coronal field. The presence of neutrals were shown to provide a mechanism for the formation of force-free coronal field from sub-surface field. This gives an answer to the question of how non-force-free field in the convection zone can become force-free in the corona.

Chapter 7 contains the details of 3D simulations, analogous to the 2D ones. In 3D, the mechanism for emergence was shown to be the same, but the presence of shear flows allows the magnetic field to emerge faster. The results of chapter 6 were verified in 3D, it is important to stress that the effectiveness of ion-neutral collisions depends on the speed of the emergence, and these simulations are for the emergence of magnetic flux due to the magnetic buoyancy instability. Flux tubes with greater amounts of twist may be less affected if the emergence mechanism is something other than the magnetic buoyancy instability.

The combined results in this thesis show that the solar atmosphere cannot be assumed to be fully ionised, as has been done in many simulations to date, and that the presence of neutrals has an important effect on the evolution of magnetic fields and therefore on the evolution of plasma in the solar atmosphere. The additional dissipation mechanism, provided by ion-neutral collisions, gives a mechanism for the conversion of sub-surface magnetic field in the convection zone into force-free coronal field. It has always been known that this change occurs, as the corona is a $\beta << 1$ plasma, while the convection zone is $\beta >> 1$. The work presented here shows a mechanism for this to occur, simply by treating the solar atmosphere as partially ionised.

8.2 Suggestions for Future Work

Having now developed a numerical code to simulate partially ionised plasma in the large length scale regime of the solar atmosphere, here are a few applications, based on simulations of magnetic fields in the solar atmosphere. However, it is important to note that any simulations which couple the surface magnetic field and the coronal fields should include partial ionisation, as it has been shown that if the evolution of the field is slow enough then all currents perpendicular to the field can be destroyed by ion-neutral collisions.

The increased dissipation due to ion-neutral collisions has applications in other studies of the solar atmosphere. In particular the coronal heating problem. It has been shown previously that the braiding of magnetic field by footpoint motions causes deposition of energy into the corona. Previous studies have investigated the dissipation of current sheets formed by considering random footpoint motions on initially homogeneous magnetic field. The subsequent, predominantly Joule dissipation leads to heating which is dependent on the footpoint motions, as well as the strength of the magnetic field. The additional Joule heating cause by partial ionisation will have an important effect on the Poynting flux provided to the corona.

This approach can be coupled to studies of magneto-convection at the surface. Rather than using random footpoint driving of initially homogeneous field, the driving

can be obtained from simulations of magneto-convection. Magnetic field can become twisted, stretched and concentrated by the convective motions of the plasma. Using the motions and magnetic fields as boundary conditions for simulations of flux braiding in the atmosphere, new heating rates can be calculated for the partially ionised regions above.

The work in this thesis has shown that the partially ionised regions of the solar atmosphere can transform emerging magnetic field into force-free field by the time it reaches the corona. However, it is still unclear as to the exact mechanism which forces magnetic field into the corona. In order to understand the subsequent coronal structures formed, detailed studies must be performed which model the emergence of magnetic field. Simulations must include the magneto-convection at and below the surface, as well as the effects of ionisation in the photosphere and chromosphere shown here, in order to realistically simulate the emergence of large scale fields.

By including magneto-convection in the models, and partial ionisation, the evolution through a more realistic atmosphere can be simulated. By varying the parameters of the magnetic field structure, different mechanisms can be simulated. For weakly twisted fields, the mechanism is a mixed mode of the magnetic buoyancy instability, for strong twist it is the kink instability. Using the models of magneto-convection coupled to the partial ionised regions, rates of emergence can be found and matched to observations.

In addition the thermal effects in the atmosphere must be investigated. Previous simulations of magnetic flux emergence have not been able to include energy transfer such as thermal conduction and radiative transfer. These must be included if the thermodynamic response to flux emergence in the solar atmosphere is to be accurately simulated. This is important in the partially ionised regions where ion-neutral collisions lead to an increased amount of Joule heating.

Appendix A

Numerical Integration of the Hydrostatic Equation

This appendix briefly describes the numerical scheme used for the numerical integration of the hydrostatic equation.

$$\frac{d}{dy}\left(\frac{\rho k_B T}{\mu_m}\right) = -\rho g \tag{A.1}$$

Density (ρ), temperature (T) and mean mass (μ_m) are defined at the cell centres (yc), while gravity g is defined at the vertexes (yb), as shown in figure A.1.

The partial derivative on left hand side of equation (A.1) is estimated by the first order difference

$$\frac{\frac{\rho_i k_B T_i}{\mu_{m\,i}} - \frac{\rho_{i-1} k_B T_{i-1}}{\mu_{m\,i-1}}}{dyc_{iy}} \tag{A.2}$$

while the right hand side can be averaged at the cell vertex $y_b(i-1)$. If the grid is stretched so that $dy_b(i-1) \neq dy_b(i)$ this averaging may be inaccurate so the average must be weighted by the size of the two contributing adjacent cells. Defining the average at the cell centre $y_b(i-1)$ as

$$\rho_{av} = \rho_{i-1}\frac{dyb_{i-1}}{dyb_{i-1} + dyb_i} + \rho_i \frac{dyb_i}{dyb_{i-1} + dyb_i} \tag{A.3}$$

gives a more accurate average. Defining

$$dg = \frac{1}{dyb_{i-1} + dyb_i} \tag{A.4}$$

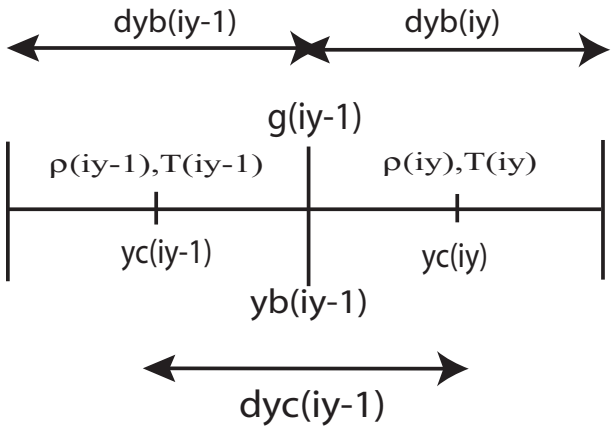

Figure A.1: Numerical grid showing the positions of the variables needed to solve the HS equation

then the numerical solution of (A.1) is then

$$\frac{\frac{\rho_i k_B T_i}{\mu_{m\,i}} - \frac{\rho_{i-1} k_B T_{i-1}}{\mu_{m\,i-1}}}{dyc_i} = -\rho_{i-1} g_{i-1} \frac{dyb_{i-1}}{dg} - \rho_i g_{i-1} \frac{dyb_i}{dg} \tag{A.5}$$

or

$$\rho_i = \rho_{i-1} \frac{\left[\frac{k_B T_{i-1}}{\mu_{m\,i-1} dyc_{i-1}} - \frac{g(i-1) dyb_{i-1}}{dg}\right]}{\left[\frac{k_B T_{i-1}}{\mu_{m\,i-1} dyc_{i-1}} + \frac{g(i-1) dyb_i}{dg}\right]}. \tag{A.6}$$

This gives a method to integrate the density in the vertical direction and only requires the value of the density at the base of the numerical domain. This can be found by using the VALC model to give the density at the height that the base of the domain represents (e.g. y=0 at the surface).

Although the Lagrangian remap code used in these simulations is second order in space, this first order method gives an equilibrium that is numerically stable, with typical velocities generated being at machine precision round-off.

Bibliography

W.P. Abbet and G.H. Fisher. A Coupled Model for the Emergence of Active Region Magnetic Flux into the Solar Atmosphere. *Astrophysical Journal*, 582:475–485, 2003.

D.J. Acheson. Instability by Magnetic Buoyancy. *Solar Physics*, 62:23–50, 1979.

V.A. Ambartsumyan. *Theoretical Astrophysics*. Pergamon Press, 1958.

H.M. Antia. *Lectures on Solar Physics*, page 80. Springer-Verlag Berlin, Berlin, 2003.

T.D. Arber, A.W. Longbottom, C.L Gerrard, and A.M. Milne. A Staggered Grid, Lagrangian-Eulerian Remap Code for 3-D MHD Simulations. *Journal of Computational Physics*, 171:151–181, 2001.

V. Archontis, F. Moreno-Insertis, K. Galsgaard, A. Hood, and E. O'Shea. Emergence of Magnetic Flux from the Convection Zone to the Corona. *Astronomy and Astrophysics*, 426:1047–1063, 2004.

V. Archontis, F. Moreno-Insertis, K. Galsgaard, and A. Hood. The Three-Dimensional Interaction Between Emerging Magnetic Flux and a Large-Scale Coronal Field: Reconnection, Current Sheets, and Jets. *Astrophysical Journal*, 635:1299–1318, 2005.

M.J. Aschwanden. Review of Coronal Oscillations - An Observers View. In *Turbulence, Waves and Instabilities in the Solar Plasma*, NATO Science Series II, 2003.

M.J. Aschwanden. *Physics of the Solar Corona*. Springer, Berlin, Germany and New York, U.S.A, 2004.

M.J. Aschwanden, L. Fletcher, C.J Schrijver, and D. Alexander. Coronal Loop Oscillations Observed with the Transition Region and Coronal Explorer. *Astrophysical Journal*, 520:880–894, 1999.

M.J. Aschwanden, C.J. Schrijver, B. De Pontieu, and A.M. Title. Transverse Oscillations in Coronal Loops Observed with TRACE - II. Measurents of Geometric and Physical Parameters. *Solar Physics*, 206:99–+, 2002.

H.W. Babcock. The Solar Magnetograph. *Astrophysical Journal*, 118:387–+, 1953.

H.W. Babcock. The Topology of the Sun's Magnetic Field and the 22-YEAR Cycle. *Astrophysical Journal*, 133:572–+, 1961.

J. N. Bahcall, M. H. Pinsonneault, and S. Basu. Solar Models: Current Epoch and Time Dependences, Neutrinos, and Helioseismological Properties. *Astrophysical Journal*, 555:990–1012, 2001.

J. W. Belcher. Alfvénic Wave Pressures and the Solar Wind. *Astrophysical Journal*, 168:509–+, 1971.

D. Berghmans and F. Clette. Active Region EUV Transient Brightenings - First Results by EIT of SOHO JOP80. *Solar Physics*, 186:207–229, 1999.

S.I. Braginskii. Transport processes in a plasma. In *Reviews of Plasma Physics*, volume 1. New York: Consultants Bureau, 1965.

J.C. Brown. On the Ionisation of Hydrogen in Optical Flares. *Solar Physics*, 29:421–427, 1979.

P. Bushby and J. Mason. Solar Dynamo: Understanding the Solar Dynamo. *Astronomy and Geophysics*, 45:7–13, 2004.

P. Caligari, F. Moreno-Insertis, and M. SChüssler. Emerging Flux Tubes in the Solar Convection Zone. I. Asymmetry, Tilt, and Emergence Latitude. *Astrophysical Journal*, 441:886–902, 1995.

P. Caligari, M. Schussler, and F. Moreno-Insertis. Emerging Flux Tubes in the Solar Convection Zone. II. The Influence of Initial Conditions. *Astrophyical Journal*, 502: 481–492, 1998.

F. Cattaneo and D. W. Hughes. Nonlinear Saturation of the Turbulent α Effect. *Physical Review E*, 54:4532–+, November 1996.

P. Charbonneau and K. B. MacGregor. On the Generation of Equipartition-Strength Magnetic Fields by Turbulent Hydromagnetic Dynamos. *Astrophysical Journal*, 473: L59–L62, 1996.

A. R. Choudhuri. The Evolution of Loop Structures in Flux Rings Within the Solar Convection Zone. *Solar Physics*, 123:217–239, 1989.

J. Christensen-Dalsgaard, W. Dappen, S. V. Ajukov, E. R. Anderson, H. M. Antia, S. Basu, V. A. Baturin, G. Berthomieu, B. Chaboyer, S. M. Chitre, A. N. Cox, P. Demarque, J. Donatowicz, W. A. Dziembowski, M. Gabriel, D. O. Gough, D. B. Guenther, J. A. Guzik, J. W. Harvey, F. Hill, G. Houdek, C. A. Iglesias, A. G. Kosovichev, J. W. Leibacher, P. Morel, C. R. Proffitt, J. Provost, J. Reiter, E. J. Rhodes, Jr., F. J. Rogers, I. W. Roxburgh, M. J. Thompson, and R. K. Ulrich. The Current State of Solar Modeling. *Science*, 272:1286–+, 1996.

Cowling. *MagnetoHydrodynamics, Monographs on Astronomical Subjects*. Adam Hilger, 1957.

S.R. Cranmer and A.A. Van Ballegooijen. On the Generation, Propagation, and Reflection of Alfvén Waves from the Solar Atmosphere to the Distant Heliosphere. *Astrophysical Journal*, 156:265–293, 2005.

I. De Moortel. Observation of Oscillations in Coronal Loops. *Astronomy and Astrophysics*, 355:L23–L26, 2000.

I. De Moortel and A.W. Hood. The Damping of Slow MHD Waves in Solar Coronal Magnetic Fields. II. The Effect of Gravitational Stratification and Field Line Divergence. *Astronomy and Astrophysics*, 415:705–715, 2004.

B. De Pontieu. Numerical Simulations of Spicules Driven by Weakly Damped Alfvén Waves. *Astronomy and Astrophysics*, 347:696–710, 1999.

B. De Pontieu and G. Haerendel. Weakly Damped Alfvén Waves as Drivers for Spicules. *Astronomy and Astrophysics*, 338:729–736, 1998.

B. De Pontieu, P.C.H Martens, and H.S Hudson. Chromospheric Damping of Alfvén Waves. *Astrophysical Journal*, 558:859–871, 2001.

C. E. DeForest. High-Frequency Waves Detected in the Solar Atmosphere. *Astrophysical Journal*, 617:L89–L92, 2004.

C. E. Deforest and J. B. Gurman. Observation of Quasi-periodic Compressive Waves in Solar Polar Plumes. *Astrophysical Journal*, 501:L217–L220, 1998.

S. D'Silva and A. R. Choudhuri. A Theoretical Model For Tilts of Bipolar Magnetic Regions. *Astronomy and Astrophysics*, 272:621–633, 1993.

Y. Elsworth, R. Howe, G. R. Isaak, C. P. McLeod, and R. New. Evidence from Solar Seismology Against Non-Standard Solar-Core Models. *Nature*, 347:536–539, 1990.

T. Emonet and F. Moreno-Insertis. The Physics of Twisted Magnetic Flux Tubes Rising in a Stratified Medium: Two-Dimensional Results. *Astrophysical Journal*, 492:804–821, 1998.

R. Erdélyi. Heating of the Solar Corona: Review. *Publications of the Astronomy Deparment of the Eotvos Lorand University*, 15:7–+, 2005.

C.R. Evans and J.F. Hawley. Simulation of Magnetohydrodynamic Flows - A Constrained Transport Method. *Astrophysical Journal*, 332:659–677, 1988.

Y. Fan. The Emergence of a Twisted Ω-Tube into the Solar Atmosphere. *Astrophysical Journal*, 554:L111–L114, 2001.

Y. Fan, G. H. Fisher, and E. E. Deluca. The Origin of Morphological Asymmetries in Bipolar Active Regions. *Astrophysical Journal*, 405:390–401, 1993.

Y. Fan, G. H. Fisher, and A. N. McClymont. Dynamics of Emerging Active region Flux Loops. *Astrophysical Journal*, 436:907–928, 1994.

Y. Fan, E.G. Zweibel, M.G. Linton, and G.H. Fisher. The Rise of Kink-Unstable Magnetic Flux Tubes and the Origin of δ-Configuration Sunspots. *Astrophysical Journal*, 460: 460–477, 1999.

J. Feynman and S. F. Martin. The Initiation of Coronal Mass Ejections by Newly Emerging Magnetic Flux. *Journal of GeoPhysical Research*, 100:3355–3367, 1995.

G. H. Fisher, Y. Fan, and R. F. Howard. Comparisons Between Theory and Observation of Active Region Tilts. *Astrophysical Journal*, 438:463–471, 1995.

A. Fossum and M. Carlsson. Response Functions of the Ultraviolet Filters of TRACE and the Detectability of High-Frequency Acoustic Waves. *Astrophysical Journal*, 625: 556–562, 2005.

D. J. Galloway and N. O. Weiss. Convection and Magnetic Fields in Stars. *Astrophysical Journal*, 243:945–953, 1981.

K. Galsgaard, F. Moreno-Insertis, V. Archontis, and A. Hood. A Three-Dimensional Study of Reconnection, Current Sheets and Jets Resulting from Magnetic Flux Emergence in the Sun. *Astrophysical Journal*, 618:L153–L156, 2005.

M.K. Georgoulis and B.J. LaBonte. Vertical Lorentz Force and Cross-Field Currents in the Photospheric Magnetic Fields of Solar Active Regions. *Astrophysical Journal*, 162:1029–1041, 2004.

S. E. Gibson and Y. Fan. The Partial Expulsion of a Magnetic Flux Rope. *Astrophysical Journal*, 637:L65–L68, 2006.

P.A. Gilman. Instability of MagnetoHydroStatic Stellar Interiors from Magnetic Buoyancy. I. *Astrophysical Journal*, 162:1019–1029, 1970.

M.L. Goldstein, D.A. Roberts, and W.H. Matthaeus. MagnetoHydrodynamic Turbulence in the Solar Wind. *Annual Review of Astronomy and Astrophysics*, 33:283–325, 1995.

M. Goossens, A. De Groof, and J. Andries. Waves and Oscillations in Magnetic Fields. In H. Sawaya-Lacoste, editor, *SOLMAG: Magnetic Coupling of the Solar Atmosphere*, volume SP-505 of *ESA Conference Proceedings*, page 137. ESA, 2002.

D. O. Gough, A. G. Kosovichev, J. Toomre, E. Anderson, H. M. Antia, S. Basu, B. Chaboyer, S. M. Chitre, J. Christensen-Dalsgaard, W. A. Dziembowski, A. Eff-Darwich, J. R. Elliott, P. M. Giles, P. R. Goode, J. A. Guzik, J. W. Harvey, F. Hill, J. W. Leibacher, M. J. P. F. G. Monteiro, O. Richard, T. Sekii, H. Shibahashi, M. Takata, M. J. Thompson, S. Vauclair, and S. V. Vorontsov. The Seismic Structure of the Sun. *Science*, 272:1296–1300, 1996.

G. E. Hale. On the Probable Existence of Magnetic Fields in Sun-Spots. *Astrophysical Journal*, 28:315–+, 1908.

J. V. Hollweg. Waves and Instabilities in the Solar Wind. *Reviews of Geophysics and Space Physics*, 13:263–289, 1975.

A.W. Hood. *Plasma Physics: An Introductory Course*, pages 267–290. Cambridge University Press, 1996.

S.P. James, R. Erdélyi, and B. De Pontieu. Can Ion-Neutral Damping Help to Form Spicules? *Astronomy and Astrophysics*, 406:715–724, 2003.

M. L. Khodachenko, H. O. Rucker, R. Oliver, T. D. Arber, and A. Hanslmeier. On the Mechanisms of MHD Wave Damping in the Partially Ionized Solar Plasmas. *Advances in Space Research*, 37:447–455, 2006.

M.L Khodachenko, T.D Arber, H.O Rucker, and A. Hanslmeier. Collisional and Viscous Damping of MHD Waves in Partially Ionized Plasmas of the Solar Atmosphere. *Astronomy and Astrophysics*, 422:1073–1084, 2004.

B. Kliem, I.E. Dammasch, W. Curdt, and K. Wilhelm. Correlated Dynamics of Hot and Cool Plasmas in the Main Phase of a Solar Flare. *Astrophysical Journal Letters*, 508: L61–L65, 2002.

J. A. Klimchuk. On Solving the Coronal Heating Problem. *Solar Physics*, 234:41–77, 2006.

A. G. Kosovichev, J. Schou, P. H. Scherrer, R. S. Bogart, R. I. Bush, J. T. Hoeksema, J. Aloise, L. Bacon, A. Burnette, C. de Forest, P. M. Giles, K. Leibrand, R. Nigam, M. Rubin, K. Scott, S. D. Williams, Sarbani Basu, J. Christensen-Dalsgaard, W. Dappen, Jr. Rhodes, E. J., Jr. Duvall, T. L., R. Howe, M. J. Thompson, D. O. Gough, T. Sekii, J. Toomre, T. D. Tarbell, A. M. Title, D. Mathur, M. Morrison, J. L. R. Saba, C. J. Wolfson, I. Zayer, and P. N. Milford. Structure and Rotation of the Solar Interior: Initial Results from the MDI Medium-L Program. *Solar Physics*, 170:43–61, 1997.

J.E. Leake and T.D. Arber. The Emergence of Magnetic Flux Through a Partially Ionised Solar Atmosphere. *Astronomy and Astrophysics*, 450:805–818, 2006.

J.E. Leake, T.D. Arber, and M.L. Khodachenko. Collisional Dissipation of Alfvén Waves in a Partially Ionised Solar Atmosphere. *Astronomy and Astrophysics*, 442:1091–1098, 2005.

J. W. Leibacher and R. F. Stein. A New Description of the Solar Five-Minute Oscillation. *Astrophysical Letters*, 7:L191–L192, 1971.

R. B. Leighton. A Magneto-Kinematic Model of the Solar Cycle. *Astrophysical Journal*, 156:1–26, 1969.

R.B. Leighton, R.W. Noyes, and G.W. Simon. Velocity Fields in the Solar Atmosphere. I. Preliminary Report. *Astrophysical Journal*, 135:474–499, 1962.

M.G. Linton, D. W. Longcope, and G.H. Fisher. The Helical Kink Instability of Isolated, Twisted Magnetic Flux Tubes. *Astrophysical Journal*, 469:954–963, 1996.

M.G. Linton, G.H. Fisher, R.B. Dahlburg, and Y. Fan. Nonlinear Evolution of Kink-Unstable Magnetic Flux Tubes and solar δ-Spot Active Regions. *Astrophysical Journal*, 507:404–416, 1998.

M.G. Linton, R.B. Fisher, G.H.a dn Dahlburg, and Y. Fan. Relationship of the Multimode Kink Instability to δ-Spot Formation. *Astrophysical Journal*, 522:1190–1205, 1999.

D. W. Longcope and G. H. Fisher. The Effects of Convection Zone Turbulence on the Tilt Angles of Magnetic Bipoles. *Astrophysical Journal*, 458:380–+, 1996.

T. Magara. Dynamics of Emerging Flux Tubes in the Sun. *Astrophysical Journal*, 549: 608–628, 2001.

T. Magara. A Model for Dynamic Evolution of Emerging Magnetic Fields in the Sun. *Astrophysical Journal*, 605, 2004.

T. Magara and D. W. Longcope. Injection of Magnetic Energy and Magnetic Helicity into the Solar Atmosphere by an Emerging Magnetic Flux Tube. *Astrophysical Journal*, 586:630–649, 2003.

T. Magara and D.W. Longcope. Sigmoid Structure of an Emerging Flux Tube. *Astrophysical Journal*, 559:L55–L59, 2001.

W. I. Manchester. The Role of Nonlinear Alfvén Waves in Shear Formation during Solar Magnetic Flux Emergence. *Astrophysical Journal*, 547:503–519, 2001.

W. IV. Manchester, T. Gambosi, D. Dezeeuw, and Y. Fan. Eruption of a Buoyantly Emerging Magnetic Flux Rope. *Astrophysical Journal*, 610:588–596, 2004.

P. K. Manoharan, S. Ananthakrishnan, M. Dryer, T. R. Detman, H. Leinbach, M. Kojima, T. Watanabe, and J. Kahn. Solar Wind Velocity and Normalized Scintillation Index from Single-Station IPS Observations. *Solar Physics*, 156:377, 1995.

E. Marsch and C.-Y. Tu. The Effects of High-Frequency Alfven Waves on Coronal Heating and Solar Wind Acceleration. *Astronomy and Astrophysics*, 319:L17–L20, 1997.

V. Martinez-Pillet, B.W Lites, and A. Skumanich. Active Region Magnetic Fields I. Plage Fields. *Astrophysical Journal*, 474:810–842, 1997.

R. Matsumoto and K. Shibata. Three-Dimensional MHD Simulation of the Parker Instability in Galactic Gas Disks and the Solar Atmosphere. *Astronomical Society of Japan, Publications*, 44:167–175, 1992.

R. Matsumoto, T. Tajima, K. Shibata, and M. Kaisig. Three-Dimensional Magnetohydrodynamics of the Emerging Magnetic Flux in the Solar Atmosphere. *Astrophysical Journal*, 414:357–371, 1993.

R. Matsumoto, T. Tajima, W. Chou, A. Okubo, and K. Shibata. Formation of a Kinked Alignment of Solar Active Regions. *Astrophysical Journal*, 493:L43–L46, 1998.

P.C. Matthews, D.W. Hughes, and M.R.E. Proctor. Magnetic Buoyancy, Vorticity, and Three-Dimensional Flux-Tube Formation. *Astrophysical Journal*, 448:938–941, 1995.

T.R. Metcalf, A. Jiao, A.N. McClymont, R.C. Canfield, and H. Uitenbroek. Is the Solar Chromospheric Magnetic Field Force-Free? *Astrophysical Journal*, 439:474–481, 1995.

F. Moreno-Insertis. Nonlinear Time-Evolution of Kink-Unstable Magnetic Flux Tubes in the Convective Zone of the Sun. *Astronomy and Astrophysics*, 166:291–305, 1986.

F. Moreno-Insertis. *Sunpots, Theory and Observations*, page 385. Kluwer Academic Publ., 1992.

F. Moreno-Insertis. Multidimensional Simulations of the Rise of Magnetic Flux Tubes. In *Advances in the Physics of Sunspots*, volume 118, pages 45–65, 1997.

F. Moreno-Insertis and T. Emonet. The Rise of Twisted Flux Tubes in a Stratified Medium. *Astrophysical Journal*, 472:L53–L56, 1996.

V.M Nakariakov, L. Ofman, E.E. DeLuca, B. Roberts, and J.M. Davila. TRACE Observations of Damped Coronal Loop Oscillations: Implications for Coronal Heating. *Science*, 285:862–+, 1999.

V.M. Nakariakov, V.F. Melnikov, and V.E. Reznikova. Global Sausage Modes of Coronal Loops. *Astronomy and Astrophysics*, 412:L7–L10, 2003.

U. Narain and P. Ulmscneider. Chromospheric and Coronal Heating Mechanisms. *Space Science Reviews*, 54:377–445, 1990.

W.A. Newcomb. Convective Instability Induced by Gravity in a Plasma with a Frozen-In Magnetic Field. *Physics of Fluids*, 4:391–+, 1961.

S. Nozawa, K. Shibata, and R. Matsumoto. Emergence of Magnetic Flux from the Convection Zone into the Solar Atmosphere. I - Linear and Nonlinear Adiabatic Evolution of the Convective-Parker Instability. *Astrophysical Journal Supplement*, 78:267–282, 1992.

L. Ofman, M. Romoli, G. Poletto, G. Noci, and J.L. Kohl. UltraViolet Coronagraoh Spectrometer Observtaions of Density Fluctuations in the Solar Wind. *Astrophysical Journal*, 491:L111–L114, 1997.

L. Ofman, V.M. Nakariakov, and C.E. Deforest. Slow magnetoacoustic waves in coronal plumes. *Astrophysical Journal*, 514:441–447, 1999.

R. Oliver and J. L. Ballester. Oscillations in Quiescent Solar Prominences Observations and Theory (Invited Review). *Solar Physics*, 206:45–67, 2002.

M. Ossendrijver. The Solar Dynamo. *Astronomy and Astrophysics Review*, 11:287–367, 2003.

E. N. Parker. Instability of Thermal Fields. *Astrophysical Journal*, 117:431–436, 1953.

E. N. Parker. A Solar Dynamo Surface Wave at the Interface Between Convection and Nonuniform Rotation. *Astrophysical Journal*, 408:707–719, 1993.

E.N. Parker. The Formation of Sunspots from the Solar Toroidal Field. *Astrophysical Journal*, 121:491–507, 1955.

E.N. Parker. The Instability of a Horizontal Magnetic Field in an Atmosphere Stable Against Convection. *Astrophysics and Space Science*, 62:135–142, 1979.

S.R. Pottasch and R.N. Thomas. Departures From the Saha Equation Under Varying Conditions of Lyman Continuous Opacity. *Astrophysical Journal*, 130:941–953, 1959.

M.R.E. Proctor. Magnetoconvection: Solar Convection and Magnetic Fields. *Astronomy and Geophysics*, 45, 2004.

J.J. Quirk. *Int. J. Numeric. Meth. Fluids*, 18:555, 1994.

E. Robbrecht, E. Verwichte, D. Berghmans, J.F. Hochedez, S. Poedts, and V.M Nakariakov. Slow MagnetoAcoustic Waves in Coronal Loops: EIT and TRACE. *Astronomy and Astrophysics*, 370:591–601, 2001.

B. Roberts. Waves and Oscillations in the Corona: Theory - (Invited Review). *Solar Physics*, 193:139, 2000.

B. Roberts. Waves and Oscillations in the Corona: Theory. In A. Wilson, editor, *Solar Variability: From Core to Outer Frontiers*, volume SP-506 of *ESA Conference Proceedings*, page 481. ESA, 2002.

B. Roberts. MHD Waves in the Solar Atmosphere. In H. Lacoste, editor, *Waves, Oscillations and Small-Scale Transient Events in the Solar Atmosphere*, volume SP-547 of *ESA Conference Proceedings*, page 1. ESA, 2004.

B. Roberts and V.M Nakaraiakov. Theory of MHD Waves in the Solar Corona. In R. Erdélyi, K. Petrovay, B. Roberts, and M. Ashwanden, editors, *Turbulence, Waves and Instabilities in the Solar Plasma*, volume 124 of *NATO Science Series II*, page 167, 2003.

J. Schou, H. M. Antia, S. Basu, R. S. Bogart, R. I. Bush, S. M. Chitre, J. Christensen-Dalsgaard, M. P. di Mauro, W. A. Dziembowski, A. Eff-Darwich, D. O. Gough, D. A. Haber, J. T. Hoeksema, R. Howe, S. G. Korzennik, A. G. Kosovichev, R. M. Larsen, F. P. Pijpers, P. H. Scherrer, T. Sekii, T. D. Tarbell, A. M. Title, M. J. Thompson, and J. Toomre. Helioseismic Studies of Differential Rotation in the Solar Envelope by the Solar Oscillations Investigation Using the Michelson Doppler Imager. *Astrophysical Journal*, 505:390–417, 1998.

C.J. Schrijver, M.J. Aschwanden, and A.M. Title. Transverse Oscillations in Coronal

Loops observed with TRACE - I. An Overview of Events, Movies and a Discussion of Common Properties and Required Conditions. *Solar Physics*, 206:69–98, 2002.

M. Schüβler. Magnetic Buoyancy Revisited - Analytical and Numerical Results for Rising Flux Tubes. *Astronomy and Astrophysics*, 71:79–91, 1979.

A. Severny. Solar magnetic fields. *Space Science Reviews*, 3:451, 1964.

K. Shibata, T. Tajima, R. Matsumoto, T. Horiuchi, T. Hanawa, R. Rosner, and Y. Uchida. Nonlinear Parker Instability of Isolated Magnetic Flux in a Plasma. *Astrophysical Journal*, 338:471–492, 1989.

K. Shibata, T. Tajima, and R.S. Steinolfson. Two-Dimensional Magnetohydrodynamic Model of Emerging Magnetic Flux in the Solar Atmosphere. *Astrophysical Journal*, 345:584–596, 1989.

K. Shibata, S. Nozawa, R. Matsumoto, A. C. Sterling, and T. Tajima. Emergence of Solar Magnetic Flux from the Convection Zone into the photosphere and Chromosphere. *Astrophysical Journal*, 351:L25–L28, 1990.

G. W. Simon and R. B. Leighton. Velocity Fields in the Solar Atmosphere. III. Large-Scale Motions, the Chromospheric Network, and Magnetic Fields. *Astrophysical Journal*, 140:1120–+, 1964.

E.A. Spiegel and N.O. Weiss. Magnetic Activity and Variations in Solar Luminosity. *Nature*, 287:616, 1980.

L. Spitzer. *Physics of Fully Ionised Gases*. Number 3 in Interscience Tracts on Physics and Astronomy. John Wiley and Sons, 1962.

M. Stix. Differential Rotation and the Solar Dynamo. *Astronomy and Astrophysics*, 47: 243–254, 1976.

M. Stix. *The Sun: An Introduction*. Springer, 2002.

Thomas and Athay. *Physics of the Solar Chromosphere (3rd ed.)*. Oxford University Press, 1961.

J.H. Thomas and A.H. Nye. Convective Instability in the Presence of a Nonuniform Horizontal Magnetic Field. *Physics of Fluids*, 18:490–+, 1975.

B.J. Thompson, S.P. Plunkett, J.B. Gurman, O.C. Newmark, J.S.and St Cyr, and D.J. Michels. SOHO/EIT Observations of an Earth-directed Coronal Mass Ejection on May 12, 1997. *Geophysical Research Letters*, 25:2461–2464, 1998.

M. J. Thompson, J. Toomre, E. Anderson, H. M. Antia, G. Berthomieu, D. Burtonclay, S. M. Chitre, J. Christensen-Dalsgaard, T. Corbard, M. Derosa, C. R. Genovese, D. O. Gough, D. A. Haber, J. W. Harvey, F. Hill, R. Howe, S. G. Korzennik, A. G. Kosovichev, J. W. Leibacher, F. P. Pijpers, J. Provost, E. J. Rhodes, J. Schou, T. Sekii, P. B. Stark, and P. Wilson. Differential Rotation and Dynamics of the Solar Interior. *Science*, 272:1300–+, 1996.

S. M. Tobias, N. H. Brummell, T. L. Clune, and J. Toomre. Transport and Storage of Magnetic Field by Overshooting Turbulent Compressible Convection. *Astrophysical Journal*, 549:1183–1203, 2001.

E. Tu, C.-Y.and Marsch. MHD Structures, Waves and Turbulence in the Solar Wind: Observations and Theories. *Space Science Review*, 73:1–2, 1995.

P. Ulmschneider and Z. Musielak. Mechanisms of Chromospheric and Coronal Heating (Invited review). In A. A. Pevtsov and H. Uitenbroek, editors, *ASP Conf. Ser. 286: Current Theoretical Models and Future High Resolution Solar Observations: Preparing for ATST*, pages 363–+, 2003.

R. K. Ulrich. Observations of Magnetohydrodynamic Oscillations in the Solar Atmosphere with Properties of Alfven Waves. *Astrophysical Journal*, 465:436–+, 1996.

R.K. Ulrich. Observations of MHD Oscillations in the Solar Atmosphere with Properties of Alfvén Waves. *Astrophysical Journal*, 465:436–450, 1996.

A.A. van Ballegooijen. The Structure of the Solar Magnetic Field Below the Photosphere. I - Adiabatic Flux Tube Models. *Astronomy and Astrophysics*, 106:43–52, 1982.

B. van Leer. Towards the Ultimate Conservative Difference Scheme. V - A Second-Order Sequel to Godunov's Method. *Journal of Computational Physics*, 32:101–136, 1979.

J.E. Vernazza, E.H. Avrett, and R. Loeser. Structure of the Solar Chromosphere. III - Models of the EUV Brightness Components of the Quiet-Sun. *Astrophysical Journal Supplement*, 45:635–725, 1981.

A. Vögler, S. Shelyag, M. Schüssler, F. Cattaneo, T. Emonet, and T. Linde. Simulations of Magneto-convection in the Solar photosphere: Equations, methods, and results of the MURaM code. *Astronomy and Astrophysics*, 429:335–351, 2005.

T.J. Wang, S.K. Solanki, W. Curdt, D.E. Innes, and I.E. Dammasch. Doppler Shift Oscillations of Hot Solar Coronal Plasma Seen by SUMER: A Signature of Loop Oscillation? *Astrophysical Journal*, 574:L101–L104, 2002.

Y.-M. Wang and N. R. Sheeley, Jr. Filament Eruptions near Emerging Bipoles. *Astrophysical Journal*, 510:L157–L160, 1999.

M. L. Wilkins. Use of Artificial Viscosity in Multidimensional Fluid Dynamic Calculations. *Journal of Computational Physics*, 36:281–303, 1980.

J. G. Wissink, P. C. Matthews, D. W. Hughes, and M. R. E. Proctor. Numerical Simulations of Buoyant Magnetic Flux Tubes. *Astrophysical Journal*, 536:982–997, 2000.

S. T. Wu, W. P. Guo, S. P. Plunkett, B. Schmieder, and G. M. Simnett. Coronal Mass Ejections (CMEs) Initiation: Models and Observations. *Journal of Atmospheric and Terrestrial Physics*, 62:1489–1498, 2000.

C. Zwann. On the Appearance of Magnetic Flux in the Solar Photosphere. *Solar Physics*, 60:213–240, 1978.